Comput Mech (2007) 39: 153–190
DOI 10.1007/s00466-005-0016-7

ORIGINAL PAPER

D. Fressmann · P. Wriggers

Advection approaches for single- and multi-material arbitrary Lagrangian–Eulerian finite element procedures

Received: 20 July 2005 / Accepted: 14 October 2005 / Published online: 8 December 2005

Abstract The essential feature in arbitrary Lagrangian–Eulerian (ALE) based finite element approaches is the additional requirement to consider flow effects of the materials and the solution variables through the computational domain. These flow effects are commonly known as advective effects. The present paper examines different advection strategies for the application of the ALE finite element method in a finite deformation solid mechanics framework, where especially micromechanical problems are referred to. The global solution algorithm is based on the well-known fractional step method that provides an operator splitting approach for the solution of the coupled ALE equations. Distinguishing the so-called single-material and the multi-material ALE method, different advection schemes based on volume- and material-associated advection procedures are required. For the latter case, the material interfaces are not resolved explicitly by the finite element mesh. Instead a volume-of-fluid interface tracking approach in terms of the volume fractions of the different material phases is applied.

Keywords Arbitrary Lagrangian–Eulerian · Finite deformations · Finite elementmethod · Volume-of-fluid interface reconstruction · Advection schemes

1 Introduction

Conventional finite element procedures in a solid-mechanics framework are usually based on a purely Lagrangian view of the deformation, where the finite element mesh remains attached to the material points while the material deforms according to the governing equations. The advantages of this approach are obvious: material points are explicitly tracked during the proceeding deformation process, and the history of these points can be accessed directly. Thus the handling of history variables, necessary to describe e.g. inelastic effects, becomes straightforward. Furthermore, if a domain with multiple material properties is analyzed, material boundaries are resolved explicitly by the finite element edges and are thus considered very accurately in dependence of the local mesh size. However, a considerable drawback of these methods appears, if large material deformations have to be taken into account. Deforming elements lead to a deterioration of the solution and in the limit potentially to an inversion of single elements. As a consequence, the analysis terminates due to negative Jacobians and cannot be continued (cf. e.g. [8] and references therein).

In this case, a remeshing procedure becomes necessary, where in general a new mesh in the deformed configuration is generated and the current solution state is transferred to this new mesh using appropriate transfer procedures. An efficient and continuum-mechanical consistent formulation can be achieved by the arbitrary Lagrangian–Eulerian (ALE) method that introduces additional flux terms into the governing equations (see e.g. [22, 42] or [36]). Essential in this case is a constant mesh topology, where only the mesh nodes are relocated to obtain a homogeneous and undistorted mesh. The resulting partial differential equations represent a set of coupled equations for the material velocity and the relative velocity between the mesh and the material, which is also known as the convective velocity. If the material deformations and the convective velocity are discretized simultaneously using a conventional (Bubnov-) Galerkin-type approach, various problems concerning the stability and robustness of the finite element solution can occur. This requires the implementation of special upwinding procedures, like the streamline upwind Petrov-Galerkin (SUPG) or the Galerkin least squares method (see e.g. [8, 17, 37, 43] or [62] for a review of these methods). Another problem is the occurrence of the second spatial derivatives of the primary variable in the advection term. In case of linear ansatz spaces for the displacements and the velocities, these gradients cannot be computed properly

D. Fressmann (✉)
Department of Civil, Surveying and Environmental Engineering,
University of Newcastle, Newcastle NSW 2308, Australia
E-mail: dirk.fressmann@newcastle.edu.au

P.Wriggers
Institute for Mechanics and Computational Mechanics,
University of Hannover, Hannover Germany
E-mail: wriggers@ibnm.uni-hannover.de

on the element level and a least-squares extrapolation to the nodes, based on a C^0-continuous distribution of the primary variable or a mixed formulation becomes necessary. Note that these approaches can lead to a considerably more complex implementation of the global algorithm.

This motivates the use of a computational split, where the coupled set of equations is decomposed into a Lagrangian step and a transport or advection step. In the first step, all advective effects, i.e. flow effects, are neglected and the mesh deforms with the material, while the second step explicitly accounts for the relative motion of the finite element mesh with respect to the material. This computational split is usually referred to as *fractional-step* or *operator-split* approach and can be found in various publications in the ALE literature (see e.g. [9, 13, 20] or [56]). The constant mesh topology enables the determination of material fluxes and fluxes of the solution variables across the edges of adjacent elements, where the transport process can now be performed by solving the linear, homogeneous advection equation. Indeed, this is a common problem in the fluid dynamics community and special purpose algorithms can be applied for the solution of the transport problem, which will be the main topic of this paper.

A further point of discussion is the consideration of material boundaries in a domain with multiple material properties as it appears for instance in micromechanical observations of heterogeneous materials. In an ALE framework usually two different strategies are conceivable. Within a single-material ALE (SALE) approach, the material interfaces are accurately resolved by the element edges in a Lagrangian manner throughout the whole deformation process (see e.g. [9, 27] or [57]), whereas in a multi-material ALE (MMALE) approach, the different materials are allowed to "flow" freely through the computational domain without persistent connection to the finite element mesh ([10] or [49]). This implies that also the material interfaces are allowed to change their position relative to the elements and therefore so-called *mixed elements* with multiple material properties have to be taken into account. The tracking of the material deformations is performed by the volume-of-fluid method (VOF) ([32]), where different material occurrences are considered by their respective volume fractions on the element level. This requires the inclusion of special integration algorithms for the governing finite element equations. In this framework, a distinction between volume- and material-associated quantities has to be introduced and special advection procedures have to be incorporated for both kinds of variables. In particular, material-associated quantities require an advection process that is able to account for the distribution of the different material phases to consider the conservation properties of the solution variables with respect to the associated material phase.

The following paper mainly refers to problems in a finite deformation, micromechanical framework, where multiple material phases are gathered together in a so-called representative volume element (RVE). Furthermore, the matrix or void material generally fills the space between the different inclusions and a coherent material structure is considered. This assumption allows the application of the principles of standard continuum mechanics to the heterogeneous material. The application of special boundary conditions, consistent with the micromechanical assumptions, finally leads to large material deformations of the internal microstructure. Note that in the following only structured meshes are considered, where a logical mesh direction can be defined, mainly in the direction of the local element coordinate axes. Further informations about these micromechanical assumptions can for instance be found in [1] or [28].

The outline of this paper is as follows. Section 2 briefly refers to the basic continuum mechanical equations in the ALE method and the integration into a finite element framework, including the description of the global solution algorithm and the special features of the multi-material version of the ALE method. Section 3 gives some more informations about the advection process, the basic equations and some fundamental requirements for the solution scheme of the advection process as well as a closer discussion of the distinction between volume- and material-associated quantities. In Sect. 4 and 5 finally, the advection algorithms for both types of quantities are described and respective numerical examples are given. The paper will be finished with a summary in Sect. 6.

2 Arbitrary Lagrangian–Eulerian finite element method

The description of the motion within an ALE framework is based on an extension of the classical theory of large deformation, non-linear continuum mechanics ([45, 65]). Since this extension of the kinematical relations and the derivation of the governing equations are nowadays standard and can be found in various publications and textbooks, the following section will only give a short overview of the most important aspects concerning the advection process. Further details can be found in e.g. [8, 10, 22, 33, 34, 57] or [42].

2.1 ALE-kinematical description

In a Lagrangian description of the motion, the deformation of a material point X in n spatial dimensions is given in terms of the mapping function $\boldsymbol{\varphi}(\mathbf{X}, t) : \mathcal{R}^n \times \mathcal{R} \rightarrow \mathcal{R}^n$ that in general is a function of time t and the initial position $\mathbf{X}$

$$\mathbf{x}(\mathbf{X}, t) = \boldsymbol{\varphi}(\mathbf{X}, t). \tag{1}$$

Here the initial configuration Ω_0 with associated coordinates $\mathbf{X} \in \mathcal{R}^n$ and the spatial configuration Ω with coordinates $\mathbf{x} \in \mathcal{R}^n$ describe the undeformed and the deformed configuration, respectively. However, in an ALE point of view, additionally an independent referential configuration $\hat{\Omega}$ with time dependent coordinates $\boldsymbol{\chi}(t) \in \mathcal{R}^n$ is introduced. In a discrete finite element sense, this configuration usually coincides with the position of the finite element mesh nodes. The total deformation map Eq. (1) can subsequently be described with respect to these intermediate coordinates. Therefore, two time varying, generic mapping functions $\boldsymbol{\Psi}(\boldsymbol{\chi}(t), t) : \mathcal{R}^n \times \mathcal{R} \rightarrow \mathcal{R}^n$

and $\boldsymbol{\Phi}(\boldsymbol{\chi}(t), t) : \mathcal{R}^n \times \mathcal{R} \rightarrow \mathcal{R}^n$ are introduced that define the relations between these different configurations

$$\begin{aligned} \boldsymbol{\Psi}\big(\boldsymbol{\chi}, t\big): &\quad \boldsymbol{\chi}(t) \rightarrow \mathbf{X}\big(\boldsymbol{\chi}, t\big), \\ \boldsymbol{\Phi}\big(\boldsymbol{\chi}, t\big): &\quad \boldsymbol{\chi}(t) \rightarrow \mathbf{x}\big(\boldsymbol{\chi}, t\big), \end{aligned} \tag{2}$$

i.e. these functions map referential points $\boldsymbol{\chi}(t)$ in the referential configuration $\hat{\Omega}$, to initial points $\mathbf{X}(\boldsymbol{\chi}, t)$, defined in the initial configuration $\Omega_0 = \Psi(\hat{\Omega})$ and spatial points $\mathbf{x}(\boldsymbol{\chi}, t)$, defined in the spatial configuration $\Omega = \Phi(\hat{\Omega})$ (cf. Fig. 1). The total deformation map Eq. (1) can then be written as

$$\begin{aligned} &\mathbf{x} = \boldsymbol{\varphi}(\mathbf{X}, t) = \boldsymbol{\Phi}\big(\boldsymbol{\chi}, t\big) = \boldsymbol{\Phi}\big(\boldsymbol{\Psi}^{-1}(\mathbf{X}(\boldsymbol{\chi}, t), t), t\big) \\ \rightarrow \quad &\boldsymbol{\varphi} = \boldsymbol{\Phi} \circ \boldsymbol{\Psi}^{-1}. \end{aligned} \tag{3}$$

The fundamental difference to a Lagrangian description is that the initial configuration $\mathbf{X}(\boldsymbol{\chi}, t)$ now becomes a function of time and the association between material particles and points in the referential configuration, i.e. points, accessible in the finite element mesh, can change. This leads to the characteristic non-Lagrangian nature of the ALE description where additional flow effects of the material phases and the solution variables through the computational domain have to be taken into account.

2.2 General time derivatives

The explicit time dependency of the referential coordinates $\boldsymbol{\chi}(t)$ leads to an additional term in the material time derivative of a general space and time dependent scalar quantity $\phi(\boldsymbol{\chi}, t)$ that can be given as

$$\dot{\phi}|_{\mathbf{x}} = \frac{\mathrm{d}\phi(\boldsymbol{\chi}, t)}{\mathrm{d}t} = \left.\frac{\partial \phi(\boldsymbol{\chi}, t)}{\partial t}\right|_{\chi} + \operatorname{grad} \phi(\boldsymbol{\chi}, t) \cdot \mathbf{c}. \tag{4}$$

$(\dot{\bullet})|_{\mathbf{x}} = \frac{\mathrm{d}(\bullet)}{\mathrm{d}t}$ refers to the material time derivative at fixed initial coordinates $\mathbf{X}$, while $(\dot{\bullet})|_{\chi}$ holds the referential coordinates fixed and is thus a local time derivative of the quantity $(\bullet)$ with respect to $\boldsymbol{\chi}$. In the above equation, the time derivative has been decomposed into a local derivative at fixed referential coordinates, describing the change of ϕ with respect to this referential configuration, and in a convective part that considers the relative motion of the referential configuration with respect to the initial configuration. The convective velocity

$$\mathbf{c} = \mathbf{v} - \hat{\mathbf{v}} \quad \text{with} \quad \mathbf{v} = \left.\frac{\partial \mathbf{x}}{\partial t}\right|_{\mathbf{x}} \quad \text{and} \quad \hat{\mathbf{v}} = \left.\frac{\partial \mathbf{x}}{\partial t}\right|_{\chi}, \tag{5}$$

gives the relative motion of the velocity of the material particles $\mathbf{v}$ to the mesh velocity $\hat{\mathbf{v}}$, i.e. the velocity of the material through the finite element mesh and the convective derivative thus denotes a flux of the variable ϕ.

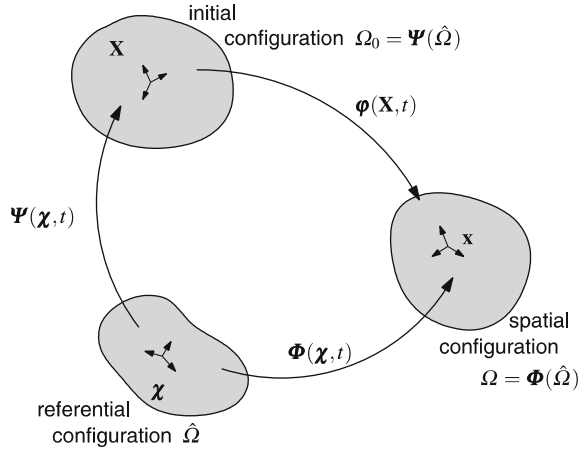

Fig. 1 Mapping relations between the three ALE configurations

2.3 Governing equations and variational form

The set of governing equations, necessary for the implementation of a finite deformation finite element analysis, are given by the balance of mass, momentum and energy. Note that in contrast to a Lagrangian approach, where the balance of mass is usually fulfilled by construction, the density has to be balanced explicitly to account for the conservation of mass during the non-Lagrangian deformation. If furthermore inelastic effects, like plasticity, viscoelasticity or damage have to be accounted for, additional evolution equations for the internal variables are to be considered. These equations can be written in a general form, similar to Eq. (4)

$$\begin{aligned} &\frac{\mathrm{d}\boldsymbol{\phi}(\mathbf{x}, t)}{\mathrm{d}t} = \boldsymbol{\mathcal{S}}(\mathbf{x}, t) \\ \rightarrow \quad &\left.\frac{\partial \boldsymbol{\phi}(\mathbf{x}, t)}{\partial t}\right|_{\chi} + \operatorname{grad} \boldsymbol{\phi}(\mathbf{x}, t) \cdot \mathbf{c} = \boldsymbol{\mathcal{S}}(\mathbf{x}, t), \end{aligned} \tag{6}$$

where the vector $\boldsymbol{\phi}$ consists of the scalar quantities ϱ, v_i, e and α_i

$$\boldsymbol{\phi} = \big\{\varrho, v_i, e, \alpha_i\big\}^{\mathrm{T}} \tag{7}$$

for the material density ϱ, the components of the material velocity v_i, the internal energy e and a set of n history variables α_i $(i = 1, \ldots, n)$. The general vector $\boldsymbol{\mathcal{S}}$ denotes a source term that describes the local changes of the quantities $\boldsymbol{\phi}$ and is derived from the governing equations.

In a finite element analysis, the coupled set of non-linear field equations (6) is transferred into a variational form by multiplication with a test function $\delta\boldsymbol{\phi} \in \bar{\mathcal{V}}^{\phi}$ and integration over the computational domain $\mathcal{B}$

$$\begin{aligned} \int_{\mathcal{B}} \delta\boldsymbol{\phi} \cdot \big(\dot{\boldsymbol{\phi}}|_{\chi}(\mathbf{x}, t) + \operatorname{grad} \boldsymbol{\phi}(\mathbf{x}, t) \cdot \mathbf{c}\big)\, \mathrm{d}v = \\ \int_{\mathcal{B}} \delta\boldsymbol{\phi} \cdot \boldsymbol{\mathcal{S}}(\mathbf{x}, t)\, \mathrm{d}v. \end{aligned} \tag{8}$$

The function space $\mathcal{V}^{\phi}$ is associated with the function $\boldsymbol{\phi}$, while the test function space $\bar{\mathcal{V}}^{\phi}$ is associated with the test function $\delta\boldsymbol{\phi}$ and fulfills the homogeneous Dirichlet boundary conditions. In a Bubnov–Galerkin approach, $\delta\boldsymbol{\phi} \in \bar{\mathcal{V}}^{\phi}$ is usually expected to fulfill the same smoothness requirements as the solution variable $\boldsymbol{\phi} \in \mathcal{V}^{\phi}$ itself.

2.4 Global solution approach for the coupled ALE equations

Equations (6) represents a coupled set of equations for the material velocity $\mathbf{v}$ and the convective velocity $\mathbf{c}$, or their discrete displacement increment counterparts $\Delta\mathbf{u}$ and $\Delta t\,\mathbf{c}$, respectively. The convective velocity is usually prescribed by an appropriate mesh motion scheme that minimizes the mesh distortions and retains a uniform mesh geometry throughout the deformation process. A summary of such mesh motion schemes can for instance be found in [5, 38, 49] or [25] and should not be referred here in more detail. The coupled equations describe two different phenomena. First the motion of the material is prescribed by the Lagrangian governing equations, while simultaneously the relocation of the mesh nodes leads to a flux of the material and the current solution state through the mesh. The fractional-step or operator-split solution approach (see e.g. [20, 61] or [10]) directly considers these two phenomena by dividing the coupled equation into two subproblems. The first subproblem considers a purely Lagrangian approach and determines the physical material deformations according to the balance laws and the constitutive equations. Neglecting the convective effects, Eq. $(6)_2$ reduces to

$$\left.\frac{\partial \boldsymbol{\phi}(\mathbf{x}, t)}{\partial t}\right|_{\chi} = \boldsymbol{\mathcal{S}}(\mathbf{x}, t). \tag{9}$$

To account for the relative motion of the mesh configuration with respect to the material, an additional transport step is performed afterwards. Here first the mesh nodes are relocated to their new position and subsequently a transport of the solution is performed that finally results in the solution of the homogeneous, linear advection equation

$$\left.\frac{\partial \boldsymbol{\phi}(\mathbf{x}, t)}{\partial t}\right|_{\chi} + \operatorname{grad} \boldsymbol{\phi}(\mathbf{x}, t) \cdot \mathbf{c} = \mathbf{0}. \tag{10}$$

Note that this approach can be seen as an explicit solution procedure where no direct interactions between both steps are considered. Indeed the operator-split method enables the use of special-purpose solution algorithms for both parts. For the Lagrangian step [Eq. (9)], standard finite element procedures can be applied with slight modifications, while the advection step can be implemented very efficiently using the extensive experiences of the fluid dynamics community, where the advection equation is a common problem to solve. The remainder of the paper will mainly deal with an efficient and accurate implementation of this transport step.

2.5 Single- and multi-material ALE methods

Another important decision concerning the implementation of the ALE approach and the advection step is the handling of the material boundaries in a computational domain with multiple materials. Generally, two approaches are conceivable (cf. Fig. 2). In the first approach, the material boundaries are resolved directly by the finite element mesh, where the mesh nodes remain aligned to the boundaries throughout the whole deformation process in a Lagrangian sense. Therefore, each element consists of only one type of material and no material fluxes over element boundaries have to be considered during the advection process. This approach is also denoted as the SALE method, is relatively easy to implement and represents the most common strategy in the recent ALE literature (see e.g. [3, 57] or [6], amongst others).

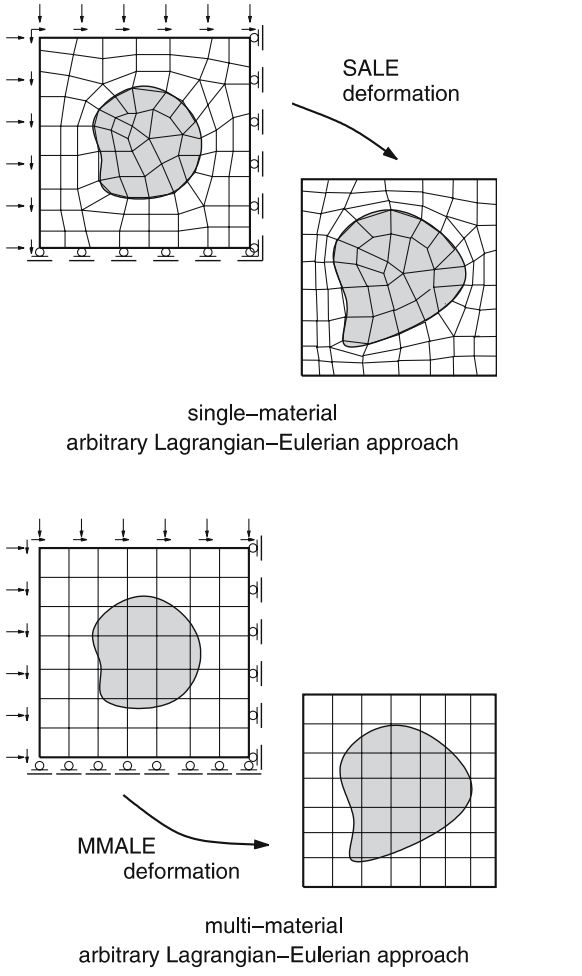

Fig. 2 2D illustration of the basic idea of the single-material ALE approach (SALE – *top*) and the multi-material ALE approach (MMALE – *bottom*) using a micromechanical, single inclusion system

However this approach restricts the mesh motion scheme considerably and for some applications, e.g. large deformation micromechanical problems, it is advantageous to apply so-called MMALE approaches, where the material boundaries can run freely through the finite element discretization (cf. e.g. [10, 12, 49]). This implies that special elements have to be incorporated that are able to deal with multiple material properties. In the remainder, these elements will be referred to as mixed elements and the material occurrences will be accounted for using the VOF [32], where each material phase k is considered only by its element volume fraction $f^k \in \mathcal{R}$, defined by

$$f^k = \frac{1}{V}\int_{\Omega^k} \mathrm{d}v^k = \frac{V^k}{V}$$
$$\text{and} \quad \sum_k V^k = V, \quad \sum_k f^k = 1. \tag{11}$$

Ω^k represents the portion of the elements region Ω, associated with material k, while V and V^k are the total element volume and the volume of material k, respectively. Material k completely fills the element if $f^k = 1.0$, adopts only a partial element volume if $0.0 < f^k < 1.0$ and is not present within the element if $f^k = 0.0$. In the VOF approach, effective element properties are computed by applying so-called mixture theories on the element level, based on averaging theorems for the element variables (see e.g. [10] or [12]). In the discrete case, these effective element properties $\bar{\phi}$ are computed as a weighted sum of the different material-associated properties ϕ^k

$$\bar{\phi} = \sum_k \phi^k f^k$$
$$\text{e.g.} \quad \bar{\boldsymbol{\sigma}} = \sum_k \boldsymbol{\sigma}^k f^k \quad \text{or} \quad \bar{\varrho} = \sum_k \varrho^k f^k, \tag{12}$$

for the averaged Cauchy-stresses $\bar{\boldsymbol{\sigma}}$ and the averaged material density $\bar{\varrho}$, respectively. Subsequently, these effective properties are inserted into the governing equations to compute the finite element matrices and vectors. However, one restriction in this approach is the assumption of a uniform distribution of the solution variables, which leads to an element-wise spatially constant gradient and allows the application of the element mixture theories. This uniform distribution can for instance be achieved by a reduced integration scheme of the element integrals and linear ansatz spaces for the displacements and velocities, where the element matrices are evaluated only in the element center. This reduced integration scheme leads to a rank deficiency of the element stiffness matrix and special stabilization techniques have to be applied, which is indeed not a topic of this work and the reader is referred to the corresponding literature (e.g. [7, 53] or [14]).

2.6 Finite element discretization

The governing equations in the variational form, given by Eq. (8), specify a coupled system of partial differential equations.

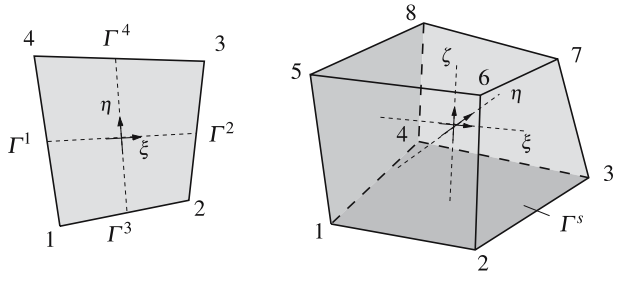

Fig. 3 Two- and three-dimensional finite element with node, edge and surface definitions

Since a closed-form solution is usually not applicable, a spatial discretization with finite elements is performed, where the continuous body $\mathcal{B}$ is discretized by a set of n_e non-overlapping finite elements $\Omega^e \subset \mathcal{B}^h$. Thus $\mathcal{B}^h$ is a spatial approximation of the physical body $\mathcal{B}$. Similarly, the physical boundary $\partial\mathcal{B}$ is approximated by the discrete boundary $\partial\mathcal{B}^h$ of the finite element discretization that is a subset of the union of all element boundaries $\partial\Omega^e$. Finally, the boundary of one finite element can be separated into n_f element surfaces Γ^s

$$\mathcal{B} \approx \mathcal{B}^h = \bigcup_{e=1}^{n_e} \Omega^e \quad \text{resp.}$$
$$\partial\mathcal{B} \approx \partial\mathcal{B}^h \subset \bigcup_{e=1}^{n_e} \partial\Omega^e \quad \text{and} \quad \partial\Omega^e = \bigcup_{s=1}^{n_f} \Gamma^s. \tag{13}$$

The following derivations should be restricted to 2D quadrilateral and 3D hexahedral elements with bi- and tri-linear ansatz spaces, respectively. Generally these elements consist of four vertices and four straight edges in the two-dimensional case, whereas the three dimensional elements consist of eight vertices, twelve straight edges and six ruled surfaces that do not necessarily lie in a plane if the element is arbitrarily distorted (cf. Fig. 3).

As mentioned before, only linear shape functions will be considered, where in the isoparametric concept the spatial coordinates $\mathbf{x}^e$ and the displacement $\mathbf{u}^e$ and velocity $\mathbf{v}^e$ are likewise interpolated using the same shape functions $N_\mathrm{I}(\boldsymbol{\xi})$, defined for each element node I

$$\mathbf{x}^e = \sum_\mathrm{I} N_\mathrm{I}(\boldsymbol{\xi})\, \mathbf{x}_\mathrm{I} \quad \text{and}$$
$$\mathbf{u}^e = \sum_\mathrm{I} N_\mathrm{I}(\boldsymbol{\xi})\, \mathbf{u}_\mathrm{I}, \quad \text{resp.} \quad \mathbf{v}^e = \sum_\mathrm{I} N_\mathrm{I}(\boldsymbol{\xi})\, \mathbf{v}_\mathrm{I}. \tag{14}$$

$\mathbf{x}_\mathrm{I}$ denote the nodal coordinates, while $\mathbf{u}_\mathrm{I}$ and $\mathbf{v}_\mathrm{I}$ refer to the nodal displacements and velocities, respectively.

In the following derivations, the volume- and surface integrals are required. To obtain an efficient approach, especially for the three dimensional hexahedral elements, analytic solutions rather than numerical approximations are preferred. These can be derived using the divergence theorem $\operatorname{div}(\phi\,\boldsymbol{\psi}) = \operatorname{grad}\phi\cdot\boldsymbol{\psi} + \phi \operatorname{div}\boldsymbol{\psi}$ for a vector-valued function $\boldsymbol{\psi} \in \mathcal{R}^n$ and a scalar $\phi \in \mathcal{R}$. Integrating over the element volume and choosing $\phi = 1$ and $\boldsymbol{\psi} = \mathbf{x}$ gives

$$\int_{\Omega^e} \operatorname{div}\mathbf{x}\,\mathrm{d}v = \int_{\partial\Omega^e} \mathbf{x}\cdot\mathbf{n}\,\mathrm{d}a = \sum_{s=1}^{n_s}\int_{\Gamma^s} \mathbf{x}\cdot\mathbf{n}^s\,\mathrm{d}\Gamma^s, \tag{15}$$

with $\operatorname{div}\mathbf{x} = 2$ for the two dimensional and $\operatorname{div}\mathbf{x} = 3$ for the three dimensional case. The integral over the element surface is divided into the integrals over each surface s of the element with outward unit normal vector $\mathbf{n}^s$. For the two dimensional case, the surface integration is trivial and can be performed by choosing the center point $\mathbf{x}^s$ of each polygon edge with length l^s, multiplied with the constant normal vector $\mathbf{n}^s$

$$A = \frac{1}{2}\int_{\Gamma^s} \mathbf{x}\cdot\mathbf{n}^s\,\mathrm{d}\Gamma^s = \frac{1}{2}\,\boldsymbol{x}^s\,\boldsymbol{n}^s\,l^s. \tag{16}$$

$\boldsymbol{x}^s = \frac{1}{2}\left(\boldsymbol{x}_1^s + \boldsymbol{x}_2^s\right)$ gives the coordinates of the center point of the element edge, while $\boldsymbol{x}_1^s$ and $\boldsymbol{x}_2^s$ are now the vectors of the local vertices, defining the element edge. The normal vector can be given directly as

$$\boldsymbol{n}^s = \frac{1}{l^s}\begin{pmatrix} y_2^s - y_1^s \\ -x_2^s + x_1^s \end{pmatrix} \tag{17}$$

with edge length $l^s = ||\boldsymbol{x}_2^s - \boldsymbol{x}_1^s||_2$. The total two-dimensional element volume, defined by n_f edges, can then be written as

$$A^e = \frac{1}{2}\sum_{s=1}^{n_f}\left(x_1^s\, y_2^s - x_2^s\, y_1^s\right). \tag{18}$$

For the three-dimensional case, the solution of Eq. (15) is much more complicated (cf. [24] or [39]). It is based on the parameterization of each ruled hexahedral surface s using the tri-linear shape functions that reduce to bi-linear functions on the surface in terms of the local coordinates ξ and η

$$\mathbf{x}^s = \sum_{\mathrm{I}} N_{\mathrm{I}}(\xi, \eta)\, \mathbf{x}_{\mathrm{I}}^s. \tag{19}$$

Again, $\mathbf{x}_{\mathrm{I}}^s$ are the vertices of the ruled surface s (cf. Fig. 4). To simplify the equations, the superscript s will be omitted for the coordinates of the considered surface. The surface element in the local $\xi - \eta$ plane can then be given as

$$\mathrm{d}\boldsymbol{\Gamma}^s = \mathbf{n}^s\, \mathrm{d}\Gamma^s = \left(\frac{\partial \mathbf{x}}{\partial \xi} \times \frac{\partial \mathbf{x}}{\partial \eta}\right) \mathrm{d}\xi\, \mathrm{d}\eta. \tag{20}$$

Inserting the parameterization Eq. (19) into the above form and integrating over the local coordinates $-1 \leq \xi \leq 1$ and $-1 \leq \eta \leq 1$, the surface element can be analytically integrated and we obtain

$$\int_{\Gamma^s} \mathrm{d}\boldsymbol{\Gamma}^s = \frac{1}{2}\,\mathbf{k}, \tag{21}$$

with $\mathbf{k} = (\mathbf{x}_3 - \mathbf{x}_1) \times (\mathbf{x}_4 - \mathbf{x}_2)$. Subsequently, using Eq. (15), the element volume can be given as

$$V^e = \frac{1}{6}\sum_{s=1}^{n_f} \mathbf{x}_0 \cdot \mathbf{k} \quad \text{and} \quad \mathbf{x}_0 = \frac{1}{n_p}\sum_{i=1}^{n_p} \mathbf{x}_{\mathrm{I}}, \tag{22}$$

where $\mathbf{x}_0$ denotes the center point of the surface s at $\boldsymbol{\xi} = \mathbf{0}$, n_f the number of element surfaces and n_p the number of surface nodes.

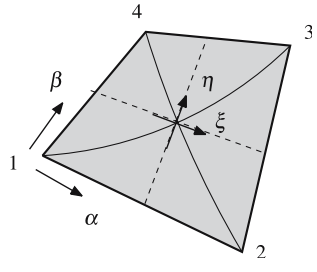

Fig. 4 Ruled surface element and surface parameterizations $(\xi, \eta)/(\alpha, \beta)$

For the following three-dimensional observations, the introduction of an alternative parameterization $(\alpha, \beta) \in [0, 1]$ (cf. Fig. 4) is advantageous, which is indeed equivalent to Eq. (19)

$$\mathbf{x} = \mathbf{x}_1 + \alpha\,(\mathbf{x}_2 - \mathbf{x}_1) + \beta\,(\mathbf{x}_4 - \mathbf{x}_1) + \alpha\,\beta\,\mathbf{d}. \tag{23}$$

The vector $\mathbf{d} = \mathbf{x}_1 - \mathbf{x}_2 + \mathbf{x}_3 - \mathbf{x}_4$ characterizes the deviation of the surface from the plain parallelogram ($\mathbf{d} = \mathbf{0}$). Introducing the cross-vectors $\mathbf{X}_i$, defined for each vertex of the surface element

$$\begin{aligned} &\mathbf{X}_i = (\mathbf{x}_i''' - \mathbf{x}_i) \times (\mathbf{x}_i - \mathbf{x}_i') \\ &\text{with} \quad \mathbf{x}_1' = \mathbf{x}_2, \quad \mathbf{x}_2' = \mathbf{x}_3 \quad \text{and} \quad \mathbf{x}_1''' = \mathbf{x}_4, \end{aligned} \tag{24}$$

with the successor and predecessor nodes $\mathbf{x}_i'$ and $\mathbf{x}_i'''$, respectively, the surface element can also be given as

$$\mathrm{d}\boldsymbol{\Gamma}^s = [\mathbf{X}_1 + \alpha\,(\mathbf{X}_3 - \mathbf{X}_4) + \beta\,(\mathbf{X}_3 - \mathbf{X}_2)]\,\mathrm{d}\alpha\,\mathrm{d}\beta. \tag{25}$$

Performing the integration over the parameters α and β the same results are obtained as in Eq. (22). Incidentally, the determination of the advection volumes in Chapt. 4.3 requires an efficient evaluation of surface integrals of the form

$$\mathcal{F}^s = \int_{\Gamma^s} \mathbf{c} \cdot \mathbf{n}\, \mathrm{d}a, \tag{26}$$

where $\mathbf{c}$ is the vector-valued convective velocity and $\mathbf{n}$ is the outward unit normal to the surface s. Using the above results, the integral can also be written as

$$\mathcal{F}^s = \frac{1}{2}\,\mathbf{c}_0 \cdot \mathbf{k} \quad \text{and} \quad \mathbf{c}_0 = \frac{1}{n_p}\sum_{i=1}^{n_p} \mathbf{c}_i, \tag{27}$$

with the convective velocity $\mathbf{c}_0$, evaluated in the center of the surface s.

3 The advection problem

Physically, the advection process describes a transport of the material and the current solution state through the mesh along the streamlines of the advective flow, provided by the convective velocity $\mathbf{c}$. In an ALE finite element framework this corresponds to a relocation of the finite element nodes by the mesh motion scheme, while the material is held fixed in space. Since an exact solution generally cannot be obtained for an arbitrary distribution of the solution variables in a discrete domain, again we seek a numerical solution procedure that is able to provide a sufficient accurate solution for the advection problem

In the following sections, we consider different solution procedures for the scalar advection problem, where $\boldsymbol{\phi}$ in Eq. (10) is exchanged by a general scalar-valued quantity ϕ. Here, several approaches have been published in the last decades, mainly in the fluid dynamics community. They are based on different ideas, where for example finite element, finite difference and finite volume approaches are applied. In the remainder, solely the latter two approaches should be referred to.

3.1 Basic equations for the advection problem

Mathematically, the transport process is entirely described by the solution of the linear, homogeneous advection equation (10) that can be written for a general space and time dependent scalar field $\phi(\mathbf{x}, t)$ as follows

$$\left.\frac{\partial \phi}{\partial t}\right|_{\chi} + \text{grad}\ \phi \cdot \mathbf{c} = 0 \quad \text{with} \quad \phi(\mathbf{x}, t_0) = \phi_0(\mathbf{x}). \tag{28}$$

The latter equation specifies a set of initial conditions in form of an initial distribution ϕ_0 of the unknown field ϕ at a specific reference time $t = t_0$ which is provided by the preceding Lagrangian step in an ALE finite element method. The exact solution of the above problem can be given as

$$\phi(\mathbf{x}, t) = \phi(\mathbf{x} - t\,\mathbf{c}, t), \tag{29}$$

where the lines $(\mathbf{x} - t\,\mathbf{c})$ are called characteristics and ϕ is constant along these lines.

For the derivation of efficient solution procedures it is often advantageous to rewrite Eq. (28) in a more general representation using the conservative form, also known as the *Euler equation* for the scalar quantity ϕ

$$\left.\frac{\partial \phi}{\partial t}\right|_{\chi} + \text{div}\ \boldsymbol{f}(\phi) = 0 \quad \text{with} \quad \phi(\mathbf{x}, t_0) = \phi_0(\mathbf{x}). \tag{30}$$

$\boldsymbol{f}(\phi)$ now describes the flux of the variable ϕ with the convective velocity $\mathbf{c}$ which is generally a non-linear function of ϕ, whereas in its simplest case, $\boldsymbol{f}(\phi)$ is linear in ϕ and we obtain the linear advection equation with

$$\boldsymbol{f}(\phi) = \phi\,\mathbf{c}. \tag{31}$$

Subsequently, Eq. (30) can also be rewritten as

$$\left.\frac{\partial \phi}{\partial t}\right|_{\chi} + \text{grad}\ \phi \cdot \mathbf{c} = -\phi\,\text{div}\ \mathbf{c}. \tag{32}$$

Comparing the above form with Eq. $(28)_1$, the divergence of the convective velocity must vanish to conform, i.e. the convective flow has to be incompressible. This certainly makes sense, since during the advection process, the material remains fixed in space and only the mesh nodes are relocated to their new positions. No deformation of the material occurs and Eq. (30) reduces to Eq. (28). As a consequence the advection step can be performed by solving either of these two equations.

3.2 General requirements to the advection scheme

Unfortunately, none of the existing numerical approaches provide a solution scheme that solves the advection equation "exactly", in a numerical sense. Therefore, restrictions concerning the quality of the solution have to be accepted. A proper classification of these schemes can be obtained, considering some basic requirements to the solution algorithm. The most important are connected to questions of efficiency, stability and the capability to retain the original shape of the solution distribution throughout the advection process. More extensive details can be found in e.g. [9, 26, 47] or [23].

– *Conservatism of the advection scheme*
In the Lagrangian solution step, some of the solution variables, like the density, the internal energy and the momentum are governed by conservation equations that conserve the quantities during the deformation process. To maintain the magnitudes of these solution variables over the transport step, the advection schemes are required to be conservative in the sense that the value of the solution variable, integrated over the domain Ω, remains constant throughout the advection process, i.e.

$$\Phi^+ := \int_{\Omega^+} \phi^+ \,\mathrm{d}v = \int_{\Omega^-} \phi^- \,\mathrm{d}v =: \Phi^-, \tag{33}$$

where ϕ^- and ϕ^+ denote the values of the scalar-valued and volume-specific solution variable ϕ before and after the advection step, respectively. Furthermore it is highly recommended that also those solution variables that are not governed by a conservation law directly, like strains and stresses fulfill the conservation property.

– *Efficiency, stability and robustness of the advection scheme*
Within a finite element framework, the domain of interest is decomposed into single elements. Therefore the advective flow of the solution variables can be replaced by discrete fluxes over the element boundaries, i.e. by determining the amount of the solution variables and the material, transported in the downstream direction between adjacent elements within a certain time interval. The computation of the flux has only local support and is thus restricted to a small patch of adjacent elements in the direction of the flow. Interactions between non-adjacent elements should be excluded to limit the numerical effort and the accuracy of the advection process. Thus, explicit solution schemes in time can be preferred with respect to implicit schemes. This certainly reduces the numerical effort and influences the efficiency of the numerical scheme considerably. However, explicit schemes are only conditional stable and require the fulfillment of the Courant–Friedrich–Levy (CFL) condition

$$C_r := \frac{|\mathbf{c}|\,\Delta t}{h} \leq 1, \tag{34}$$

where h denotes a characteristic element size and C_r the Courant number. This criterion implies that the material is not allowed to pass an element within one advection step and is thus consistent with the local view of the flux computation.

– *Sufficient order of the approximation*
Another important feature is the approximation order or the consistency error that measures the error arising from the numerical approximation of the original partial differential equation and indicates the degree of the polynomial that is advected by the scheme without error. The error is estimated independently for the time and space discretization, usually by calculating the difference between the

exact and the approximated solution using a Taylor series expansion

$$e = \phi^{\text{ex.}} - \phi^{\text{appr.}}. \tag{35}$$

In [26] extensive analyses of different schemes are performed. While the temporal approximation of explicit schemes is limited to only first-order, the spatial approximation accuracy of the advection scheme should at least be of second order, to obtain an accurate solution algorithm.

– *Monotonicity of the advection scheme*
The requirement for monotonicity of the advection scheme demands that the value of the advected variable ϕ^+ remains within the solution range of the original value ϕ^-. This avoids over- and undershots of the solution that are often produced in common advection schemes. It is obvious that non-monotonic solution schemes are not advisable in advection schemes for finite element procedures, since variables, required to retain within a specific solution range, can violate this requirement. This, for instance, can lead to unphysical negative deformation gradients, densities or energies.

– *Control of the numerical diffusion of the advection scheme*
Most advection schemes, especially the classical first-order methods, show highly numerically diffusive properties, i.e. the solution value decreases and widens in the flow direction or perpendicular to the streamlines (crosswind diffusion). The effect of numerical diffusion or numerical dissipation is independent of the above mentioned criteria, i.e. a stable and conservative scheme can be extremely diffusive. Physically, the numerical diffusion is described by terms containing the second-order spatial derivative of the advected variable ϕ. Especially within the linear advection equation, terms containing the second derivative with respect to time can be transformed into pure diffusion terms

$$\frac{\partial \phi}{\partial t} = -\frac{\partial \phi}{\partial \mathbf{x}} \cdot \mathbf{c} \quad \rightarrow \quad \frac{\partial^2 \phi}{\partial t^2} = \mathbf{c}\, \frac{\partial^2 \phi}{\partial \mathbf{x}^2}\, \mathbf{c}. \tag{36}$$

This observation suggests that almost all explicit advection schemes are expected to be numerically diffusive, since the second derivative of ϕ with respect to the time occurs in the consistency error. In particular, it can be observed that in case of first-order accurate advection schemes, the second-order spatial derivatives lead to large numerically dissipative results.

Concerning advection approaches, applicable for an ALE finite element simulation, next to the mandatory stability, the two most important properties are probably the requirement for conservatism and monotonicity. These properties are responsible for a physically meaningful solution that fulfills the conservation requirements of the governing equations and thus retains the total value of the solution variables throughout the advection process. The effect of the numerical diffusion is important to consider if the Courant number exceeds a critical value. Since the stability of the scheme cannot be guaranteed any more, the transport step has to be splitted into multiple advection steps, based on intermediate mesh configurations. In such case, an advection scheme with only a small amount of diffusion is preferable to retain the spatial shape of the solution variable properly.

3.3 Volume- and material-associated quantities

In a conventional Lagrangian-based finite element framework or a SALE analysis, the material boundaries are properly resolved by the finite element mesh during the whole deformation process. Therefore no fluxes of different material phases across element boundaries have to be considered for. This implies that only homogeneous materials and solution variables have to be dealt with in the advection step, the material distribution does not have to be taken into account and all solution quantities can be treated as volume-associated variables.

However, in a MMALE framework materials are allowed to flow arbitrarily through the finite element discretization and thus fluxes of different material phases can occur over certain element boundaries. This requests the distinction between two different kinds of variables. The first kind is again not associated with a certain material phase and is therefore independent of the material distribution. Here, mostly elastic strain-like variables, like the deformation gradient $\mathbf{F}$ or the right and left Cauchy-Green tensors $\mathbf{C}$ and $\mathbf{b}$, respectively, are referred to. On the contrary, material-associated quantities are directly associated with a certain material phase k and thus the material distribution within a mixed element becomes very important in the advection step. Examples for those quantities are e.g. the stresses $\boldsymbol{\sigma}^k$, the density ϱ^k, the volume fraction f^k or special, material-associated internal variables (e.g. plastic strains). To account for the material-associated conservation properties, the amount of material, and thus of the solution variable, transported between adjacent elements has to be determined. This leads to a different treatment of volume- and material-associated quantities and two different advection algorithms will be considered in the following that are both based on the solution of the conservation form of the advection problem, given in Eq. (30).

In the following two sections, first the advection process for purely volume-associated variables is reviewed, where the material distribution is not relevant. Subsequently, the advection process for the material-associated variables is presented, based on the VOF as a special algorithm to trace the motion of the materials and their interfaces.

4 Advecting volume-associated quantities

As pointed out before, volume-associated variables are variables occupying an arbitrary distribution within the computational domain without direct connection to the different material phases. In a hyperelastic ALE finite element method these quantities can for instance be strain-like variables, like the deformation gradient or the left Cauchy-Green tensor. To avoid the computation of the total deformation map on

the element level, these quantities can be treated as history variables to store the deformation history of the referential configuration (cf. Eq. (3) and [57]). To advect these quantities accurately, special care has to be taken concerning the choice of the corresponding advection algorithms. In particular the effect of the numerical diffusion has to be minimized and the fulfillment of the monotonism properties are highly recommended (cf. Sect. 3.2).

In this context, a huge number of different solution schemes in one and multiple spatial dimensions and of different orders of accuracy has been published. However within the fractional-step method, the transport step is usually performed frequently after a sequence of Lagrangian steps to smooth the deformed mesh. Therefore an efficient implementation of this step is of fundamental importance to avoid a stagnation of the overall analysis progress. In the following, two types of general approaches, applicable for an ALE finite element method, will be discussed in more detail. The first approach is based on a direct and point-wise solution of the advection equations using a C^0 continuous approximation of the generalized solution variable ϕ, while the second approach represents a more general class of solution schemes and is based on finite volume methods. For comparisons to other schemes, found in the literature, the reader is referred to publications like e.g. [10, 26, 23, 58, 64, 66] or [19].

4.1 A simple test problem

A convenient strategy for the analysis of advection methods, especially of finite-difference and finite-volume-based schemes, is first to develop the scheme for a simple one-dimensional problem, where a wave or a discontinuity is transported through a fixed mesh with equidistant grid nodes and a uniform velocity. In this case, dimensional effects and influences arising from non-orthogonal mesh topologies can widely be excluded. In the following, the different advection schemes are therefore first applied to a pseudo-2D test example, depicted in Fig. 5, where the advection schemes are implemented for the general 2D case, while the flow is only one-dimensional on an equidistant finite element grid. The extension to multiple spatial dimensions can be done in several ways and is referred to in Sect. 4.6.

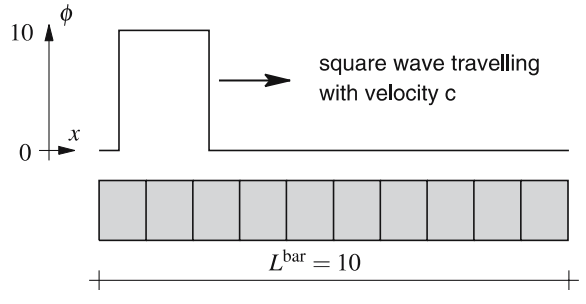

Fig. 5 Pseudo two-dimensional system with a square wave traveling with the convective velocity c

4.2 Direct solution scheme for the advection equation

A simple and straight-forward method to solve the advection equation (28) for the scalar quantity ϕ is the direct evaluation of the hyperbolic part on the integration point level of a finite element. Therefore, Eq. (28) is integrated in time using an explicit time-integration scheme

$$\dot{\phi}|_\chi \approx \frac{\phi^+ - \phi^-}{\Delta t} \quad \rightarrow \quad \phi^+ = \phi^- - \Delta t \ \text{grad}\ \phi \cdot \mathbf{c}, \tag{37}$$

where ϕ^- and ϕ^+ are the values of ϕ at the integration points before and after the advection process, respectively. Since no physical time is associated with the advection step, Δt acts as a pseudo time, such that $\Delta \mathbf{u_c} = \Delta t\, \mathbf{c}$ refers to the convective displacement increment, prescribed by the node relocation scheme.

As discussed before, ϕ is usually a derived element-based variable, stored at the integration points and is consequently discontinuous over the edges of adjacent elements. However the evaluation of the spatial gradient of ϕ requires an – at least – C^0 continuous approximation of the quantity ϕ that for instance can be obtained by a least-squares interpolation (see e.g. [69]). The vector of nodal values $\hat{\boldsymbol{\phi}} = [\hat{\phi}_I]$ is determined from the values at the integration points $\bar{\phi}$ according to the following implicit equation

$$\boldsymbol{V}\, \hat{\boldsymbol{\phi}} = \boldsymbol{R} \tag{38}$$

with $\boldsymbol{V} = [V_{IJ}] = \int_\Omega N_{\text{I}}^\phi\, N_J^\phi \, \text{d}v$ representing a consistent volume matrix and the corresponding right-hand side $\boldsymbol{R} = [R_{\text{I}}] = \int_\Omega N_{\text{I}}^\phi\, \bar{\phi}\, \text{d}v$, containing the discrete values $\bar{\phi}$. Generally, N_{I}^ϕ can be chosen to be identical with the isoparametric shape functions of the finite element displacement interpolation. To obtain an efficient, explicit approach, the volume matrix can further be lumped, for instance by using the row-sum criterion. Subsequently, a C^0-continuous interpolation and the discrete gradient $\text{grad}^h\, \phi$ can be obtained element-wise according to

$$\hat{\phi} = \sum_{\text{I}} N_{\text{I}}^\phi\, \hat{\phi}_{\text{I}} \quad \rightarrow \quad \text{grad}^h\, \hat{\phi} = \sum_{\text{I}} \hat{\phi}_{\text{I}} \otimes \text{grad}\ N_{\text{I}}^\phi. \tag{39}$$

The application of this advection scheme represents an easy to implement procedure, since no fluxes over the edges of adjacent elements have to be computed and thus no information about the element neighborhood is required. Unfortunately, it can be observed that this formulation shows numerical instabilities, depending on the size of the convective displacement increment. Fig. 6 (above) shows the result for the problem, depicted in Fig. 5, where an initial square wave is transported along a spatially fixed bar with a uniform mesh, consisting of 30×1 elements. The Courant number is chosen to be $C_r = 1/2$. The square wave already disperses after a few time steps and the solution degenerates considerably. As reported in [34], these spatial instabilities can mostly be avoided using a local and global smoothing procedure [31]. The local smoothing procedure implies an initial smoothing of ϕ on the element level by using the

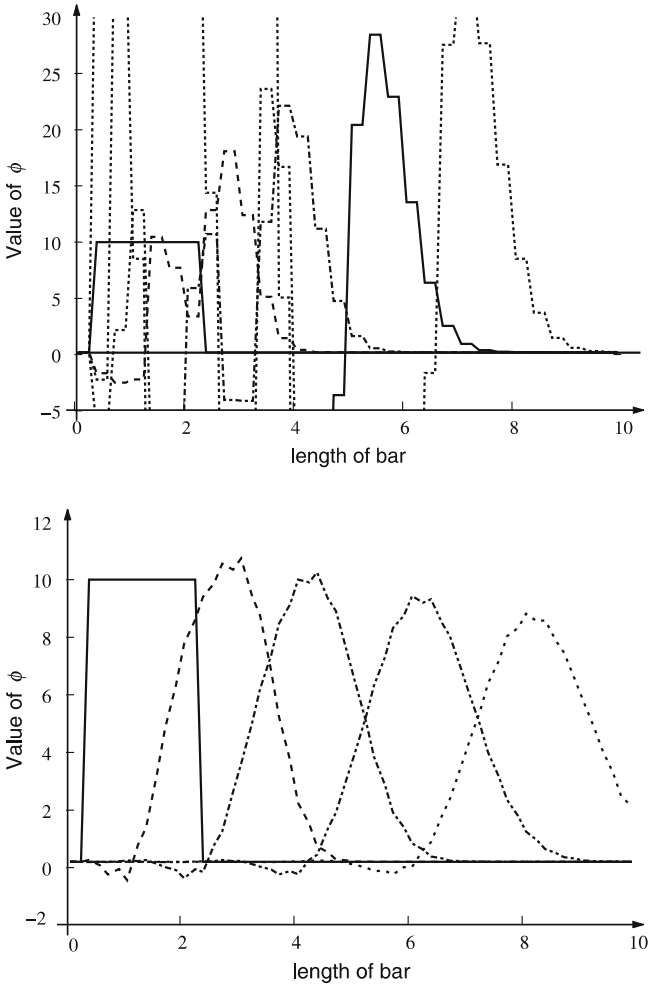

Fig. 6 Solution of the advection problem using the direct advection approach (Courant number $C_r = 1/2$, 60 advection steps), *top*: direct solution of the advection equation, *bottom*: local and global smoothing procedure (mesh density: 30 elements in x-direction)

element average value for the computation of the right-hand side $\boldsymbol{R}$ in Eq. (38)

$$\bar{\phi} \quad \leftarrow \quad \frac{1}{V} \int_{\Omega} \bar{\phi} \, \mathrm{d}v, \tag{40}$$

with the element domain Ω and the element volume V. Note that in case of a reduced integration procedure in the multi-material ALE framework, this step is certainly obsolete. The global smoothing procedure implies the substitution of ϕ^- in Eq. $(37)_2$ with the interpolated value $N_{\mathrm{I}} \hat{\phi}_{\mathrm{I}}$

$$\phi^+ = \sum_{\mathrm{I}} N_{\mathrm{I}}^{\phi} \, \hat{\phi}_{\mathrm{I}}^- - \Delta t \sum_{\mathrm{I}} \hat{\phi}_{\mathrm{I}}^- \otimes \mathrm{grad} \; N_{\mathrm{I}}^{\phi} \cdot \mathbf{c}. \tag{41}$$

The evolution of the solution with time is shown in Fig. 6 (bottom). Although this stabilization scheme reduces the spatial instability considerably, the distribution of the solution variable shows over- and undershots that lead to unphysical values of ϕ. Additionally, the square is rounded off, while the peak value decreases with time, i.e. the solution is numerical diffusive. Indeed, if C_r exceeds the value of $1/2$, the solution is dominated by extremely large over- and undershots and is not comparable to the exact solution any more.

More improved results can be obtained using a weighted global smoothing procedure, where the integration point values are computed by a weighted sum of Eqs. $(37)_2$ and (41)

$$\phi^+ = (1-\alpha)\, \phi^- + \alpha \sum_{\mathrm{I}} N_{\mathrm{I}}^{\phi} \, \hat{\phi}_{\mathrm{I}}^- - \Delta t \sum_{\mathrm{I}} \hat{\phi}_{\mathrm{I}}^- \otimes \mathrm{grad} \; N_{\mathrm{I}}^{\phi} \cdot \mathbf{c}. \tag{42}$$

Note that the weighting factor α is not necessarily expected to be between 0 and 1. Figure 7 shows the solution of the square wave for Courant numbers of $1/3$ and $7/10$, while the weighting parameter is chosen to be 0.56 and 1.7, respectively.

Unfortunately, this approach implies a number of problems. First of all, the range of α that leads to an accurate

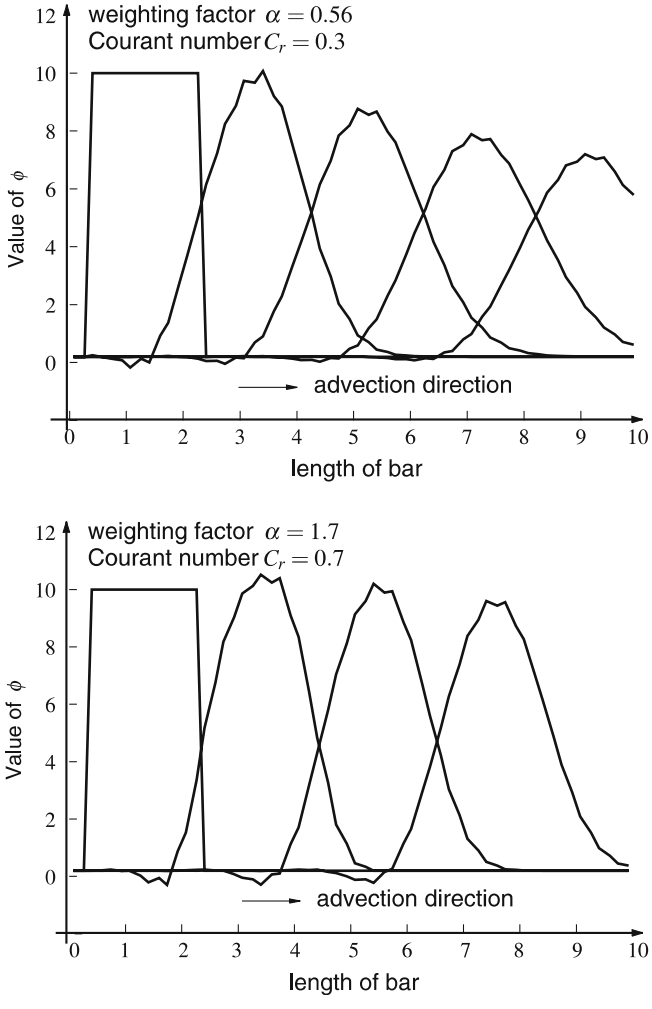

Fig. 7 Solution of the advection problem with weighted global smoothing *top*: $C_r = 1/3$ with $\alpha = 0.56$ and 100 advection steps, *bottom*: $C_r = 7/10$ with $\alpha = 1.7$ and 43 advection steps (mesh density: 30 elements in x-direction)

solution is very small. Therefore, only small perturbations of α suffice to deteriorate the solution considerably. In [34] a broad range for the weighting factor is proposed, based on the local Courant number C_r

$$C_r \leq \alpha \leq 2\, C_r. \tag{43}$$

Indeed, this choice is not sufficient to obtain an accurate solution for the advection problem. But even if α is estimated correctly, the shape of the initial square wave is not maintained, rather it is deformed considerably, especially at a – numerically diffusive – low Courant number. In case of a high Courant number, slight undershots in front of the steep gradient still occur. Furthermore, it is highly recommended that the volume-associated advection approach can be extended to the material-associated advection approach to maintain the efficiency and limit the numerical effort of the total advection process. Hence, this approach does not consider explicitly the distribution of different material phases since they are only given implicitly as discrete quantities at the integration points. During the smoothing process, the material properties are distributed to the contiguous elements and the C^0-continuous representation accounts for the different materials only in a very rough and smeared sense.

4.3 Finite-volume based methods

Another solution approach is given by a class of finite volume methods that are usually constructed for the solution of the conservative Euler equation, given in Eq. (30). In practical numerical solution algorithms, this equation is discretized element-wise in a volume-integrated form. The resulting approach guarantees global conservation of the variable ϕ within the control volume. Using the divergence theorem, the integration over the element domain Ω gives

$$\int_\Omega \left.\frac{\partial \phi}{\partial t}\right|_\chi \mathrm{d}v = -\int_\Omega \operatorname{div} \boldsymbol{f}(\phi)\, \mathrm{d}v = -\int_{\partial\Omega} \boldsymbol{f}_\phi \cdot \mathbf{n}\, \mathrm{d}a, \tag{44}$$

where $\partial\Omega$ is the boundary of the element domain with unit normal vector $\mathbf{n}$. In the latter relation, the flux $\boldsymbol{f}$ is exchanged by the surface flux vector $\boldsymbol{f}_\phi$ associated with the variable ϕ that is an approximation of the value of $\boldsymbol{f}(\phi)$ on the boundary of the domain Ω. Furthermore, the boundary integral can be divided into the sum of the integrals over the n element surfaces Γ and we obtain

$$\int_\Omega \left.\frac{\partial \phi}{\partial t}\right|_\chi \mathrm{d}v = -\sum_{s=1}^{n} \int_{\Gamma^s} \boldsymbol{f}_\phi^s \cdot \mathbf{n}^s\, \mathrm{d}a. \tag{45}$$

In the case that multiple integration points are considered within the element, the distribution of ϕ is non-constant. This leads to some difficulties to account – numerically – for the conservation of the quantity. Therefore, instead of the discrete values at the integration points, the volumetric average $\bar{\phi}$ of the variable ϕ in the element domain is used

$$\bar{\phi}(t) = \frac{1}{V} \int_\Omega \phi(\mathbf{x}, t)\, \mathrm{d}v. \tag{46}$$

To obtain an efficient solution procedure, again an explicit solution in time of the advection equation is pursued. This can be achieved using an explicit forward-Euler time-integration scheme for the approximation of the local time derivative [cf. Eq. (37)]

$$\left.\frac{\partial \bar{\phi}}{\partial t}\right|_\chi \approx \frac{\bar{\phi}^+ - \bar{\phi}^-}{\Delta t}. \tag{47}$$

Again, $-$ and $+$ denote the values of ϕ before and after the advection step, respectively, and Δt is the pseudo-time increment of the advection step. To avoid unphysical oscillations of the solution, an upwinding procedure has to be included for the evaluation of the volume integrals and the numerical fluxes (see e.g. [35]), where the informations to compute the numerical flux $\boldsymbol{f}_\phi$ and the volume integral on the right-hand side of the above equation are taken from the upstream elements. Thus, a volume-weighted update rule is obtained

$$\begin{aligned} &\bar{\phi}^+ V^+ = \bar{\phi}^- V^- - \Delta t \sum_s \mathcal{F}_\phi^s \\ &\text{with} \quad \mathcal{F}_\phi^s = \int_{\Gamma^s} \boldsymbol{f}_\phi^s \cdot \mathbf{n}^s\, \mathrm{d}a. \end{aligned} \tag{48}$$

Here the surface integral term $\boldsymbol{f}_\phi^s$ in Eq. (45) is substituted by the numerical flux value $\mathcal{F}_\phi^s$ associated with the variable ϕ over the surface s. A special case of $\mathcal{F}_\phi^s$ is the volume flux value $\mathcal{F}^s$ which describes the rate of volume transported from the current to the adjacent elements over the element edge s and is defined to be positive for outflow material transports in the direction of the normal $\mathbf{n}$

$$\mathcal{F}^s = \int_{\Gamma^s} \mathbf{c}^s \cdot \mathbf{n}^s\, \mathrm{d}a. \tag{49}$$

The total (downstream) volume V^+ can then be updated from the upstream volume V^- according to

$$V^+ = V^- - \Delta t \sum_s \mathcal{F}^s. \tag{50}$$

Volume-weighted advection procedures, as given in Eq. (48), ensure the volumetric conservation of the variable ϕ during the advection step, provided that the flux is determined in a conservative manner. A mass-weighted advection procedure can be obtained by applying the following, modified update scheme

$$\bar{\phi}^+ M^+ = \bar{\phi}^- M^- - \Delta t \sum_s \tilde{\mathcal{F}}_\phi^s, \tag{51}$$

with M^- and M^+ being the element masses before and after the advection step, respectively (down- and upstream masses). $\tilde{\mathcal{F}}_\phi^s$ is now a mass-associated numerical flux of the variable ϕ. The mass flux can be computed similar to Eqs. (49) and (50)

$$\begin{aligned} &M^+ = M^- - \Delta t \sum_s \tilde{\mathcal{F}}^s \\ &\text{with} \quad \tilde{\mathcal{F}}^s = \int_{\Gamma^s} \varrho\, \mathbf{c}^s \cdot \mathbf{n}^s\, \mathrm{d}a. \end{aligned} \tag{52}$$

Depending on the type of the advection variable, the volume- and mass-weighted advection schemes can be applied.

It is clear that the above mentioned advection strategy is only first-order accurate in time and is thus limited in the time step size, i.e. since no physical time is associated with the advection step, the convective displacement increment $\Delta t\,\mathbf{c}$ has to be limited by the Courant stability criterion $C_r = \Delta t\,|\mathbf{c}|/h \leq 1$. This limits the size of the advection volumes with respect to the total element size. Furthermore, the distribution of the variable ϕ within the current element is usually non-linear. Essential for the spatial approximation order and accuracy of the advection method is the determination of the numerical flux value $\mathcal{F}^s_\phi$. Here methods of first-order accuracy, where the flux value is assumed to be constant and higher-order methods, where a non-linear distribution of ϕ is reconstructed, are possible. The determination of the numerical flux values will be the main topic of the next sections.

4.4 Determination of the numerical flux values in the finite volume approach

The global approximation properties of advection schemes, based on finite volumes, essentially depend on the determination and approximation of the numerical flux value $\mathcal{F}^s_\phi$ of the variable ϕ over the partial element boundary s. Almost all properties, summarized in Sect. 3.2, are strongly influenced by the flux value. A large number of different schemes has been published, mainly with respect to fluid dynamics applications. In general, these schemes can be separated into the classical linear advection schemes, like e.g. the *upstream difference scheme*, the *Lax-Friedrich scheme*, the *QUICK scheme* or the *Lax-Wendroff* and the *Beam-Warming schemes* and in the so-called high-resolution, non-linear advection schemes, where the flux-corrected transport (FCT) scheme and the total variation diminishing (TVD) scheme are probably the most widely used approaches (see e.g. [66, 16] or [18]).

The classical first- and second-order advection schemes are usually linear schemes in the sense that the solution procedure does not depend on the solution itself and can be given directly in a closed-form. The distribution of ϕ within each element is assumed to be constant (first-order accurate advection schemes) or of higher order (at least second-order accurate advection scheme). Unfortunately, these schemes show a couple of drawbacks that make them unusable in a finite element framework, where the solution variable ϕ highly influences the approximation behavior and the solution quality of the overall analysis. Therefore, high-resolution, non-linear advection schemes promise a better solution quality for the advection problem.

In the remainder of this section, the first-order accurate upstream and the second-order accurate Lax-Wendroff advection scheme, as classical examples for linear schemes, will first be analyzed in more detail. Subsequently, a special class of TVD schemes is presented that will be applied to solve the present advection problem.

4.4.1 Classical first- and second-order flux calculations

Generally, the classical procedures to determine the flux values are based on the approximation of the temporal and spatial derivatives in the finite-volume advection equation Eq. (45) using finite differences. This results in first and second-order accurate advection methods. Representative for these classical approaches, the first-order upstream and the second-order Lax-Wendroff scheme are discussed. These schemes are also used in an ALE framework by different authors (e.g. [9] or [57]).

The first-order accurate *upstream difference scheme*, also known as the *donor-cell algorithm* (see e.g. [56] or [10]), is based on a forward or backward difference approximation for the spatial derivative, depending on the flow direction. The distribution of the fundamental unknown ϕ is assumed to be constant within each element. If an element contains a higher-order distribution of ϕ, the element mean value $\bar{\phi}$ is determined according to Eq. (46), prior to the application of the advection scheme.

A meaningful advection scheme requires that the informations for the finite difference approximation of the spatial gradient is performed by only using informations from the upstream direction of the flow, i.e. the new value $\bar{\phi}^+$ is computed by tracing the characteristics back in the upstream direction, passing through $\bar{\phi}^+$. Therefore, the computation of the gradient depends on the direction of the convective velocity $\mathbf{c}$. This process is also known as *upwinding* (cf. Fig. 8 for a simple description). Using the total volume flux $\mathcal{F}^s$ over the element edge s (with $s = 1, \ldots, n_{(\text{edges})}$), defined in Eq. (49), the numerical flux value $\mathcal{F}^s_\phi$ on the boundary s of element j can then be written as

$$\mathcal{F}^s_\phi = \frac{1}{2}\,\mathcal{F}^s\left(\bar{\phi} + \bar{\phi}^s\right) + \frac{1}{2}\,|\mathcal{F}^s|\left(\bar{\phi} - \bar{\phi}^s\right). \tag{53}$$

Here $\bar{\phi}$ is the averaged value of ϕ in the current element, while $\bar{\phi}^s$ is the averaged value in the adjacent element over the element edge s. The method is stable if the Courant criterion is fulfilled, i.e. $C_r = \Delta t\,|\mathbf{c}|/h \leq 1$. Furthermore, the scheme is first-order accurate in space and time, conservative and monotone. Unfortunately, the problem with all first-order linear advection schemes, based on finite differencing, is that they are highly numerical dissipative, i.e. the numerical diffusion leads to a strong flattening and widening of the distribution of ϕ, especially in regions with steep gradients (see Fig. 9). This effect gets worse, if the Courant

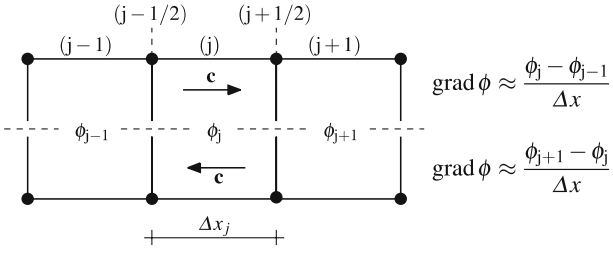

Fig. 8 Concept of *upwinding*; the gradient can only be computed using informations from the upstream direction of the flow

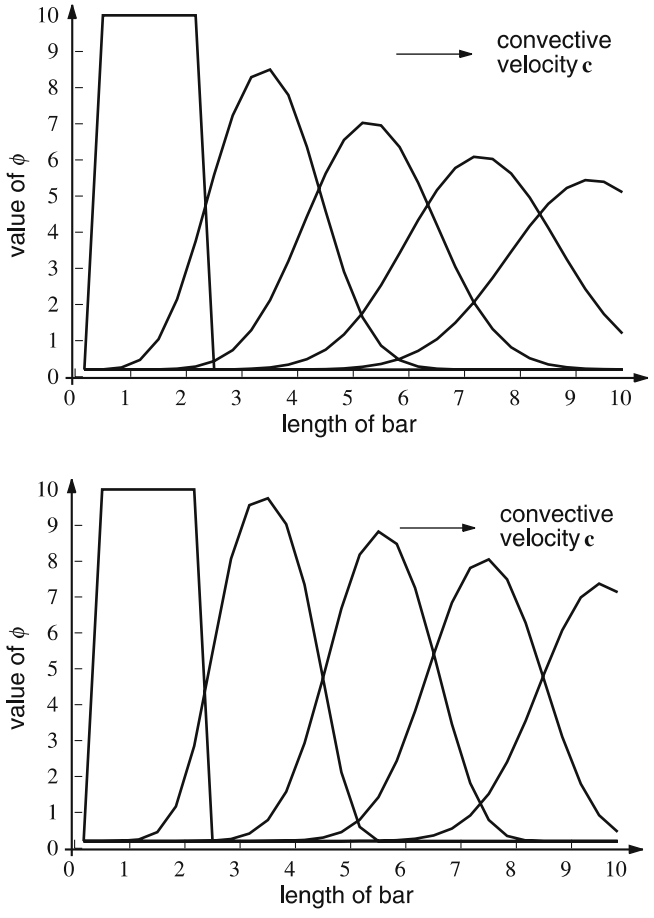

Fig. 9 Solution of the advection problem using the first-order accurate donor advection method *top*: $C_r = 1/3$ and 100 advection steps, resp. *bottom*: $C_r = 7/10$ and 43 advection steps (mesh density: 30 elements in x-direction)

number is reduced and the number of advection steps, needed for the transport problem, is increased. Nevertheless, due to its simplicity and efficient implementation possibilities, the first-order donor-cell or upwind method is used in different ALE codes (see e.g. [57] or [49]). In the case that only one advection step is needed for the transport of the solution variables, the dissipative effects of the method are very small and a sufficient accurate solution can be obtained in most cases. However if the material deformation is very localized or if an implicit time integration with large time steps is applied, several advection steps may be required in the remap step and, due to a degeneration of the internal variables, the numerical dissipation can lead to large inconsistencies in the numerical algorithm.

The second class of classical advection schemes, is based on a second-order accurate approximation of the derivatives in the advection equation, where the most used scheme is probably the *Lax-Wendroff* approach (see e.g. [40]). The key point of the Lax-Wendroff method is to replace the time derivatives with spatial derivatives, using the advection equation ($\dot{\phi}|_{\chi} = -\operatorname{grad}\phi \cdot \mathbf{c}$). Therefore, first a Taylor series expansion of ϕ in time is performed, where terms of third- and higher order are neglected

$$\phi^{+} = \phi^{-} + \frac{\partial \phi^{-}}{\partial t}\,\Delta t + \frac{1}{2}\,\frac{\partial^2 \phi^{-}}{\partial t^2}\,\Delta t^2 + \mathcal{O}\big(\Delta t^3\big). \tag{54}$$

Inserting the advection equation recursively, the update equation of the Lax-Wendroff scheme is obtained as follows

$$\phi^{+} = \phi^{-} - \Delta t\ \operatorname{grad}\phi^{-} \cdot \mathbf{c} + \frac{1}{2}\Delta t^2\, \mathbf{c} \cdot \operatorname{grad}(\operatorname{grad}\phi^{-}) \cdot \mathbf{c}. \tag{55}$$

In a finite difference framework, the spatial derivatives are usually approximated using a first-order forward-difference and a second-order central difference scheme. The flux term in Eq. (48) can then be represented as

$$\mathcal{F}^{s}_{\phi} = \frac{1}{2}\,\mathcal{F}^{s}\left(\bar{\phi} + \bar{\phi}^{s}\right) + \frac{\Delta t}{2\,h}\,\mathcal{F}^{s^2}\left(\bar{\phi} - \bar{\phi}^{s}\right), \tag{56}$$

where again, $\bar{\phi}^{s}$ is the volume averaged value of ϕ in the adjacent element over element edge s and h denotes a characteristic element length. In Fig. 10 the solutions of the 2D example of the propagating square wave are depicted. As

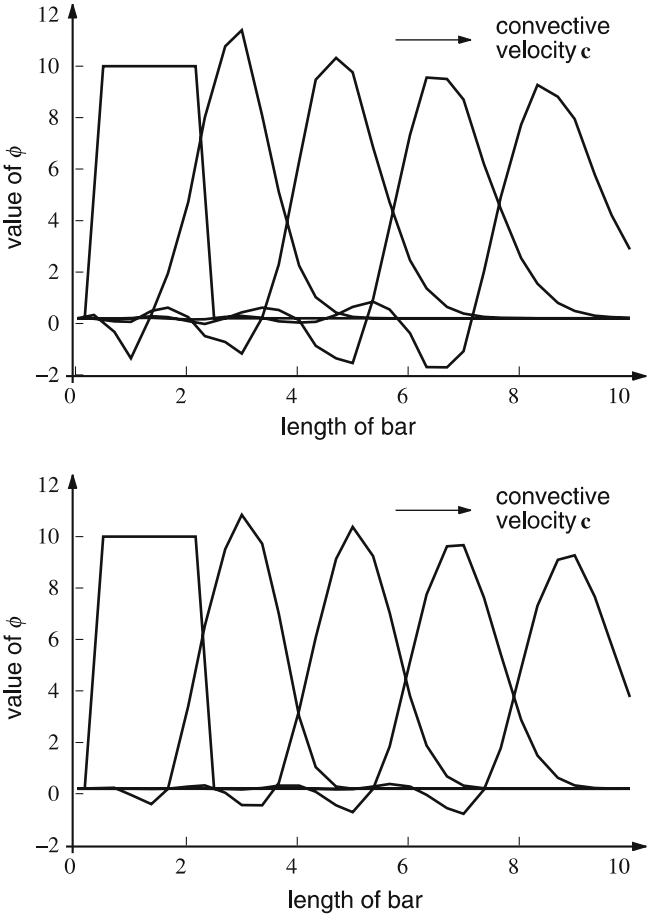

Fig. 10 Solution of the advection problem using the second-order accurate Lax-Wendroff advection method *top*: $C_r = 1/3$ and 100 advection steps, resp. *bottom*: $C_r = 7/10$ and 43 advection steps (mesh density: 30 elements in x-direction)

expected, the numerical diffusion is smaller, compared to the first-order upstream advection scheme. Indeed, the shape of the initial square wave is not retained accurately, rather it is broadened at the bottom and sharpened at the top of the wave. It can be shown that the method is neither monotone nor conservative. Especially the absence of monotonism, characterized by the typical unphysical oscillations of a linear, second-order advection scheme, violates the permitted range of the solution variable ϕ deeply and the application of the Lax-Wendroff advection scheme within an ALE finite element approach can cause serious problems.

In the finite element framework of ALE methods, a Galerkin-type approach for the approximation of the higher-order spatial derivatives, required for the solution of Eq. (55), is sometimes applied (see e.g. [8] or [56]). This approach is based on a least-squares approximation for the first-order gradient $\boldsymbol{\gamma} = \text{grad}\ \phi^-$ at the mesh nodes $\boldsymbol{\gamma}_\text{I}$ using the divergence theorem

$$\int_\Omega N_\text{I}^\gamma\, \boldsymbol{\gamma}\, \mathrm{d}v = -\int_\Omega \phi\ \text{grad}\ N_\text{I}^\gamma\, \mathrm{d}v + \int_{\partial\Omega} N_\text{I}^\gamma\, \phi\, \mathbf{n}\, \mathrm{d}a, \qquad (57)$$

where $\mathbf{n}$ is the outward normal on the boundary of the domain Ω in the current configuration and N_I^γ is a set of shape functions. After insertion of the approximation $\boldsymbol{\gamma} \approx \sum_\text{I} N_\text{I}^\gamma\, \boldsymbol{\gamma}_\text{I}$ and assemblage, the following linear system is obtained $\boldsymbol{V}^\gamma\, \boldsymbol{\gamma} = \boldsymbol{\Phi}$ with

$$\boldsymbol{\Phi} = [\Phi_\text{I}] = -\int_{\Omega_e} \phi\ \text{grad}\ N_\text{I}^\gamma\, \mathrm{d}v + \int_{\partial\Omega_e} N_\text{I}^\gamma\, \phi\, \mathbf{n}\, \mathrm{d}a. \qquad (58)$$

Again, $\boldsymbol{V}^\gamma$ is a consistent volume matrix that can be diagonalized by a lumping procedure to obtain an explicit approach. Subsequently, the second derivative of ϕ can be computed in the element center using the shape functions N_I^γ and the following expression is obtained for the update of ϕ

$$\phi^+ = \phi^- - \Delta t\, \mathbf{c}\cdot\boldsymbol{\gamma} + \frac{1}{2}\Delta t^2\, \mathbf{c}\cdot\text{grad}\ \boldsymbol{\gamma}\cdot\mathbf{c}. \qquad (59)$$

The update scheme can easily be applied to higher-order elements, where more than one integration point is present, by applying Eq. (59) Gauss point-wise for all internal variables. Further information and a comparison to a two-dimensional extension of the first-order upwind scheme are given in [56].

The general problem of almost all linear advection methods is that they are either highly numerical dissipative, like the first-order advection schemes, or that they are disturbed by large, unphysical oscillations, like the higher-order advection approaches. Both numerical effects influence the evolution of the solution while the analysis proceeds. Since the accuracy and the stability of the underlying finite element approach highly depends on the accuracy of the advection approach other, more reliable methods have to be taken into account. A characteristic statement, concerning this phenomenon, is given by Loehner ([44])

> *"For these linear schemes, the choice is between high-order, oscillatory and 'noisy' solutions or low-order, overdiffusive and 'smooth' solutions."*

4.4.2 Higher-order, non-linear flux calculations

Based on the idea to construct higher-order advection schemes that fulfill the monotonicity and conservation requirements simultaneously, different higher-order, non-linear advection schemes, based on finite difference or finite-volume methods were developed in the past. Among these methods are for instance essential non-oscillatory schemes (ENO), FCT schemes and TVD schemes, where the two latter ones are probably the most popular approaches.

The basic idea of the FCT techniques is first to apply a spatially higher-order scheme, like e.g. the Lax-Wendroff scheme, as far as possible. If large gradients or discontinuities in the solution distribution occur, artificial diffusion is added to eliminate the production of oscillations and to smooth the spatial distribution of the solution variable. This adaptive dissipation property is the challenging point of these high-resolution schemes and has to be implemented carefully to ensure that enough dissipation is introduced to preserve the monotonicity without affecting the final solution. This is realized through the concept of *flux-limiters* (see e.g. [16]). For a finite-volume-like approach, this process can for instance be written as

$$\phi^+ V^+ = \underbrace{\phi^- V^- - \Delta t \sum_s \mathcal{F}_\phi^{s,h}}_{\text{second-orderadvection}} + \underbrace{\Delta t \sum_s \lim\left(\mathcal{F}_\phi^{s,h} - \mathcal{F}_\phi^{s,l}\right)}_{\text{limitedcorrection}}, \qquad (60)$$

where $\mathcal{F}_\phi^{s,l}$ denotes the lower-order and $\mathcal{F}_\phi^{s,h}$ the higher-order flux term, whose difference is restricted by the limiter to avoid the oscillatory over- and undershots. Obviously, FCT schemes are second-order accurate in smooth regions and reduce to almost first-order accuracy in the vicinity of steep gradients. Since the limitation operation itself depends on the solution variable ϕ and thus the diffusion coefficient depends on the local behavior of the solution, such procedures are basically non-linear.

The TVD schemes are constructed in a similar way, where again second-order approaches are applied in smooth regions that reduce to only first-order accuracy in regions with steep gradients. In contrast to the FCT approaches, only element averaged values $\bar{\phi}$ are considered to ensure the conservation properties of the scheme. To obtain a second-order approach, the distribution of ϕ is reconstructed, based on gradients, computed from informations of the adjacent elements, such that no spurious oscillations near a discontinuity occur. Again this is obtained by the limiter approach. A characteristic property of these schemes is the limitation of the so-called total variation, introduced by [30].

A comparison of the numerical solution provided by both algorithms shows that, depending on the choice of the higher-order advection scheme, the FCT approach does not necessarily conserve the solution variable during the advection step. Furthermore, if the artificial diffusion to be added is

overestimated, FCT schemes can still show high numerical diffusion, while this effect can mostly be eliminated for the TVD schemes, depending on the choice of the limiter. Practical implementations and comparisons are given in e.g. [23], [66] or [64]. The remainder of this section will be restricted on a detailed description of a special class of TVD schemes, based on finite volume techniques, that serves as a direct higher-order extension of the first-order upstream approach.

Basic concept of the TVD advection scheme The basic concept of the TVD advection schemes was derived in [30], where two basic requirements for this kind of advection scheme were formulated

1. no additional oscillations shall occur during the advection approach and
2. existing oscillations are not allowed to increase.

Formally, these requirements can be described by a non-oscillatory property, where the total variation of the general variable ϕ in the domain Ω, defined by

$$TV[\phi] = \int_{\Omega} |\operatorname{grad} \phi| \, \mathrm{d}v \leq C < \infty \tag{61}$$

is bounded and does not increase with time. In a one-dimensional, discrete sense, this means that the total variation of the advected element variable $\bar{\phi}^+$, denoted by $\mathrm{TV}^h[\bar{\phi}^+]$, is not larger than the total variation of the original element variable $\bar{\phi}^-$, denoted by $\mathrm{TV}^h[\bar{\phi}^-]$

$$\begin{aligned} \mathrm{TV}^h[\bar{\phi}^+] &:= \sum_{i=0}^{N-1} |\bar{\phi}_{i+1}^+ - \bar{\phi}_{\mathrm{i}}^+| \\ &\leq \sum_{i=0}^{N-1} |\bar{\phi}_{i+1}^- - \bar{\phi}_i^-| =: \mathrm{TV}^h[\bar{\phi}^-]. \end{aligned} \tag{62}$$

N is the number of nodes and TV^h is a discrete, finite difference-like approximation of the total variation, while $\bar{\phi}$ describes the element-averaged quantity of ϕ [cf. Eq. (46)]. The total variation limits the differences of $\bar{\phi}$ in two adjacent elements, prevents the development of over- and undershots, i.e. the development of new local extrema, and results therefore in a monotonic, non-oscillatory scheme. Thus, if oscillations occur, they are truncated using the limiter concept. In the past, several different TVD approaches have been published (see e.g. [18, 30] or [60]). The scheme that will be applied here is a direct, second-order accurate extension to the first-order upstream technique, described in the last section, where the TVD numerical flux value is computed according to

$$\mathcal{F}_{\phi}^{s} = \frac{1}{2} \mathcal{F}^{s} \left(\hat{\phi} + \hat{\phi}^{s}\right) + \frac{1}{2} |\mathcal{F}^{s}| \left(\hat{\phi} - \hat{\phi}^{s}\right). \tag{63}$$

In contrast to the first-order method, a piecewise linear reconstruction $\hat{\phi}$ of the volume-averaged quantity $\bar{\phi}$ in each local direction of the element is assumed, based on informations from the adjacent elements. In Eq. (63), $\hat{\phi}$ is the reconstruction near the boundary s of the current element, while $\hat{\phi}^s$ denotes the reconstruction over the boundary s of the adjacent element (cf. Fig. 11). If the linear reconstruction of $\hat{\phi}$ is performed around the centroid of the current element i, the conservation requirement of the advection scheme is fulfilled a priori. For the local element direction ξ we obtain

$$\hat{\phi}_i^{\xi}(\xi, t) = \bar{\phi}_i(t) + s_i^{\xi}(t) \, (\xi - \xi_i), \tag{64}$$

where ξ_i is the centroid coordinate of the current element i and s_i^{ξ} is the slope in the local ξ-direction that has to be determined in accordance with the TVD condition. In the multidimensional case and assuming a structured mesh geometry, the advection can be performed in so-called directional sweeps. Here the reconstruction is determined for all local directions of an element and ξ corresponds to the coordinate of the local element coordinate system that is aligned with the direction of the current advection sweep. The values $\hat{\phi}$ and $\hat{\phi}^s$ at the element edge s in Fig. 11, required for the evaluation of Eq. (63), are subsequently computed according to

$$\hat{\phi} = \bar{\phi}_i - \frac{1}{2} l_i^{\xi} \, s_i^{\xi} \quad \text{and} \quad \hat{\phi}^s = \bar{\phi}_{i-1} + \frac{1}{2} l_{i-1}^{\xi} \, s_{i-1}^{\xi}, \tag{65}$$

respectively.

The computation of the numerical flux values over the edges s of the current element i requires the determination of the slopes in the current element and also in the first-order adjacent elements, i.e. the elements sharing an edge with element i. Therefore, the distribution of ϕ in the first- and second-order adjacent elements is required. In the vicinity of a boundary, this information is certainly not available and the advection process reduces to a first-order Donor advection scheme, where the slope vanishes ($s_i = 0$). In the practical implementation of the advection scheme, it is advantageous, only to compute the outflow fluxes of the current element to limit the support of the local flux calculation. In this case, only the slope s_i in the current element is required and the determination of the flux values is simplified considerably.

The concept of slope limiters The slope for the reconstruction of $\bar{\phi}$ in the current element is computed using informations from the adjacent elements. To account for the monotonicity requirement, given by the TVD condition in Eq. (62), the slope has to be limited, such that over- and undershots in the

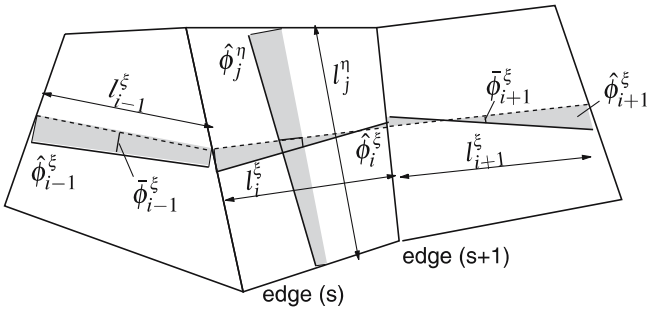

Fig. 11 Schematic representation and naming conventions for the linear reconstruction process of $\bar{\phi}$ for the "donor" element i in the local ξ-direction

reconstructed distribution of $\bar{\phi}$ are widely avoided. This can be achieved by a comparison of the maximum difference of adjacent element values $\bar{\phi}$, which is generalized by the concept of slope limiters. Here, the slope s_i^ξ of ϕ in the current element i and in the local element direction ξ is computed using the element-averaged quantities $\bar{\phi}$ as follows

$$s_i^\xi = \frac{\mathcal{L}_i}{l_i^\xi}\,(\bar{\phi}_{i+1} - \bar{\phi}_i), \tag{66}$$

where l_i^ξ is the length of element i in the local ξ-direction, i.e. the distance of the center nodes of opposite element edges, while the slope limiter $\mathcal{L}_i$ is defined as a function of the ratio of consecutive gradients

$$\mathcal{L}_i = \mathcal{L}(\theta_i) \qquad \text{with} \qquad \theta_i = \frac{\bar{\phi}_i - \bar{\phi}_{i-1}}{\bar{\phi}_{i+1} - \bar{\phi}_i}. \tag{67}$$

$\bar{\phi}_{i-1}$, $\bar{\phi}_i$ and $\bar{\phi}_{i+1}$ are the average values of the current and the first-order adjacent elements in the considered advection direction. For reasons of stability, the limiter function $\mathcal{L}(\theta_i)$ is required to fulfill the TVD condition which finally leads to the restriction $0 \le \mathcal{L}(\theta_i) \le 2$. However, the choice of the limiter $\mathcal{L}_i(\theta)$ is not unique and several different limiters are possible.

A first limiter, for instance, leads to the smallest slope, connecting the center point with the adjacent element variable (see Fig. 12a). This *Superbee-Limiter* can be formalized as

$$\begin{aligned} &\mathcal{L}^{\mathrm{SB}}(\theta) := \mathrm{MAX}\big(0, \mathrm{MIN}(1, 2\,\theta), \mathrm{MIN}(\theta, 2)\big) \\ &\text{with} \quad 0 \le \mathcal{L}^{\mathrm{SB}} \le 2. \end{aligned} \tag{68}$$

The limiter was introduced by [48] and also used by [21] for their advection schemes based on discontinuous Galerkin approaches. The min-functions choose the minimum value of the two possible slopes, while the leading 0 ensures that in case of a local extremum of $\bar{\phi}$, i.e. if the gradients are of different signs, a zero slope value is achieved. However, in practical advection problems, this limiter can lead to advection slopes that are too steep and oscillations can still occur in the vicinity of the element, depending on the local Courant number. A more diffusive limiter can be given in terms of the *MinMod-Limiter*, depicted in Fig. 12b. The MinMod limiter was introduced by van Leer [41] in the framework of his MUSCL schemes (monotone upwind schemes for conservation laws)

$$\begin{aligned} &\mathcal{L}^{\mathrm{MM}}(\theta) := \mathrm{MAX}\big(0, \mathrm{MIN}(1, \theta)\big) \\ &\text{with} \quad 0 \le \mathcal{L}^{\mathrm{MM}} \le 1. \end{aligned} \tag{69}$$

[10] and [49] applied this slope in their MMALE codes, while the first author also extended the choice of the slopes by adding a second-order polynomial fit through three adjacent element values. The MinMod limiter leads to advection slopes that are approximately half of he slopes, generated by the Superbee limiter. Since the maximum values cannot be reconstructed by the MinMod limiter, in contrast to the Superbee limiter, it shows a very diffusive behavior. A limiter that leads

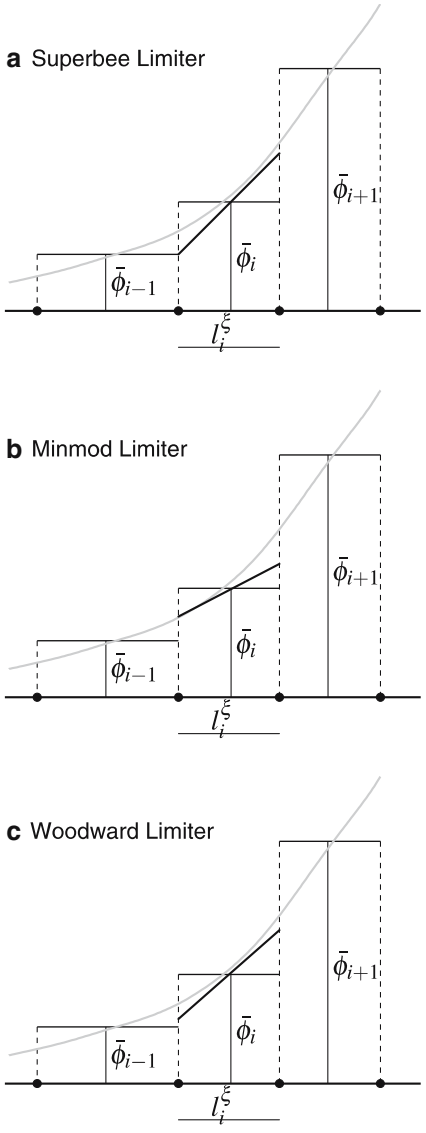

Fig. 12 Schematic representation of three example limiters. The emphasized line is the linear reconstruction of the distribution of ϕ

to an advection slope between the above mentioned ones is the *Woodward-Limiter*, depicted in Fig. 12c

$$\begin{aligned} &\mathcal{L}^{\mathrm{WW}}(\theta) := \mathrm{MAX}\left(0, \mathrm{MIN}\left(2, 2\,\theta, \frac{1}{2}\,(1+\theta)\right)\right) \\ &\text{with} \quad 0 \le \mathcal{L}^{\mathrm{WW}} \le 2. \end{aligned} \tag{70}$$

Generally, the Superbee limiter defines an upper bound of all possible limiters that are able to suppress the unphysical oscillations, while the MinMod and the Woodward limiter lead to less restrictive slopes. The choice of the limiter considerably influences the determination of the numerical flux values, i.e. the amount of the variable transported in the downstream direction and thus influences the final distribution of the advected value $\bar{\phi}^+$. If the slope limiter is chosen too large, oscillations will still occur, while in case of a slope limiter

that is too small, the advection will result in a dissipative solution distribution.

The choice of the correct limiter can be made in dependence of the advection volume $\mathcal{F}^s$ resp. the local Courant number. If the advection volumes are relatively large, emerging from high Courant numbers ($C_r \geq 1/2$), large limiter values lead to an overestimation of the advective flux $\mathcal{F}^s_\phi$ and thus over- and undershots can occur in the downstream solution. In this case, a more restrictive limiter has to be chosen for the determination of the advection fluxes. This can for instance be formalized on the basis of the MinMod limiter. To account for the advection behavior at different Courant numbers, a scaling factor α is introduced that scales the slope, used for the advection process. Figure 13 shows the distribution of the optimal scaling factor α for different Courant numbers. $\alpha = 1$ corresponds to the diffusive MinMod limiter, while $\alpha = 2$ corresponds to an approximation of the less-diffusive Superbee limiter that is applied in the case of small advection fluxes. Until a Courant number of $C_r = 1/2$ is reached, this limiter leads to satisfying results. If C_r exceeds this value, the scaling factor has to be reduced non-linearly. To establish the curve shown in Fig. 13, the pseudo two dimensional example was used, where a homogeneous distribution of the convective velocity and equidistant grid nodes was assumed. In this case, the Courant number can be computed exactly using Eq. (34). However, in practical advection problems, usually a distorted mesh and a non-homogeneous distribution of the convective velocity emerges. Thus the Courant number cannot be computed exactly and a rough, second-order approximation of the curve for values $C_r > 1/2$ will be sufficient, i.e.

$$\alpha(C_r) = \begin{cases} 2 & \text{for } C_r \leq 1/2 \\ 5.75\, C_r^2 - 12.6\, C_r + 6.9 & \text{for } C_r > 1/2 \end{cases}. \quad (71)$$

The check is performed element-wise to determine the advection limiter during the advection process. Subsequently, the advection fluxes are determined by evaluating the MinMod limiter Eq. (69) and using the modified slope

$$s_i^\xi = \frac{\alpha(C_r)\, \mathcal{L}^{\mathrm{MM}}(\theta_i)}{l_i^\xi} (\bar{\phi}_{i+1} - \bar{\phi}_i), \quad (72)$$

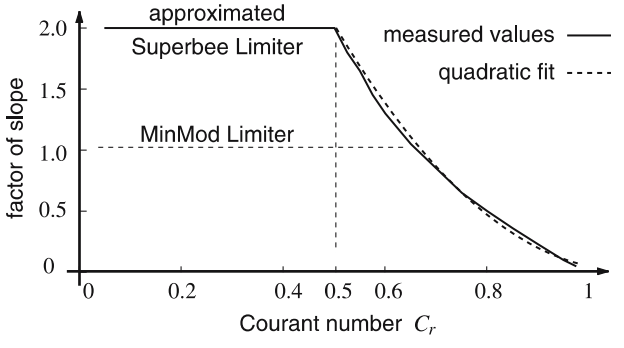

Fig. 13 Distribution of the optimal factor α for the TVD slope calculation for increasing Courant numbers

where the scaling factor α now ensures the monotonicity of the solution and the limitation of the numerical diffusion.

Redistribution to the integration points By construction, the TVD advection scheme is designed for the transport of element-averaged values of ϕ and thus $\bar{\phi}$ is piecewise constant within each element. In a multidimensional finite element simulation, multiple integration points are usually used within one element and the distribution of ϕ becomes non-constant. The assumption of a constant distribution leads to inaccurate results of the advected quantities and a linear redistribution of $\bar{\phi}$ within each element is performed to improve the quality of the advection process. This redistribution can be based on the TVD-limited slopes defined in Eq. (72). However, due to the new element geometries and distributions of ϕ after the advection step, the slopes s_i have to be recalculated for each element, e.g. using a linear interpolation according to

$$\phi_i^+(\xi) = \bar{\phi}_i^+ + \boldsymbol{s}_i \cdot \left(\boldsymbol{\xi} - \boldsymbol{\xi}_i\right). \quad (73)$$

$\boldsymbol{s}_i = (s_i^\xi, s_i^\eta, s_i^\zeta)^{\mathrm{T}}$ is the vector of the reconstructed slopes of $\bar{\phi}$ in the three local element directions $\boldsymbol{\xi} = (\xi, \eta, \zeta)^{\mathrm{T}}$. The determination of the redistribution slopes is performed with respect to a local element coordinate system (see Fig. 14) that is usually not aligned with the global Cartesian coordinate system $\mathbf{x}$. Therefore, the coordinate differences $(\xi - \xi_i)$, $(\eta - \eta_i)$ and $(\zeta - \zeta_i)$ in Eq. (73) have to be computed with respect to this element coordinate system. Considering the length of the element axes l_i^ξ, l_i^η and l_i^ζ the differences can be sufficiently approximated by

$$(\xi - \xi_i) \approx \frac{1}{2}\, \xi_g\, l_i^\xi, \quad (\eta - \eta_i) \approx \frac{1}{2}\, \eta_g\, l_i^\eta \quad \text{and} \quad (\zeta - \zeta_i) \approx \frac{1}{2}\, \zeta_g\, l_i^\zeta, \quad (74)$$

where $\boldsymbol{\xi}_g = (\xi_g, \eta_g, \zeta_g)^{\mathrm{T}}$ are the local coordinates of the evaluation point g and are formally identical with the integration points.

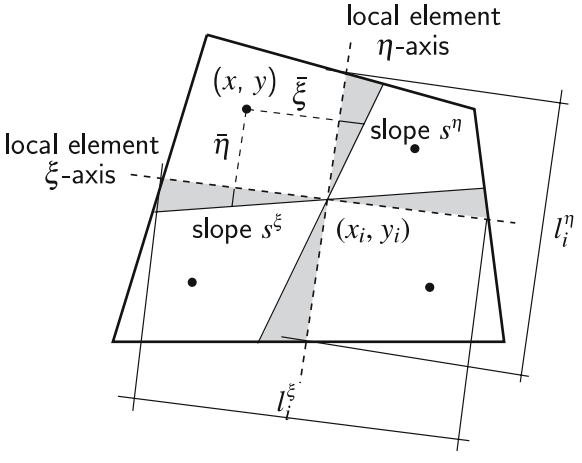

Fig. 14 Redistribution of the bi-linear shape of ϕ using limited slopes s^ξ and s^η in two dimensions

4.5 Global advection algorithm

The global advection algorithm for the second-order advection of the element-based quantity ϕ using the TVD advection scheme is summarized in Alg. (4.1). Clearly the advection process, based on finite volume methods requires extensive knowledge about the element neighborhoods, especially for the determination of the advection volumes between adjacent elements over a specific edge s. These informations have to be constructed from the global mesh topology, which requires a relatively high numerical effort. Since the element topology remains constant throughout the analysis, the element neighborhoods need only to be established once and can be stored in the global data base.

Algorithm 4.1 Schematic global TVD advection algorithm for the quantity ϕ

Requires: upstream geometry $\mathbf{x}^-$ and variable to be advected ϕ^-; convective displacement increment $\mathbf{u_c} = \Delta t\, \mathbf{c}$; element connectivity list

Provides: advected, downstream quantity ϕ^+

1. setup neighbor informations of adjacent elements from element connectivity list (only first time)
2. compute and store element averaged quantities $\bar{\phi}^- = \frac{1}{V} \int_\Omega \phi^-\, \mathrm{d}v$
3. loop all elements with prescribed convective velocity $\mathbf{c} \neq \mathbf{0}$ at the vertices
   (a) determine adjacent elements, compute element lengths/volumes and localize the advection data for the current sweep direction
   (b) loop element edges
   - compute advection volume flux $\left(\Delta t\, \mathcal{F}^s\right)$ due to Eq. (49); cycle inflow volume fluxes
   - update total element volume flux $\rightarrow\ \Delta t \sum_s \mathcal{F}^s$; subtract from current, add to adjacent element
   - reconstruct distribution of $\bar{\phi}$ and determine TVD advection fluxes for each quantity $\bar{\phi}$
   - update total element variable flux $\rightarrow\ \Delta t \sum_s \mathcal{F}^s_\phi$; subtract from current, add to adjacent element
4. second loop over all elements to perform global variable update
   (a) compute upstream volumes V^- and update downstream volumes $V^+ = V^- - \Delta t \sum_s \mathcal{F}^s$
   (b) update downstream quantities $\bar{\phi}^+$ using the transport volumes $\bar{\phi}^+ V^+ = \bar{\phi}^- V^- - \Delta t \sum_s \mathcal{F}^s_\phi$
5. update global variable arrays and redistribute average quantities $\bar{\phi}$ to the integration points

The solution of the advection problem for the pseudo 2D system is given in Fig. 15 for different Courant numbers ranging from $C_r = 1/5$ to $C_r \approx 1$. Clearly, if the Courant number takes the value $C_r = 1.0$, the shape is retained exactly on the uniform mesh. For the whole range of Courant numbers $C_r < 1$, the initial shape of the square wave is reproduced rather accurately using the dynamic limiting as described above. Indeed, a slight flattening of the square, due to the changing distribution of evaluation points, i.e. integration points, with respect to the position of the wave, cannot fully be prevented.

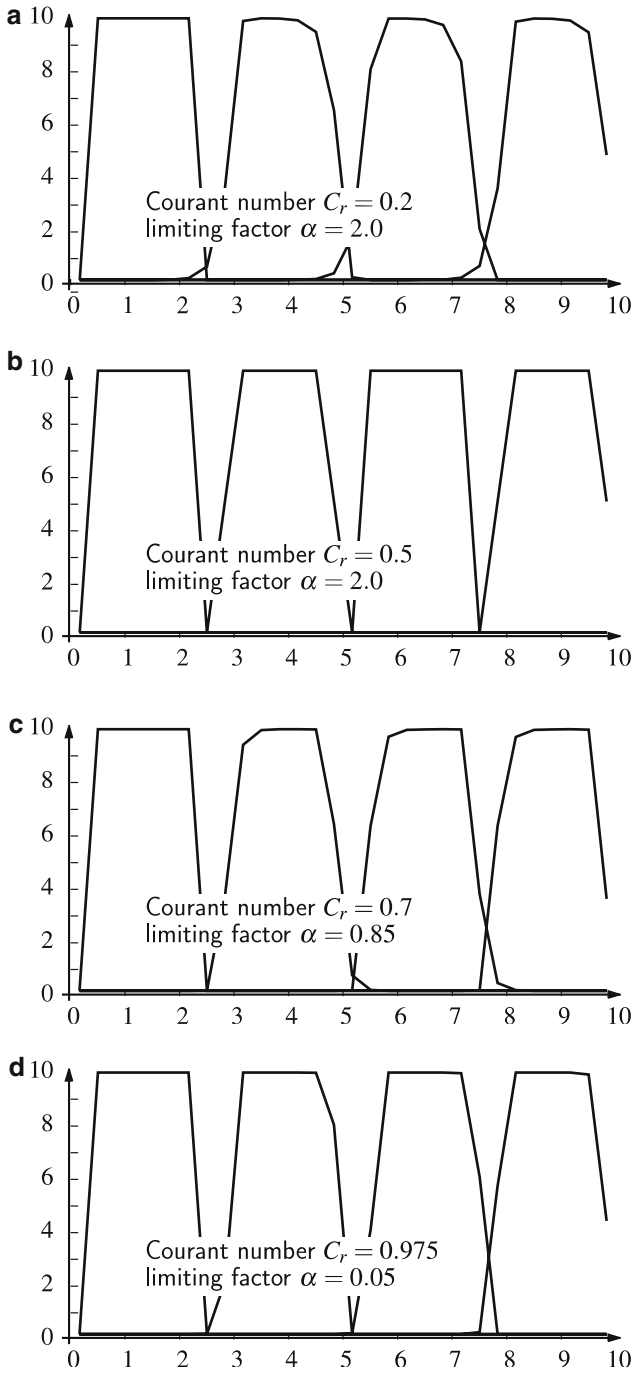

Fig. 15 Solution of the advection problem using the second-order Total variation diminishing TVD scheme and Courant numbers ranging from $C_r = 1/5$ to $C_r \approx 1$ (mesh density: 30 elements in x-direction)

4.6 Generalization of the advection scheme to the multidimensional case

In case of a multidimensional advection problem, material is transported arbitrarily through the finite element mesh, according to the direction of the convective velocity, prescribed at the mesh nodes. Essential for the advection of the

element variables is the accurate determination of the advection volumes that specify "the amount of the variable" to be transported to the downstream element. Furthermore, the multidimensional advection volumes have to be determined accurately to maintain a coherent distribution of the variable ϕ. Here generally two strategies are conceivable that should be discussed in the following.

The numerical, multi-dimensional advection simulations are performed for a circular wave propagating with the convective velocity **c** in the diagonal direction of a square region (see Fig. 16). Physically, the gradient at the boundary of the wave is infinite and reduces to a finite gradient for the discrete case, where the wave informations are only given at the 2×2 integration points of each finite element. As in the pseudo-2D examples of the last section, the convective velocity is chosen to be constant and only the Courant number is varied in terms of different time step sizes. The computational domain is discretized using 30×30 equal-sized finite elements, where first, a homogeneous mesh is considered and additionally, the advection behavior on a distorted mesh is examined.

Isotropic advection methods The first strategy is based on an isotropic advection approach, where Eqs. (48) and (51), for volume-specific and mass-specific advection variables, respectively, are evaluated simultaneously for all element edges and the volume fluxes $\Delta t\, \mathcal{F}^s$ $(s = 1, \ldots, n_f)$ in resp.

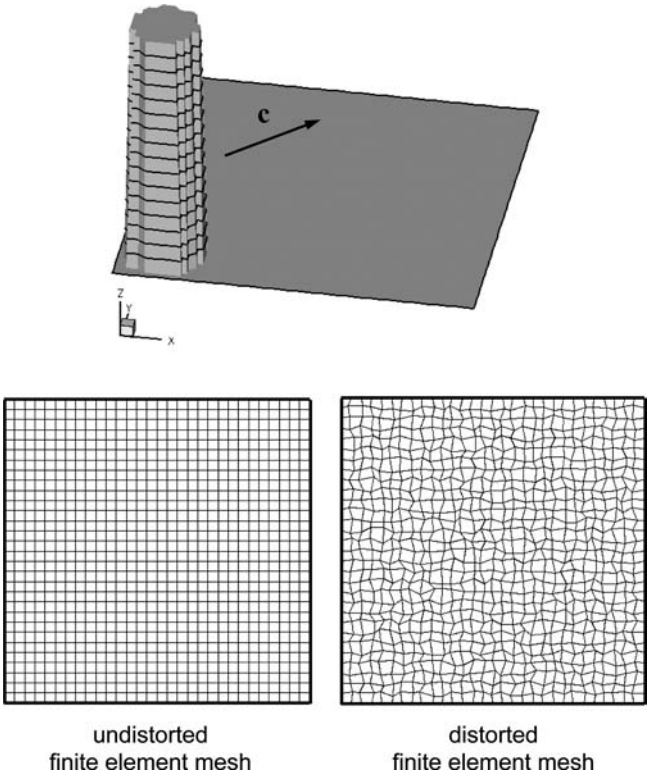

Fig. 16 Two dimensional advection problem: a circular wave traveling in the diagonal direction of a structured, undistorted and distorted finite element mesh

out of the current element over all n_f element faces are computed in one single step (cf. Fig. 17).

Indeed, the problem with this advection approach is that the flux over diagonal element connections, i.e. elements that share only one node, is not accounted for directly and the advection process is primarily processed into the direction of the orientation of the structured mesh. This leads to a strong dispersion of the solution, where the discontinuity mainly expands in the direction perpendicular to the advection direction (crosswind diffusion). Another problem occurs especially in the case of large Courant numbers ($C_r > 0.5$), where the advection volumes can overlap (cf. Fig. 17). In this case, the total volumes, advected from the donor element to the adjacent elements, are overestimated and lead to a further dispersion of the solution. Moreover, the local conservation properties are not fulfilled any more. For these reasons, the isotropic advection approach is found to be only a first-order, multidimensional extension of the one-dimensional advection scheme. In Fig. 18, the evolution of the circular discontinuity during an incompressible advection process and using the second-order TVD advection approach is depicted. The Courant number is chosen to be relatively small ($C_r = 0.3$) to minimize the effect of overlapping advection volumes. Although the peak value of the discontinuity is maintained and no diffusion in the advection direction occurs, the effect of the crosswind diffusion can obviously be observed. Note that the quality of the solutions during the advection process is very similar on the homogeneous and the distorted mesh, since the above mentioned effects occur likewise on both meshes.

One-dimensional advection sweeps The second strategy is based on a spatial operator split technique that can advantageously be applied in the case of structured meshes. In this case, one-dimensional, alternating advection sweeps are performed ([55]), where in each advection step, the propagation of the wave into the direction of the convective velocity **c** is separated into one-dimensional sweeps, each aligned to the axes of the global Cartesian coordinate system (cf. Fig. 19). The material flux between diagonally connected elements is therefore considered indirectly, using a redirection of the flux through an intermediate element (cf. Fig. 20).

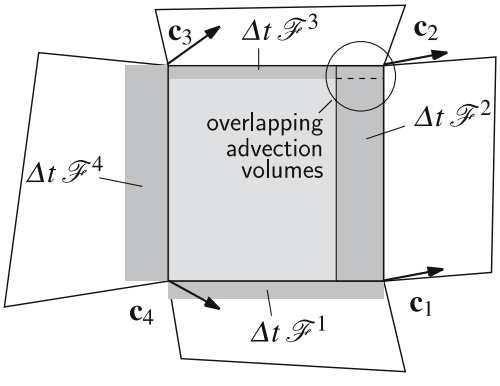

Fig. 17 Illustration of the isotropic, multidimensional generalization for the one-dimensional advection procedure

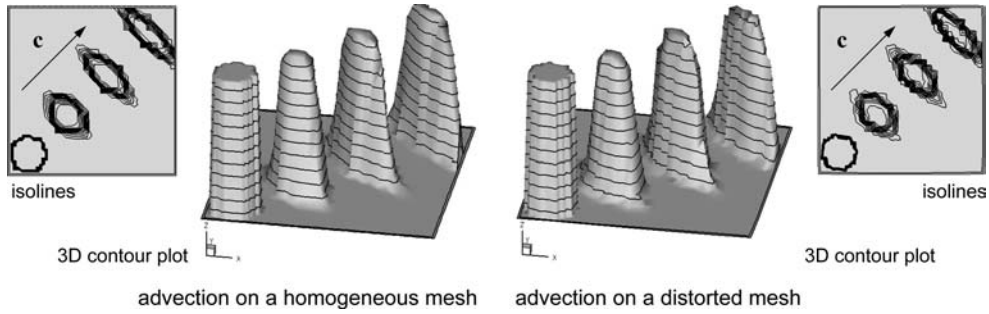

Fig. 18 Two-dimensional TVD advection process of a circular wave using the isotropic approach on a (*left*) homogeneous mesh and a (*right*) distorted mesh with 30 × 30 elements and a convective velocity **c** at $C_r \approx 0.3$. Depicted are the isolines and a 3D contour plot

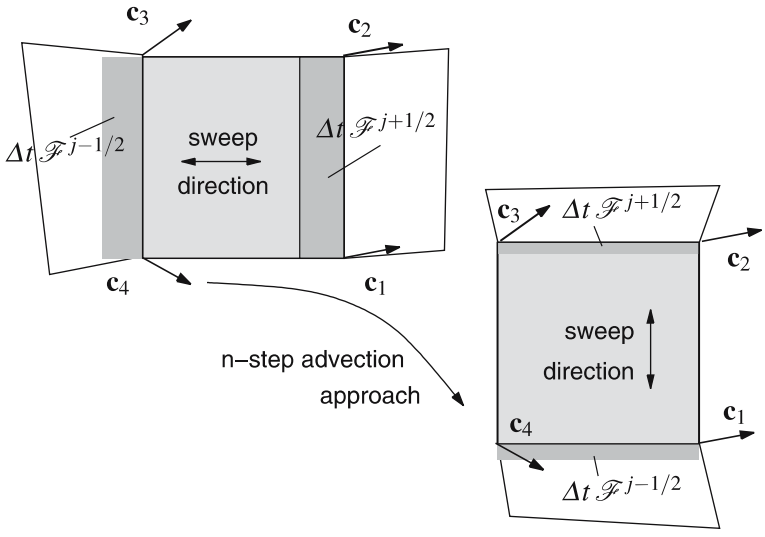

Fig. 19 Illustration of the multidimensional generalization for the one-dimensional advection procedure using one-dimensional advection sweeps

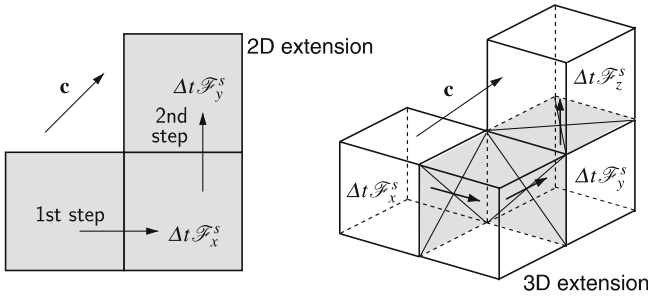

Fig. 20 Concept of one-dimensional advection sweeps; the total, multidimensional volume flux is separated into 2/3 flux-steps, aligned with the global coordinate axes

This approach provides a straight-forward construction of higher-order spatially accurate advection methods with multiple sweeps in each spatial direction and accurately advects the variables over diagonal connected elements. Indeed, numerical experiments show that the extension obtained by considering only one sweep per direction leads to considerably improved results, compared to the isotropic advection approach. To eliminate the directional dependence, the sequence of the advection sweeps is altered in each time step and an alternating scheme is obtained. The above mentioned example is depicted in Fig. 21 for a two-step approach in two dimensions and Courant numbers of approximately $C_r = 0.3$ and $C_r = 0.7$. Apart from a slight smoothing of the steep gradients, due to the discrete distribution of the evaluation points, the quality of the shape of the circular wave is properly retained during the whole advection process.

Higher-order extensions can for instance be obtained using a three-step approach in 2D, where the advection is first performed in x-direction with half of the advection volumes, then in y-direction with the full advection volumes and finally again in x-direction, using the remainder of the advection volumes. Again, the alternation of the advection sweeps can be used to eliminate the directional dependence. Certainly, the numerical effort is increased about 50% in the 2D case, where one full additional advection sweep has to be performed and even more are required in the 3D case. Since the accuracy of the advection shapes is not increased considerably using this three-step approach, the following simulations will be restricted to two and three advection sweeps for the two and three dimensional case, respectively.

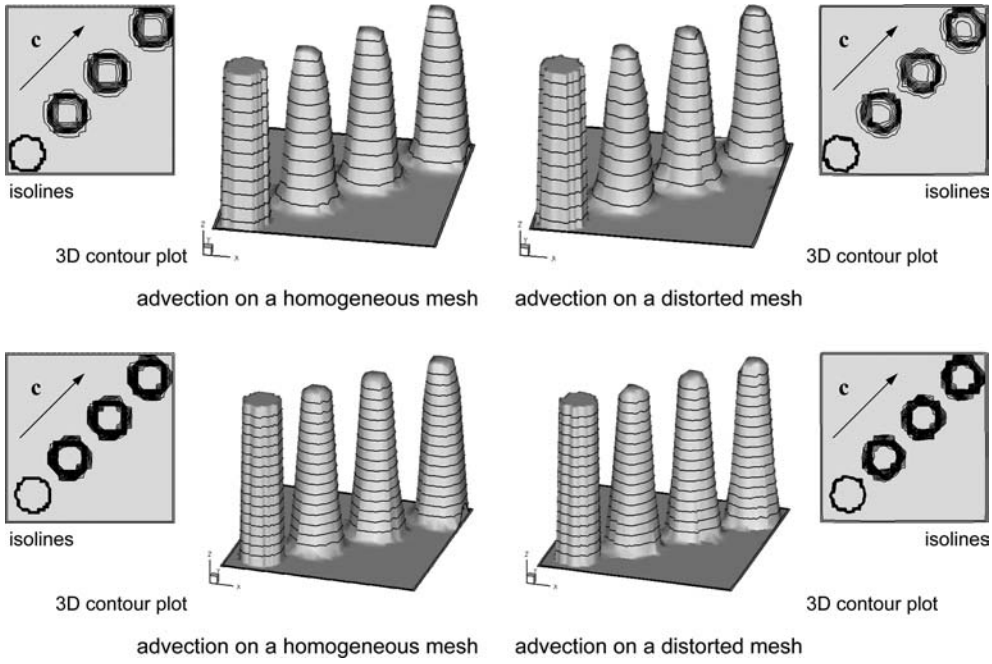

Fig. 21 Two-dimensional advection process of a circular wave using the two-step approach on a *left:* homogeneous mesh and *right:* distorted mesh with 30×30 elements and a convective velocity $\mathbf{c}$ at (*top*) $C_r \approx 0.3$ and (*bottom*) $C_r \approx 0.7$. Depicted are the isolines and a 3D contour plot

For the practical implementation in a multidimensional ALE method, the mesh nodes are relocated particularly for each spatial dimension and the advection process is performed subsequently. Clearly, for the case of a distorted mesh, this approach is strictly speaking an isotropic advection process, since due to the different orientations of the element edges the fluxes over all edges have to be considered. Indeed, the directional split minimizes the inaccuracies stemming from the overlap of the advection volumes that can safely be neglected.

4.7 Advecting nodal-based quantities

All advection schemes, described previously, are basically constructed for element-centered variables, where the fluxes between adjacent elements over the common edge can be determined directly. However, in practical problems also vertex-centered variables, like the total material displacement or the velocity, may also be required to be transported through the moving finite element mesh

To minimize the computational effort, it is highly recommended that the vertex-centered advection algorithm can directly be incorporated into the element-centered advection scheme of the last section. Hence, two different approaches can be constructed that use the volume fluxes and advection stencils, already determined for the element-based advection. The first approach, denoted as the SALE algorithm (not to be confused with the SALE algorithm), is based on an averaging process, where the vertex-centered quantities are first averaged to the element, advected and finally redistributed to the new element nodes ([2]). However, as outlined in [10], this algorithm is very diffusive and not monotone, i.e. unphysical oscillations are produced in the vicinity of steep gradients. Furthermore, the original quantities will not be retained, if the convective velocity approaches zero.

Another vertex-centered advection method that can likewise be incorporated into the element-based advection scheme is the half index shift (HIS) algorithm, developed in [11]. Here, the upstream vertex-centered variables $\boldsymbol{\Phi}^-$ are first projected to the element centroids using the projection operator $\mathcal{P}$. These element-centered quantities $\boldsymbol{\phi}^-$ can subsequently be advected using the element-centered framework of the TVD scheme to obtain the downstream element-centered values on the new mesh $\boldsymbol{\phi}^+$. Finally, $\boldsymbol{\phi}^+$ is projected back to the vertices by repetitively using the inverse projection operator. The three main steps can be summarized as follows

1. vertex-to-element proj.:

$$\boldsymbol{\phi}^- = \mathcal{P}\,\boldsymbol{\Phi}^-$$

2. advection phase:

$$\boldsymbol{\phi}^- \xrightarrow[\text{step}]{\text{advection}} \boldsymbol{\phi}^+ \tag{75}$$

3. element-to-vertex proj.:

$$\boldsymbol{\Phi}^+ = \mathcal{P}^{-1}\,\boldsymbol{\phi}^+,$$

where $\boldsymbol{\phi}$ and $\boldsymbol{\Phi}$ are now vectors, containing the element-centered and vertex-centered values of the quantity ϕ, respectively. Since the TVD advection scheme is of second-order accuracy in space, the HIS algorithm is also second-order accurate. Concerning the monotonicity properties of the advection scheme, the projection operator has to be chosen

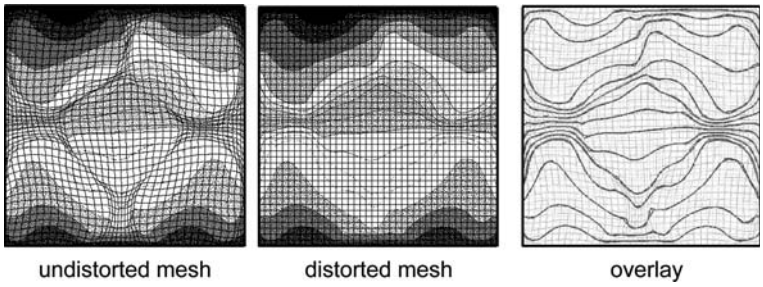

Fig. 22 Solution of the vertex-centered advection scheme for a typical heterogeneous material sample, consisting of five inclusions on a homogeneous and a distorted mesh; *left*: velocities in the vertical direction, *right*: overlay of the isolines of both meshes

properly, i.e. monotonicity has to be maintained in both projection directions, what is usually only fulfilled, if all coefficients of $\mathcal{P}$ have the same sign and the transformation matrix is diagonal. The simplest form that fulfills these requirements is the identity matrix $\mathcal{P} = \boldsymbol{I}$.

For the practical implementation, this means that each component of the vertex-centered variables at each vertex is assumed to be element-centered. Subsequently, the advection process is performed using Eq. (48) for a volume weighted advection, resp. Eq. (51) for a mass-weighted advection. Finally, the new element centered quantities are redistributed to the element nodes using the vertex-centered volume matrix $\boldsymbol{V}^+_{\text{node}}$ resp. mass matrix $\boldsymbol{M}^+_{\text{node}}$ of the downstream mesh

$$\begin{aligned} \boldsymbol{\Phi}^+ &= \frac{1}{V^+_{\text{node}}} \sum_n \boldsymbol{\phi}^+ V^+ \\ \text{resp.} \quad \boldsymbol{\Phi}^+ &= \frac{1}{M^+_{\text{node}}} \sum_n \boldsymbol{\phi}^+ M^+, \end{aligned} \tag{76}$$

where n is the number of elements, surrounding the current node, V^+_{node} and M^+_{node} are the downstream nodal volumes and masses, while V^+ and M^+ are the downstream element volumes and masses, respectively. Fig. 22 depicts a typical distribution of the velocities in a heterogeneous material under certain loads before and after the advection process, where a comparison of the isolines shows that both distributions generally match.

5 Advecting material-associated quantities

In contrast to volume-associated quantities, material-associated quantities are persistently connected to a certain material phase. As mentioned before, these material phases are distinguished by their respective volume fractions f in the VOF. The major advantage of the volume-of-fluid method in the Lagrangian step is that it can efficiently be incorporated into the governing equations using so-called mixture theories, where the contributions of the different materials are accounted for on the basis of these volume fractions (cf. Sect. 2.5). During the advection process in a MMALE method, different materials within a mixed element have to be transported over the corresponding element boundaries. For an accurate transport of the volume fractions and other material-associated variables, the material distribution and therefore the knowledge of the deformation of the material interfaces is of fundamental importance. Since only the volume fractions are stored, so-called interface reconstruction methods have to be applied within the advection step, where a mathematical parametrization of the boundary is determined.

Depending on the type and accuracy of these interface reconstruction algorithms, first- and second-order accurate approaches can be constructed. An extensive overview about classical reconstruction methods and other new developments can for instance be found in [59, 63] or [15]. In this context, the simplified line interface calculation (SLIC) method [46]) or the piecewise linear interface calculation (PLIC) method ([67]) should be mentioned due to their simplicity and efficient implementation capabilities. While the first approach assumes material boundaries which are aligned to the global Cartesian coordinate axes, the second approach allows an arbitrary orientation of the material interfaces within one element. With the knowledge of the position of the material interfaces, the volume fractions can be advected very efficiently by applying the finite-volume-based advection scheme described in Sect. 4.3.

The process of the interface reconstruction within the PLIC method and the transport of the material-associated quantities, especially the transport of the volume fraction, during the advection process will be described in the following sections.

5.1 Basic assumptions in the VOF method

The material distribution in the VOF method is represented by the volume fractions of each material k characterized by [cf. Eq. (11)]

$$\begin{aligned} &f^k = V^k / V \\ &\text{with} \quad 0 \leq f^k \leq 1 \quad \text{and} \quad \sum_k f^k = 1, \end{aligned} \tag{77}$$

where V is the total volume, while V^k represents the coherent volume of material k within a mixed element. For mixed material elements, f^k is between zero and one and sums to one for the union of all materials. The evolution equation for f^k can be derived from the balance of mass, included in the general form of the governing equations (6). Specifically,

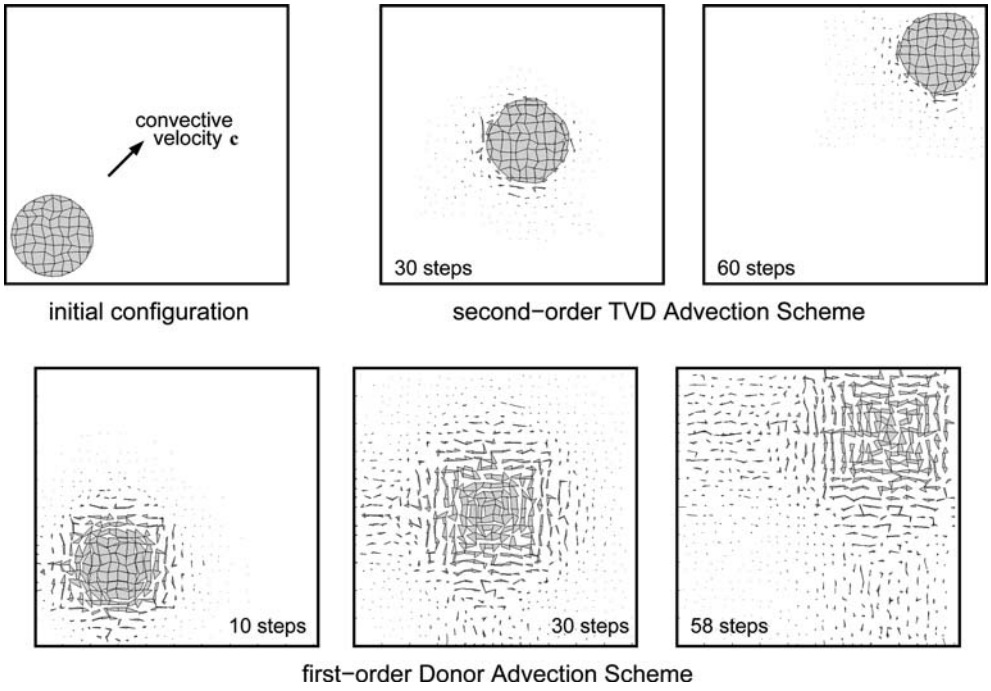

Fig. 23 Solution of the advection problem for the volume fraction for a single circular disk, advected in the diagonal direction of a 30 × 30 distorted, quadrilateral mesh ($C_r = 0.3$)

we obtain the following expression for the evolution of the density ϱ^k of material phase k

$$\frac{\mathrm{d}\varrho^k}{\mathrm{d}t} = \left.\frac{\partial \varrho^k}{\partial t}\right|_{\chi} + \operatorname{grad} \varrho^k \cdot \mathbf{c} = -\varrho^k \operatorname{div} \mathbf{v}^k = -\varrho^k \operatorname{div} \mathbf{v}, \tag{78}$$

where the last term follows from the fact that the deformation of the different materials within one mixed element is governed by the same velocity field, i.e. $\mathbf{v} = \mathbf{v}^k$. Inserting $\varrho^k = M^k / V^k$, $\mathrm{d}M^k/\mathrm{d}t = 0$ and $V^k = f^k V$, with the mass M^k of material phase k, we obtain the evolution equation of the material-associated volume fraction

$$\frac{\mathrm{d}f^k}{\mathrm{d}t} = \left.\frac{\partial f^k}{\partial t}\right|_{\chi} + \operatorname{grad} f^k \cdot \mathbf{c} = 0. \tag{79}$$

Thus, the volume fraction is a so-called Lagrangian invariant, i.e. during the Lagrangian step, the volume fraction f^k of material k does not change within the element. The finite element matrices can therefore be computed by only using the knowledge of the volume fractions in each element. This leads to a very efficient implementation of the Lagrangian step, where the volume fractions can be accessed directly as internal element variables.

In the simplest approach, the solution of the above evolution equation for the volume fractions can be obtained using either of the advection approaches, described in the preceding section, e.g. the first-order donor or the second-order TVD advection scheme. Figure 23 shows the advection process of a single two-dimensional disk in the diagonal direction of a squared computational domain on a distorted mesh. Unfortunately the initially coherent material phases disperse after only a few time steps since the material distributions are not accounted for during the advection process. Due to the diffusive properties, this effect gets worse for the first-order advection approach and it is obvious that these approaches are not applicable in an ALE finite element method, where the final solution would deteriorate considerably.

5.2 Interface reconstruction in the VOF method

During the advection step, the volume fractions and the material-associated quantities have to be advected by considering the material distribution and the position of the material interface to conserve the different phase volumes. Since the VOF method implies that the material interfaces are not traced explicitly in time, the interfaces have to be reconstructed on demand, based on the volume fractions in a small patch of adjacent elements.

In the following, the second-order accurate PLIC method should be applied, where the material interfaces are approximated with straight lines or plane surfaces in two and three spatial dimensions, respectively. In contrast to the SLIC approach, the orientation of the surface normals can be chosen arbitrarily to account for an accurate orientation of the material interfaces. Therefore, each material surface Γ is represented element-wise by the following implicit equation (cf. Fig. 24)

$$\Gamma: \quad \hat{\mathbf{n}} \cdot \mathbf{x} - d = 0, \tag{80}$$

where $\hat{\mathbf{n}} \in \mathcal{R}^n$ is the surface normal of unit length in n spatial dimensions, $d \in \mathcal{R}$ is a surface constant with $-\infty < d < \infty$, representing the shortest distance of the surface from the origin and $\mathbf{x}$ can be any point on the surface. The key point of the

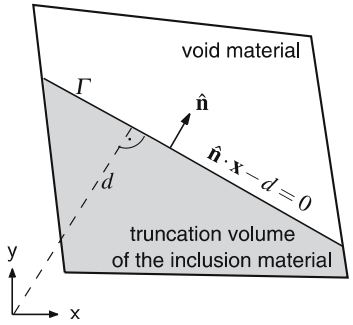

Fig. 24 Linear approximation of a 2D material interface Γ and definition of the surface parameters $\hat{\mathbf{n}}$ and d

interface reconstruction method is the proper determination of the surface parameters, i.e. the normal $\hat{\mathbf{n}}$ and the constant d. In general, the advection process of the volume fractions can be divided into three main steps:

1. First, an approximation of the surface normal is computed from the information of the adjacent elements. To improve the interface reconstruction, a post-smoothing procedure for the normal can optionally be applied using an iterative process.
2. In a second step, the material boundary is reconstructed, according to the volume fraction of the corresponding element and material using the normal, obtained from the first step. In case of a linear, first-order reconstruction (line in 2D; plane surface in 3D) this problem is unique and can be solved by determining the truncation volumes.
3. Finally, the advection volumes of each material are computed and updated element-wise in the material advection phase.

In the following the algorithms, necessary for these three steps will be presented and discussed in more detail. An overview of different methods and recent developments in VOF interface tracking algorithms is given in [15] or [54].

5.2.1 Determination of the surface normal

The determination of the surface normal $\hat{\mathbf{n}}$ within the mixed-material elements is the most important aspect of the interface reconstruction process, since it highly influences the final accuracy and quality of the reconstructed material shape. Unfortunately, this process is not unique and therefore approximations have to be accepted. Much effort has been made by different researchers to develop accurate surface normals even for the geometrically more complex three dimensional case. Most of these methods are based on finite difference stencils, least-squares fits, error minimization and other geometric constructs. Second-order methods can be obtained by combining these methods, e.g. computing an approximation of the normal and improve the normal using a local least-squares procedure. In the following, use should be made of the structure of the finite element mesh, where logical mesh directions exist and a transformation from the local to the global coordinate axes are avoided.

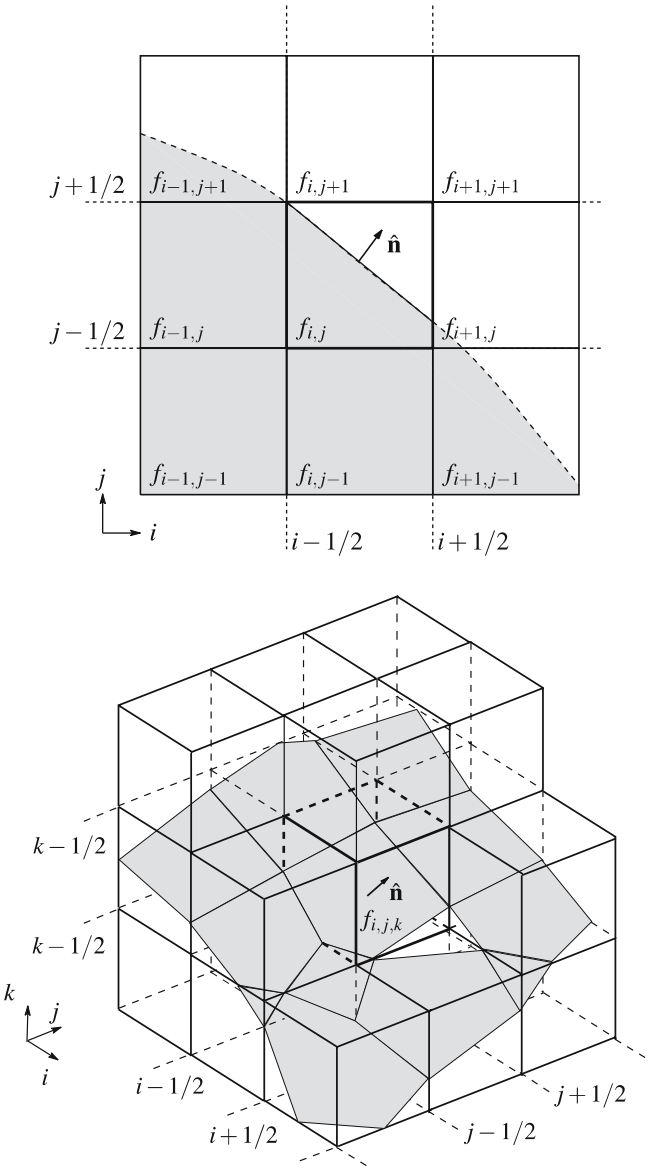

Fig. 25 Numbering of nodes and elements and approximation of the surface normal in element $(i, j(, k))$ for the two and three dimensional case in a 9/27 element patch

Probably the most promising approach to get an approximation of the normal was proposed by [67] and is based on the spatial gradient of the volume fractions

$$\hat{\mathbf{n}} \approx \frac{\text{grad } f^k}{|\text{grad } f^k|}, \tag{81}$$

which is normalized to unit length. Since the gradient is not a smooth function in space, it can clearly not be computed exactly and different schemes of first- and second-order accuracy can be used to approximate the gradient using the discrete distribution of the volume fractions. A very accurate approach was derived by [68]. The method is based on a nine-point finite difference stencil in two dimensions, resp. a 27-point stencil in three dimensions, formed by the volume

fractions of a patch of adjacent elements (sketched in Fig. 25). Using a finite difference notation, the three spatial components of the gradient of f^k in the current element can be approximated as

$$\frac{\partial f^k}{\partial x_1} = \frac{\bar{f}^k_{i+1,j,k} - \bar{f}^k_{i-1,j,k}}{2\,h_\xi} \quad \frac{\partial f^k}{\partial x_2} = \frac{\bar{f}^k_{i,j+1,k} - \bar{f}^k_{i,j-1,k}}{2\,h_\eta}, \quad \text{and} \quad \frac{\partial f^k}{\partial x_3} = \frac{\bar{f}^k_{i,j,k+1} - \bar{f}^k_{i,j,k-1}}{2\,h_\zeta}, \tag{82}$$

where $\bar{f}^k_{i+1,j,k}$ is a weighted average of the volume fraction of material k and h_ξ, h_η and h_ζ are the characteristic element lengths in the three corresponding local element coordinate directions. The weighted difference $\bar{f}_{i+1,j,k}$ for element (i, j, k) is computed according to

$$\begin{aligned}\bar{f}^k_{i+1,j,k} = \frac{1}{16}\big(&f^k_{i+1,j-1,k-1} + f^k_{i+1,j-1,k+1} \\ &+ f^k_{i+1,j+1,k-1} + f^k_{i+1,j+1,k+1} \\ &+ 2\,(f^k_{i+1,j-1,k} + f^k_{i+1,j+1,k} + f^k_{i+1,j,k-1} \\ &+ f^k_{i+1,j,k+1}) + 4\,f^k_{i+1,j,k}\big).\end{aligned} \tag{83}$$

For the two-dimensional case, the above form simplifies to

$$\bar{f}^k_{i+1,j} = \frac{1}{4}\left(f^k_{i+1,j-1} + 2\,f^k_{i+1,j} + f^k_{i+1,j+1}\right). \tag{84}$$

In Figs. 26 and 27, some examples of Youngs normal reconstruction method for the two and three dimensional case are depicted. A circle/sphere with diameter 7 that is embedded in a discrete domain with dimensions $10 \times 10(\times 10)$ is depicted, where the mesh density is chosen to be 15 elements per spatial direction. The reconstruction is performed on both, an undistorted and a distorted grid. Even though the reconstruction of the circular shapes shows some unsmooth transitions between adjacent elements that are due to a deterioration of the quality of the finite difference approximation for the normal gradient in case of a distorted element geometry, the reconstructed shapes are very accurate. Indeed, this is not the case for the cubic shapes, since the unsmooth corners and edges cannot be represented by a linear approximation of the surfaces within each element. In this case, the mesh has to be refined, to resolve the sharp edges with sufficient accuracy (cf. Fig. 28, where the number of elements has been increased from 15 to 30 elements per spatial direction).

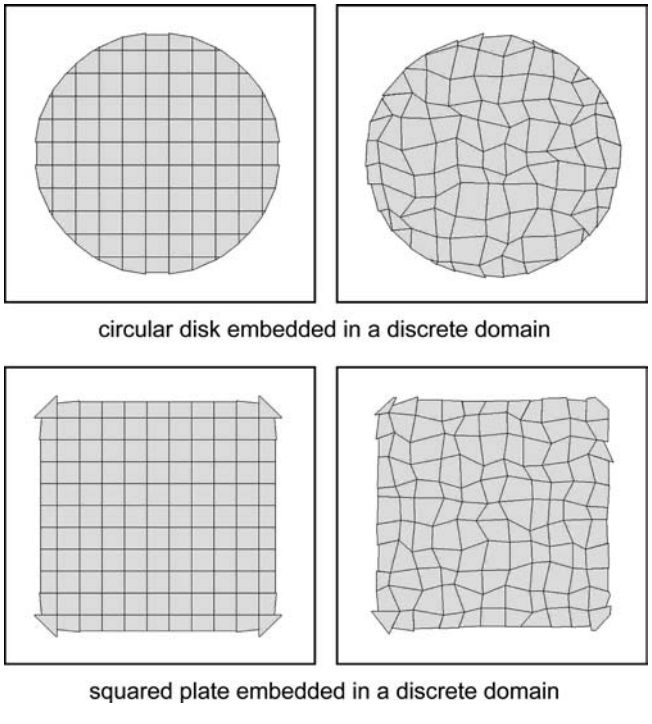

Fig. 26 Results of the interface reconstruction using the surface normal following [68] for a circular disk and a square on a homogeneous and a distorted (15×15) grid in two spatial dimensions

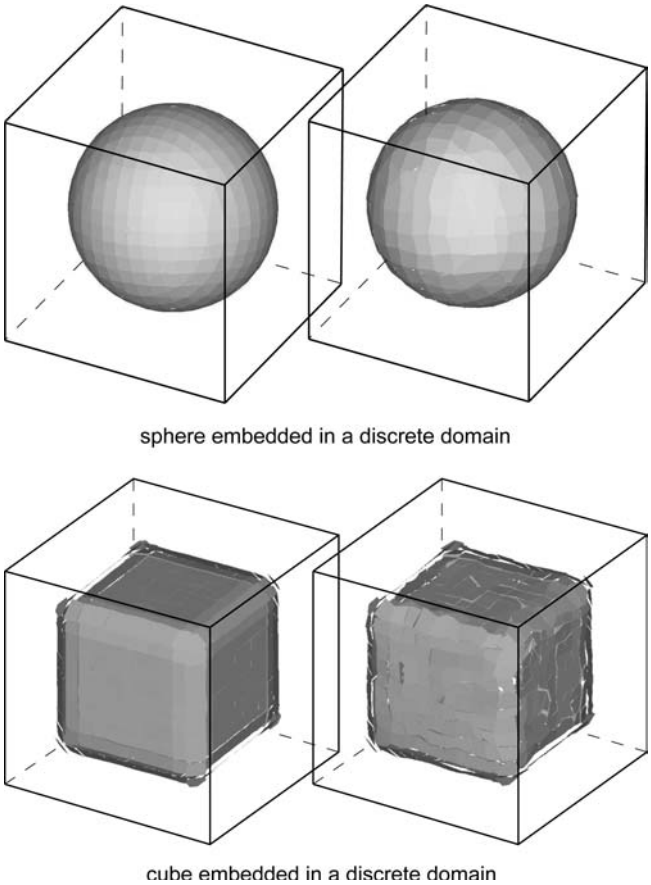

Fig. 27 Results of the interface reconstruction using the surface normal following [68] for a sphere and a cube on a homogeneous and a distorted (15×15×15) grid in three spatial dimensions

An improvement of the normal determination in the two- and three-dimensional case can often be achieved using a least-squares volume-of-fluid interface reconstruction algorithm (LVIRA – [52]), based on the minimization of the following potential in each $3 \times 3/3 \times 3 \times 3$ element patch

$$G(\hat{\mathbf{n}}) = \frac{1}{2}\left(V^f - V(\hat{\mathbf{n}})\right)^2 \qquad \rightarrow \text{MIN!}, \tag{85}$$

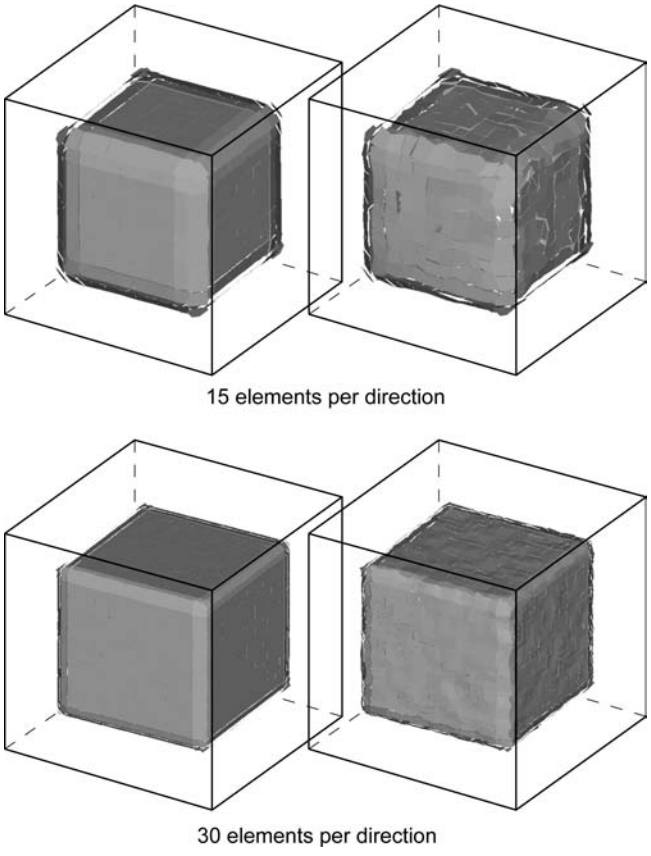

Fig. 28 Results of the interface reconstruction using the surface normal following [68] for a cube on an undistorted and a distorted grid in three spatial dimensions for two different mesh densities

where $V^f = f\,V$ is the inclusion volume in the element patch computed from the volume fractions, while $V(\hat{\mathbf{n}})$ is the volume under the straight surface line $\hat{\mathbf{n}}\cdot\mathbf{x}-d$, in dependence of the surface normal $\hat{\mathbf{n}}$ of the center element. While V^f can easily be computed using the volume fractions, no closed-form can be given for $V(\hat{\mathbf{n}})$. Thus an iterative minimizer for the new surface normal $\hat{\mathbf{n}}$ has to be applied. This improvement works fine on homogeneous meshes for arbitrary surface geometries, whereas for a general distorted mesh, several local minima can possibly occur for the above minimization problem and a stable solution can often not be attained, depending on the deformed element-shapes in the patch.

Indeed, another method, referred to as the Schwartz algorithm, works fine even on distorted meshes. This method first predicts the surface normal $\hat{\mathbf{n}}$ for the center element of a patch, using the gradient-based method mentioned above. Subsequently, the surface constants d are determined in the current and the adjacent elements, assuming the normal $\hat{\mathbf{n}}$ for all elements in the patch. In a third step, the center points of the reconstructed interfaces are connected with straight lines in the two-dimensional case and the normals $\hat{\mathbf{n}}_1$ and $\hat{\mathbf{n}}_2$ are obtained (cf. Fig. 29). The improved normal $\bar{\mathbf{n}}$ can then be obtained by averaging the two normals $\hat{\mathbf{n}}_1$ and $\hat{\mathbf{n}}_2$ of the connection lines as $\bar{\mathbf{n}} = \frac{1}{2}\left(\hat{\mathbf{n}}_1 + \hat{\mathbf{n}}_2\right)$. Note that this step requires the proper determination of adjacent elements containing the material boundary.

The reconstructed shape using Youngs interface normal calculation and the above mentioned improvement are depicted in Fig. 29 (right) for the circular shape on a distorted grid in two spatial dimensions. As expected, the interface shows a very smooth transition between adjacent elements that is superior to the shapes, depicted in Fig. 26. Additionally, the reconstruction was performed for the rectangular material sample, where again in the vicinity of the sharp edges, the quality of the surface transitions deteriorates considerably, but still shows an improved shape, compared to Fig. 26. Note that this problem only occurs if sharp edges of different materials are accounted for. In this case, the mesh has to be refined appropriately. However, in a micromechanical problem, where usually only spherical or approximately spherical inclusions are considered, this problem is not significant.

Unfortunately, these above mentioned improvement gets much more complicated in three spatial dimensions, since the choice of the elements required for the determination of the adjacent normals $\hat{\mathbf{n}}_1$ and $\hat{\mathbf{n}}_2$ is not unique. Furthermore, the surface constants have to be determined for all mixed elements in the patch. As will be outlined in the following paragraph, this step requires an iterative procedure and the numerical overhead increases considerably. For this reason, Youngs approximation is found to be sufficient for the three dimensional case.

5.2.2 Determination of the surface constant

In the second step, the position of the material surface in space has to be determined by choosing the surface parameter

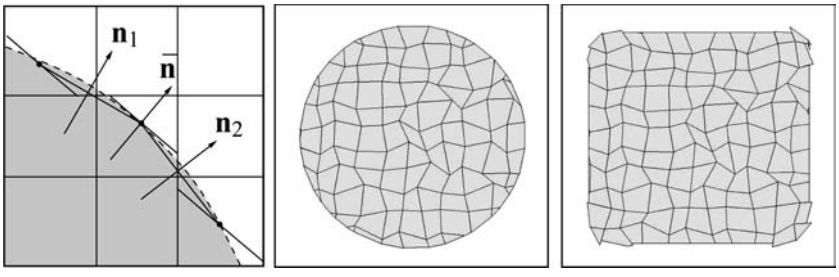

Fig. 29 Improvement of the surface normal for the two-dimensional case; *left*: element patch for the application of the Schwartz algorithm and *right*: comparison of the quality of the reconstructed surface normal for a circular and a rectangular material sample on a distorted grid

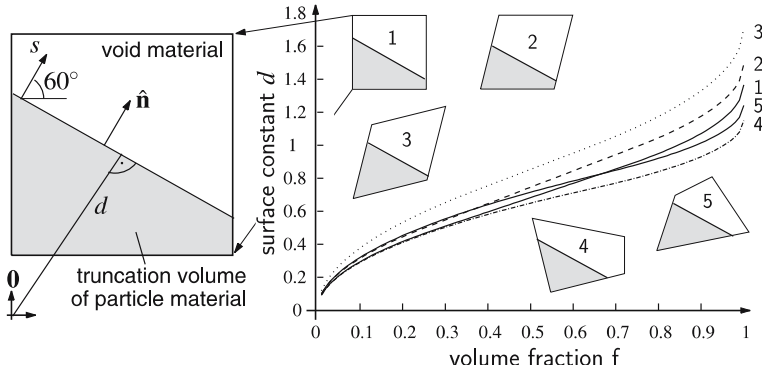

Fig. 30 Dependence of the surface constant d from the volume fraction f for different shaped elements. The surface is moved along the local coordinate s and the surface constant is evaluated. The resulting non-linear distribution is depicted on the right

d based on the given surface normal $\hat{\mathbf{n}}$. In contrast to the determination of $\hat{\mathbf{n}}$, which can only be done approximately, the surface constant can be determined exactly as a function of the surface normal, using the volume fraction f^k of the current element and material phase to conserve the different material volumes. The general approach is to compute the truncation volumes arising from the intersection of the approximated surface with the element volume. In the fluid-mechanics community, the current element is often mapped onto a reference element, and a certain number of possible intersection cases are distinguished and compared (see e.g. [29] or the overview paper of [15]). However, this approach is only accurate and applicable for undistorted or uniformly distorted meshes, where the spatial mapping to the reference element is constant. For the general case of a distorted element, this mapping is non-constant and has to be approximated using an iterative process, where the computational effort is increased considerably. Therefore, another approach should be used here that determines the truncation volumes directly using the divergence theorem (see [54]). In the following, these truncation volumes will be denoted as A_{tr} for the two-dimensional case and V_{tr} in the three-dimensional case. With the knowledge of the truncation volumes, the surface constant can be obtained using an efficient iterative process. Starting with an initial guess for d, Eq. (80) is evaluated, the truncation volume of the planar surface with the element is computed and subsequently, compared with the volume fraction of the current element. The error in the volume of material k is then given by the following expression

$$e_v^k(d^k) = V(d^k) - V^k = V(d^k) - f^k\, V, \tag{86}$$

where $V(d^k) = V_{\mathrm{tr}}(d^k)$ is the truncation volume of material k as a function of the surface constant d^k, while $V^k = f^k\, V$ is the aspired volume of the inclusion material, prescribed by the volume fraction f^k. If the error is not zero, the surface constant has to be adapted iteratively.

Generally, the dependence of the surface constant d from the volume fraction f is a non-linear function, even in the two dimensional case. This is depicted in Fig. 30, where a selection of different shaped elements has been examined for a prescribed example surface normal vector $\hat{\mathbf{n}}$. The above problem leads to a one-dimensional minimization problem to minimize the non-linear error function $e_v(d)$. The function minimization is performed using *Brent's method* (see e.g. [51]) that is based on a gradient-free minimization scheme. Each iteration step fits a quadratic polynom through three consecutive evaluation points. The minimum of the quadratic polynom is computed and chosen as an improved solution point. The iteration proceeds, unless an accurate minimum is achieved. Although the function evaluation to compute the truncation volumes $V(d)$ is relative expensive, Brent's method leads to a relatively fast convergence, since only one function evaluation per iteration step is required. Convergence is usually achieved after approximately 6–11 iterations, depending on the volume fraction.

The main effort for the determination of the surface constant is the proper determination of the truncation volumes, that originate from the intersection of a straight line or plane surface, described by $\hat{\mathbf{n}}$ and d, with the distorted quadrilateral or hexahedral element. This process is based on the divergence theorem, described in Sect. 2.6 [Eq. (15)]. In the following, the computation of the truncation volumes in two and three spatial dimensions should be addressed.

Determination of the polygon volumes in two spatial dimensions The determination of the polygon area A_{tr} in two spatial dimensions can easily be performed on the basis of the divergence theorem, where the area integral in Eq. (15) is separated into a sum of surface integrals

$$A_{\mathrm{tr}} = \int_{\Omega_{\mathrm{tr}}} \mathrm{d}v = \frac{1}{2} \sum_{s=1}^{n_s} \int_{\Gamma^s} \mathbf{x} \cdot \mathbf{n}^s \, \mathrm{d}\Gamma^s \tag{87}$$

that reduce to line integrals. n_s denotes the number of straight polygon edges, ranging from 3 to 5 and $\mathbf{n}^s$ is the (constant) normal of edge s (Fig. 31). The line integration is performed analogous to the approach given in Sect. 2.6 and we obtain the total truncation area of the polygon to

$$A_{\mathrm{tr}} = \frac{1}{2} \sum_{s=1}^{n_s} \left(x_1^s\, y_2^s - x_2^s\, y_1^s \right), \tag{88}$$

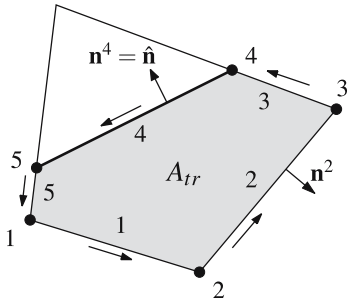

Fig. 31 Determination of the truncation polygon using the polygon edges in 2D

with the start and end coordinates of each polygon line $\boldsymbol{x}_1^s$ and $\boldsymbol{x}_2^s$, respectively. The above form requires the determination of the vertices of the truncation polygons in a proper order. This can be obtained by looping the element edges, generating the element edge vectors $\boldsymbol{x}(\xi) = \boldsymbol{x}_i + \xi\, \boldsymbol{v}_i$ with $\boldsymbol{v}_i = \boldsymbol{x}_i' - \boldsymbol{x}_i$ (the node $\boldsymbol{x}_i'$ is the successor node to $\boldsymbol{x}_i$) and inserting the element edge vectors into the surface equation (80). The current edge has an intersection point with Γ, if $0 \le \xi \le 1$.

Determination of the polygon volumes in three spatial dimensions In the three dimensional case, the determination of the truncation volumes is much more complicated. The foundation for the approach is again the divergence form Eq. (15), where the truncation volume can be represented as

$$V_{\text{tr}} = \int_{\Omega_{\text{tr}}} \mathrm{d}v = \frac{1}{3} \int_{\Omega_{\text{tr}}} \operatorname{div} \mathbf{x}\, \mathrm{d}v = \frac{1}{3} \int_{\Omega_{\text{tr}}} \operatorname{div} (\mathbf{x} - \hat{\mathbf{n}}\, d)\, \mathrm{d}v. \tag{89}$$

The last form follows from the condition that the normal of the material interface $\hat{\mathbf{n}}$ is constant on the plane surface and thus $\operatorname{div} \hat{\mathbf{n}} = 0$. The volume integral can now be converted into a surface integral, where the surface of the truncation volume is splitted into n_f element surfaces Γ_{tr}^s and the reconstructed material interface Γ_{tr}

$$3\, V_{\text{tr}} = \int_{\Gamma_{\text{tr}}} (\mathbf{x} - \hat{\mathbf{n}}\, d) \cdot \mathrm{d}\boldsymbol{\Gamma} = \sum_{s=1}^{n_f} \int_{\Gamma_{\text{tr}}^s} (\mathbf{x} - \hat{\mathbf{n}}\, d) \cdot \mathbf{n}^s\, \mathrm{d}\Gamma^s + \int_{\Gamma_{\text{tr}}} (\mathbf{x} - \hat{\mathbf{n}}\, d) \cdot \hat{\mathbf{n}}\, \mathrm{d}\Gamma. \tag{90}$$

Since the dot product in the second part of the right-hand side vanishes for each point on the material interface, the equation can be reduced to the solution of the following surface problem

$$V_{\text{tr}} = \frac{1}{3} \sum_{s=1}^{n_f} V^s \quad \text{with} \quad V^s = \int_{\Gamma_{\text{tr}}^s} (\mathbf{x} - \hat{\mathbf{n}}\, d) \cdot \mathbf{n}^s\, \mathrm{d}\Gamma^s. \tag{91}$$

Note that the integration process is only performed over the truncation surface Γ_{tr}^s, defining the part of the element face s that lies under the material surface Γ^s [grey-shaded region in Fig. 32 (right)].

An analytic approach to solve the above integral is given in [39]. Each surface Γ_{tr}^s of an arbitrary deformed brick element is defined by four vertex points that are connected with straight lines in the three-dimensional space (Fig. 32). The intersection lines of Γ^s with the element surfaces are in general curved lines. Each of these ruled surfaces can be parametrized by a local coordinate system (α, β), as introduced in Eq. (23)

$$\mathbf{x} = \mathbf{x}_1 + \alpha\, (\mathbf{x}_2 - \mathbf{x}_1) + \beta\, (\mathbf{x}_4 - \mathbf{x}_1) + \alpha\, \beta\, \mathbf{d}. \tag{92}$$

Subsequently, the ruled surface element is given by Eq. (25)

$$\mathrm{d}\boldsymbol{\Gamma}^s = \mathbf{n}^s\, \mathrm{d}\Gamma^s = [\mathbf{X}_1 + \alpha\, (\mathbf{X}_3 - \mathbf{X}_4) + \beta\, (\mathbf{X}_3 - \mathbf{X}_2)]\, \mathrm{d}\alpha\, \mathrm{d}\beta, \tag{93}$$

with the cross vectors $\mathbf{X}_i$, defined in Eq. (24). Insertion of the parametrization and the above surface element into Eq. (91) and performing some vector algebra, the following expression can be obtained

$$V^s = \left(\mathbf{x}_1 - \hat{\mathbf{n}}\, d\right) \cdot [\mathbf{X}_1\, K_{00} + (\mathbf{X}_3 - \mathbf{X}_4)\, K_{10} + (\mathbf{X}_3 - \mathbf{X}_2)\, K_{01}] - v_{\text{tet}}\, K_{11} \tag{94}$$

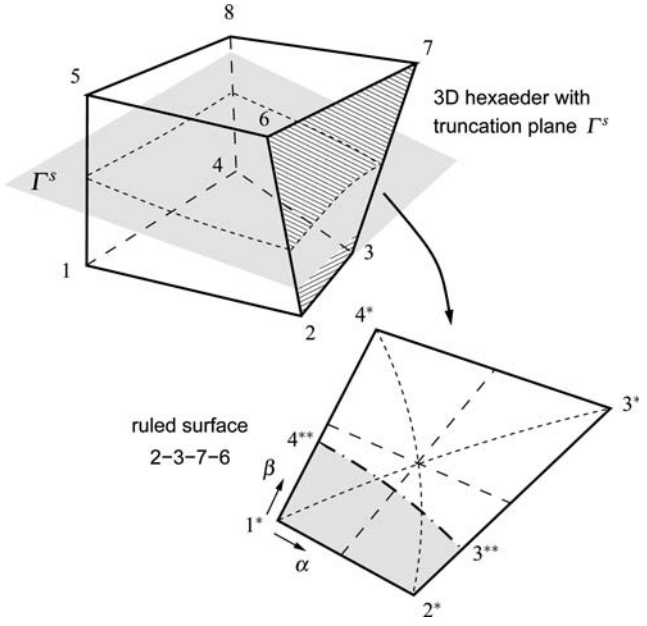

Fig. 32 *Top*: arbitrary deformed brick, composed of eight vertices, six ruled surfaces and truncation surface Γ^s; *bottom*: surface $(2-3-7-6)$ with local vertex labels 1*, 2*, 3* and 4*, curved surface intersection of Γ^s and intersection points of the surface with the element edges 3** and 4**

with

$$v_{\text{tet}} = \frac{1}{2}\,\mathbf{d}\cdot\mathbf{k} = (\mathbf{x}_1 - \mathbf{x}_2)\times(\mathbf{x}_2 - \mathbf{x}_3)\cdot(\mathbf{x}_3 - \mathbf{x}_4)$$
$$\text{and}\quad K_{nm} = \int_{\Gamma^s_{\text{tr}}} \alpha^n\,\beta^m\,\mathrm{d}\alpha\mathrm{d}\beta. \tag{95}$$

A closed-form solution of this problem is given in [39] and is obtained by analytically evaluating the K-integrals

$$V^s = \tfrac{1}{6}\sum_i \epsilon_i\, Y_i\, \tfrac{(d-d_i)^2}{\lambda_i} + \tfrac{v_{\text{tet}}}{2}\sum_i \epsilon_i\,[J_1(w_i) - 2\,J_2(w_i) + J_3(w_i)]\,\frac{(d-d_i)^4}{\lambda_i^2} \tag{96}$$

where d is the current surface constant, $d_i = \text{MIN}(d, \mu_i)$ and $\mu_i = \hat{\mathbf{n}}\cdot\mathbf{x}_i$ denote the parameters of a parallel surface through the four vertex nodes $\mathbf{x}_i$ (i = 1,. . .,4). Subsequently, using $\epsilon_1 = \epsilon_3 = +1$ and $\epsilon_2 = \epsilon_4 = -1$ the remaining parameters can be defined as follows

$$\begin{aligned} Y_i &= (\mathbf{x}_i''' - d\,\hat{\mathbf{n}})\cdot(\mathbf{x}_i - d\,\hat{\mathbf{n}})\times(\mathbf{x}_i' - d\,\hat{\mathbf{n}}),\\ \lambda_i &= \epsilon_i\,(\mu_i - \mu_i')\,(\mu_i - \mu_i''')\\ w_i &= \frac{v}{\lambda_i}\,(d - d_i),\quad \text{and}\quad v = \hat{\mathbf{n}}\cdot\mathbf{B}. \end{aligned} \tag{97}$$

The bracketed term $[J_1 - 2\,J_2 + J_3]$ can further be specified by

$$[J_1(w) - 2\,J_2(w) + J_3(w)] = 2\sum_{n=0}^{\infty}\frac{(-w)^n}{(n+2)\,(n+3)\,(n+4)}. \tag{98}$$

This analytical solution is very efficient and can mostly be used. However, there are two special cases, where this direct solution fails

1. in the first case, the surfaces with normal $\hat{\mathbf{n}}$ through two adjacent surface nodes $\mathbf{x}_i$ have the same distance from the origin, i.e. $\mu_i = \mu_i'$. Therefore, following Eq. $(97)_2$, the parameter λ_i vanishes and the corresponding terms in Eq. (96) cannot be properly computed,
2. the second case addresses severely distorted elements, where the series in Eq. (98) is not necessarily defined. Here, the absolute value of w_i in Eq. $(97)_3$ may exceed 1, i.e. if ABS $(w_i) \geq 1.0$ and the series approaches infinity.

Unfortunately, the above mentioned publication does not give any results for these specific cases and a fall-back solution has to be applied for the integration of the corresponding surface integrals, if one of these cases is detected during the integration process. In the following, a simple numerical integration procedure of Eq. $(91)_2$ will be performed for the surface element. Here, first the intersection points of the material interface with the edges of the surface element have to be determined [points 3** and 4** in Fig. 32 (right)]. This leads to a certain number of n points, defining the truncation surface. If $n \leq 4$, the integration can simply be performed by approximating the region with a triangular or a quadrilateral element and applying a standard Gauss integration procedure, resp. the analytical solution, given in Eq. (27). However, if more than four points are detected, a submeshing procedure has to be applied, where the resulting surface is approximated using multiple triangular or quadrilateral elements. However, since the straight edges of this submesh are not able to capture the exact geometry of the ruled intersection surface, an approximate solution has to be accepted. Indeed the errors introduced by this procedure are relatively small and further improvements, like e.g. the use of higher-order elements, are not required.

5.2.3 Advecting material-associated volumes

In the last step, the advection approach of the material-associated variables in terms of the volume fraction f^k is presented that accounts for the evolution of f^k during the transport step

$$\left.\frac{\partial f^k}{\partial t}\right|_{\chi} + \text{grad}\ f^k\cdot\mathbf{c} = 0. \tag{99}$$

As seen before, the application of a TVD advection scheme would lead to a dispersion and a loss of coherence of the considered material phases. Since the volume fractions are directly associated with a certain type of material, the transport volumes of the different materials have to be considered to fulfill the local balance of mass after the advection step. This requires the determination of the correct advection volumes of each material during the advection process to prevent the disintegration and dispersion of the coherent material phases. As before, the advection process for the volume fractions is based on the volume-weighted advection scheme, given in Eq. (48)

$$f^{k^+}\,V^+ = f^{k^-}\,V^- - \Delta t\sum_s \mathcal{F}_f^s \quad \text{with}\quad V^+ = V^- - \Delta t\sum_s \mathcal{F}^s, \tag{100}$$

where the flux rate $\mathcal{F}_f^s$ over the boundary s is computed according to the current material distribution. Here, four main steps have to be considered (cf. Fig. 33)

1. In the first step, the material interface of the current element is reconstructed from the volume fractions. Clearly, this is only necessary, if the current element contains more than one type of material $\rightarrow$ material interface given by: $\Gamma:\ \hat{\mathbf{n}}\cdot\mathbf{x} - d = 0$.
2. In the second step, the total flux volumes are determined from the flux polygon by back-tracing the characteristics $-\Delta t\,\mathbf{c}_1$ and $-\Delta t\,\mathbf{c}_2$ in the upstream direction. The polygon consists of the two edge nodes $\mathbf{x}_1$ and $\mathbf{x}_2$ and the two additional nodes $\mathbf{x}_3 = \mathbf{x}_2 - \Delta t\,\mathbf{c}_2$ and $\mathbf{x}_4 = \mathbf{x}_1 - \Delta t\,\mathbf{c}_1$.

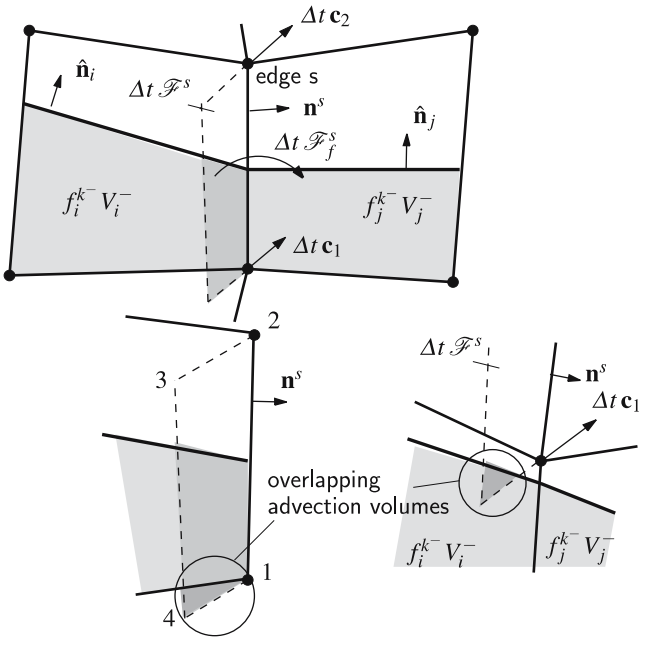

Fig. 33 Material-volume based advection process of the volume fractions; computation of the advection volumes; the overlapping advection volume in the lower center is considered by the advection approach, while the overlapping volume on the lower right is not accounted for

3. In step three, the truncation volumes $\Delta t\, \mathcal{F}_f^s$ are computed from the truncation polygons of the material surface that is constructed from the total flux polygon using the algorithms described in the last section.

4. The last step finally provides the computation of the new volume fractions using the accumulated sum of the fluxes $\Delta t \sum_s \mathcal{F}_f^s$ according to the above equation.

In case of a homogeneous, undistorted mesh, aligned to the global Cartesian coordinate axes, the material advection volumes are determined exactly, if the multidimensional sweep approach is chosen, where the sweeps are performed in the direction of the Cartesian axes. Unfortunately, in a finite element ALE framework, the advection process is usually performed on a distorted mesh. In this case, the advection volumes of different edges within one element can interact and overlap with adjacent elements. Depending on the distribution of the material surfaces, special cases can be constructed, where the material advection volumes are not determined correctly [cf. Fig. 33 (right)]. These influences get worse in case of large local Courant numbers, i.e. advection volumes.

With slight modifications, the above material advection scheme can directly be incorporated into the element-based TVD advection procedure, as was presented in Alg. (4.1), where the multidimensional advection process can again be accurately performed using the one-dimensional sweep process. The final global VOF advection algorithm is given in Alg. (5.1). Since the above described advection process is not exact on distorted meshes, some rough corrections are applied at the end of each advection sweep to ensure a consistent distribution of the volume fractions after the advection step

Algorithm 5.1 Schematic global advection algorithm for the volume fractions f^k

Requires: upstream geometry $\mathbf{x}^-$ and volume fractions f^{k-}; convective displacement increment $\mathbf{u_c} = \Delta t\, \mathbf{c}$; element connectivity list

Provides: advected material-associated volumes and new volume fractions f^k

schematic VOF advection algorithm showing the steps necessary for each spatial advection sweep:

1. setup neighbor informations of adjacent elements from element connectivity list (only first time)
2. loop all elements with prescribed convective velocity $\mathbf{c} \neq \mathbf{0}$ at the vertices
   (a) determine the number of materials within the current element
   (b) reconstruct the material surface for each material k with $0 < f^k < 1 \quad \rightarrow (\hat{\mathbf{n}}, d)^k$
   (c) loop element edges
   - determine advection volume flux $\left(\Delta t\, \mathcal{F}^s\right)$ due to Eq. (49) and nodal advection values; cycle inflow volume fluxes
   - update total element volume flux $\rightarrow\ \Delta t \sum_s \mathcal{F}^s$; subtract from current, add to adjacent element
   - if $0 < f^k < 1$ setup total flux polygon for current outflow element edge and calculate the truncation volume $\Delta t\, \mathcal{F}_f^s$, otherwise set $\Delta t\, \mathcal{F}_f^s = \Delta t\, \mathcal{F}^s$
   - update total material-associated volume fluxes $\rightarrow$ $\Delta t \sum_s \mathcal{F}_f^s$ for each element; subtract from current, add to adjacent element
3. second loop over all elements to perform global variable update
   (a) determine total upstream volumes V^- and update downstream volumes $V^+ = V^- - \Delta t \sum_s \mathcal{F}^s$
   (b) update downstream volume fractions f^k using the transport volumes $f^{k+} V^+ = f^{k-} V^- - \Delta t \sum_s \mathcal{F}_f^s$
4. perform global and local corrections to the new volume fractions

1. under- and overshots of the volume fractions are corrected, i.e. if $(f^k > 1.0 - \epsilon)$ set $f^k = 1.0$, resp. if $(f^k < \epsilon)$ set $f^k = 0.0$, where ϵ is chosen to be a very small, positive number (e.g. $\epsilon = 1.0 \times 10^{-8}$),
2. the volume fractions are rescaled to sum to 1.0, i.e. if $\sum_k f^k > 1.0$ set $f^k = f^k / \sum_l f^l$.

Numerical experiments have shown that the influence of these rough corrections are of minor order of magnitude and the masses of the different materials are usually conserved locally and globally. This will be examined in the following numerical examples section.

5.3 Numerical examples for the advection problem

In the following, the above presented VOF algorithm is verified by means of some simple advection examples in the two- and three-dimensional case. The advection of a single circular disk/sphere is performed in a region of dimensions 10^n with $n = 2$ (2D) or $n = 3$ (3D). Furthermore, the region is discretized using a spatially fixed structured 30^n quadrilateral resp. hexahedral finite element mesh. All advection processes are performed first on a homogeneous mesh and additionally

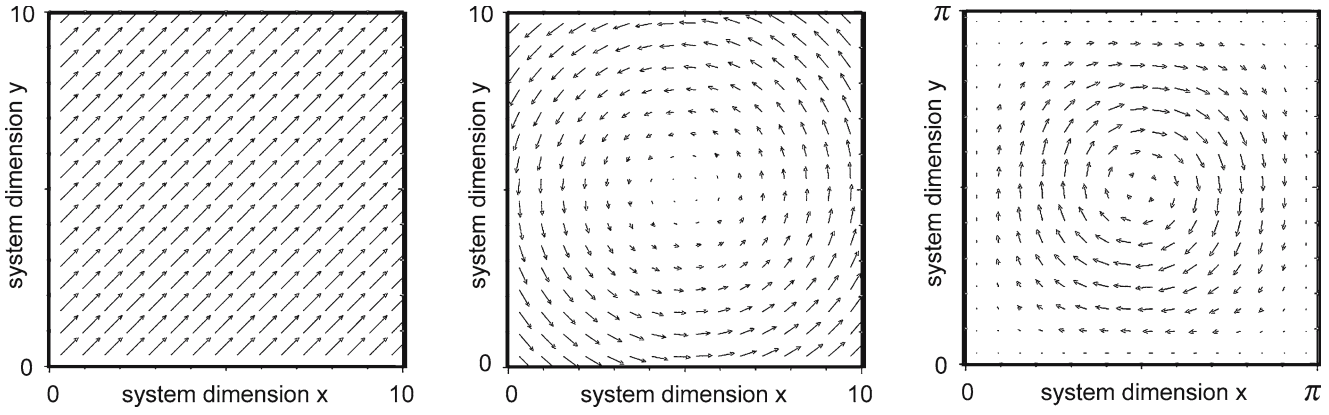

Fig. 34 Velocity fields for the three material advection tests; *left*: purely diagonal flow, *center*: rotational flow and *right*: single vortex flow

on a distorted mesh (cf. Fig. 16 for a 2D sketch), where three different Courant numbers, specifically $C_r = 0.3$, $C_r = 0.5$ and $C_r = 0.7$ are considered to examine the behavior at different advection volumes.

In the first example a circular disk/sphere is advected straight in the diagonal direction of the region, where the quality of the diagonal advection using the one-dimensional advection sweeps is verified. In the second example, the circular disc/sphere is subjected to a rotational velocity field around a center axis of the region and advected over one revolution. Note that both velocity fields lead to an incompressible advection process, where the shapes of the inclusions are physically preserved. In a third example, a compressible vortex flow is applied to a single, eccentric arranged circular disk in two dimensions, where the divergence term in Eq. (32) has to be accounted for, since div $\mathbf{c} \neq 0$. The corresponding velocity fields are depicted in Fig. 34 for the two-dimensional case.

Example 1 Diagonal advection of a circular disk/sphere The diagonal advection process is performed for a circular disk and a sphere with diameter 3 on a discrete 10^n ($n = 2, 3$) domain in two and three spatial dimensions, respectively. The domain is discretized as mentioned before. The results for the two-dimensional case are depicted in Fig. 35 for the homogeneous and the distorted mesh. Generally, the alternating one-dimensional advection sweeps to perform the advection process over the element diagonals again work very accurate and the effect of crosswind diffusion is almost eliminated. In contrast to the material-associated TVD advection scheme, depicted in Fig. 23, the circular shapes of the material sample remain coherent and the total volumes of the two materials are conserved during the whole advection process. For the homogeneous mesh, the alternating direction approach provides a – numerically – exact determination of the advection volumes and the advection process is very accurate for all three Courant numbers. However, in case of a distorted mesh, the solution deteriorates with an increasing Courant number due to the partly unconsidered material advection volumes, mentioned above. This deterioration leads to a dispersion of the material phase, where small fragments of the disk are detached from the initially coherent material.

The same effect can be observed in the three-dimensional case, depicted in Fig. 36, again for the homogeneous and distorted mesh. While in the homogeneous case, the material again remains coherent, the advection process on the distorted mesh leads to the material dispersion at large Courant numbers. Nevertheless, the advection process is very efficient and accurate, even on distorted meshes at small Courant numbers, compared to the TVD advection, showed in Fig. 23. Note that in case of the undeformed mesh, the analytical solution for the computation of the truncation volumes can be used, while this analytical solution may fail for a distorted element geometry in some cases and the fall-back solution has to be applied. Therefore, also the approximative character of the determination of the truncation volumes contributes to the dispersion of the material volume.

Following the literature, more improved results for the VOF method can e.g. be obtained using a combination with a MAC (*Marker and Cell*) scheme, where additionally to the volume fractions a certain number of marker points are added that describe the surface which can now be represented by a polygon (see e.g. [50]). However, these methods can be computationally very expensive since the (Lagrangian) motion of the marker points has to be traced during the non-Lagrangian deformation process (see e.g. [4] and references therein) and are thus not suitable in a finite element ALE framework, where more importance is concerned with efficiency and a small numerical overhead.

Example 2 Rotational advection of a circular disk/sphere In the second example, a single, eccentric arranged circular disk resp. sphere is rotated around a central axis of the computational domain. For the two-dimensional case, the solution of the advection process is depicted in Fig. 37 for the homogeneous and the distorted mesh, performed again for the three different Courant numbers $C_r = 0.3/0.5/0.7$. The prescribed velocity field leads to an alteration of the advection directions with respect to the orientation of the finite element mesh. Again, for the undeformed and the deformed mesh shape, the advection process is very accurate at low Courant

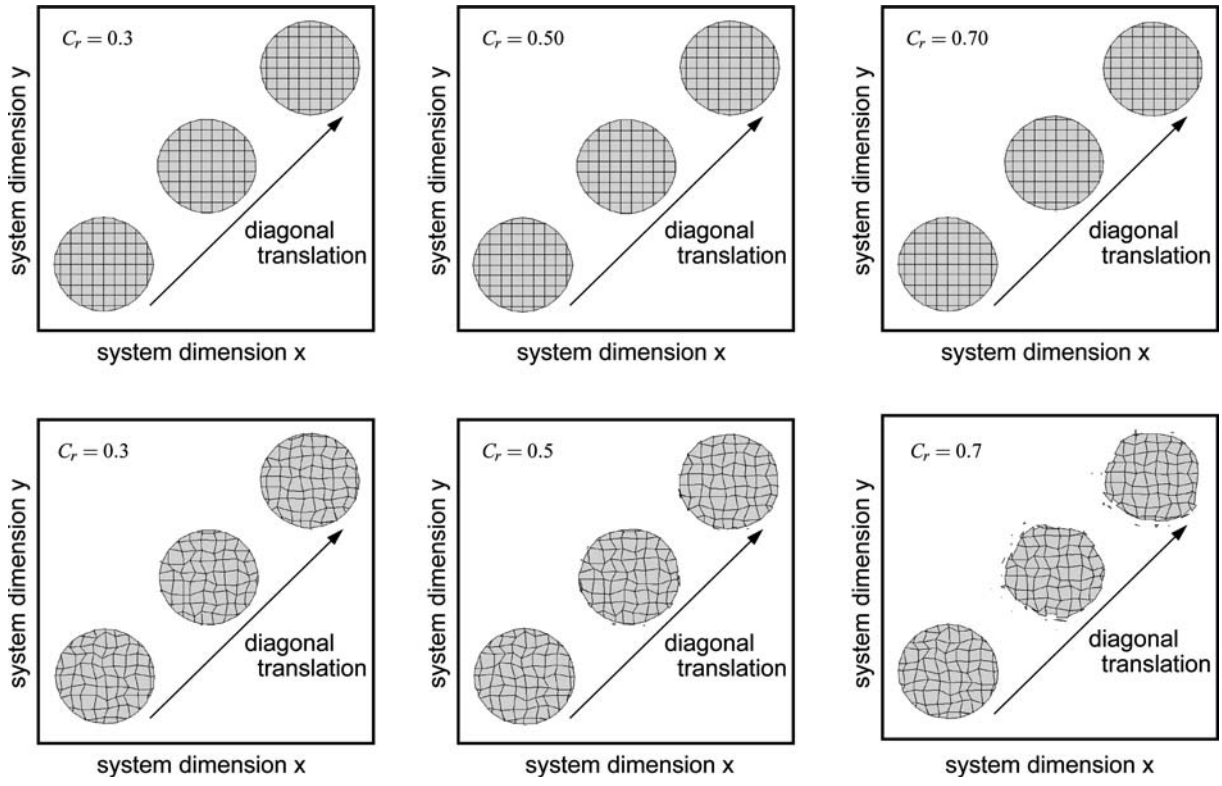

Fig. 35 2D-VOF advection of a single disc in a diagonal velocity field **c** at $C_r = 0.3$, $C_r = 0.5$ and $C_r = 0.7$ on a homogeneous (*top*) and distorted (*bottom*) 30×30 quadrilateral element mesh

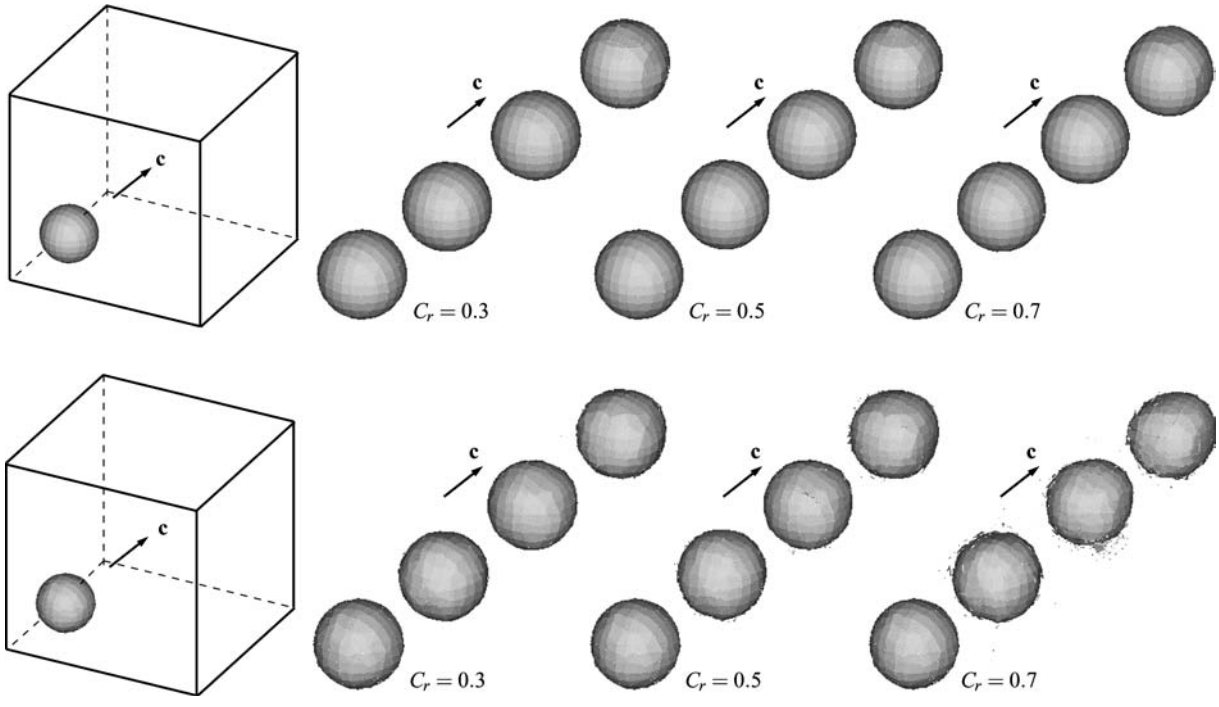

Fig. 36 3D-VOF advection of a single sphere in a diagonal velocity field **c** at $C_r = 0.3$, $C_r = 0.5$ and $C_r = 0.7$ on a homogeneous (*top*) and distorted (*bottom*) $30 \times 30 \times 30$ hexahedral element mesh

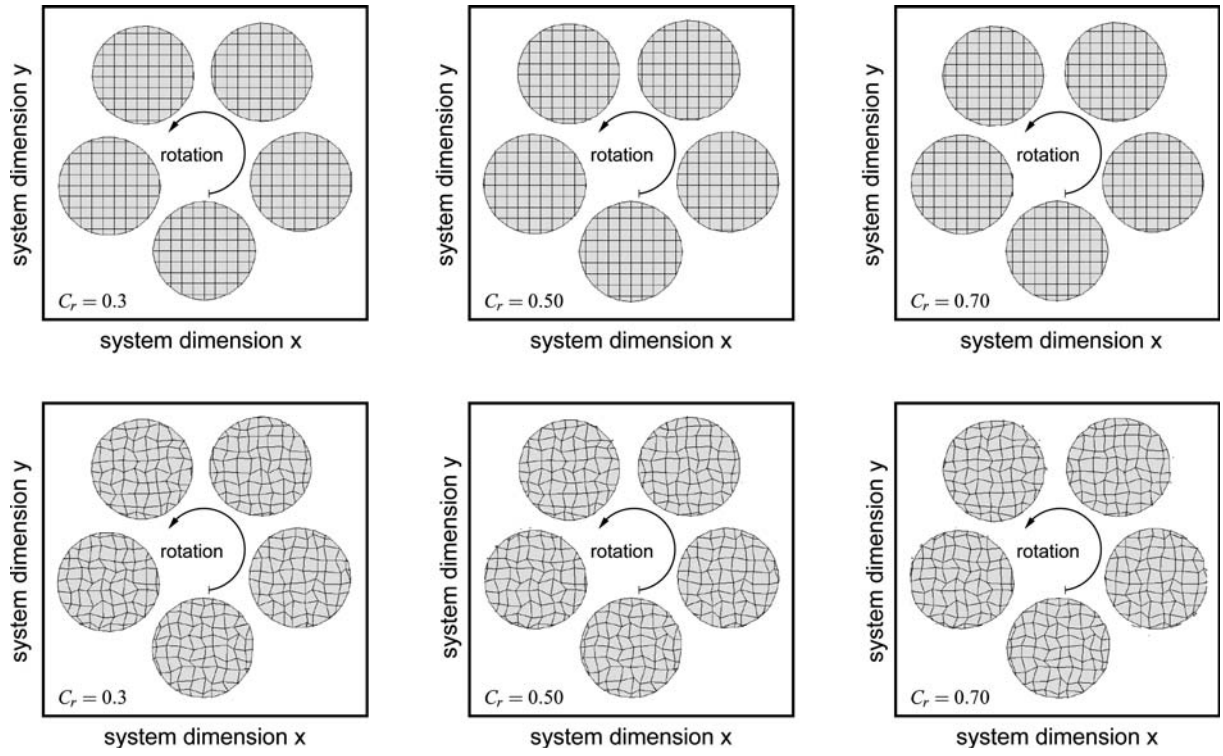

Fig. 37 2D-VOF advection of a single disc in a circular velocity field at $C_r = 0.3$, $C_r = 0.5$ and $C_r = 0.7$ on a homogeneous (*top*) and distorted (*bottom*) 30×30 quadrilateral element mesh

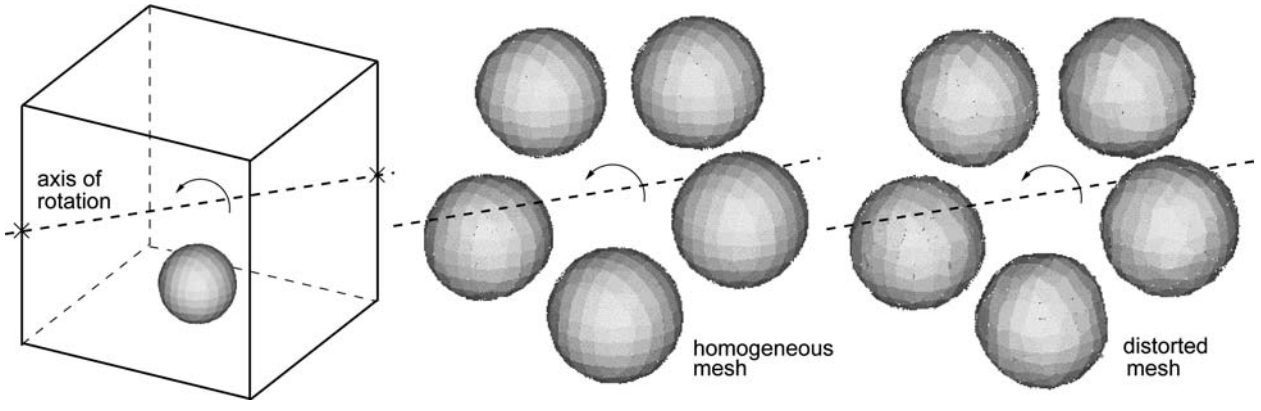

Fig. 38 3D-VOF advection of a single sphere in a circular velocity field at $C_r = 0.5$ on a homogeneous and distorted $30 \times 30 \times 30$ hexahedral element mesh

numbers and the shape of the circular disk is retained sufficiently correct. In the three-dimensional case, depicted in Fig. 38, again similar results are obtained. Here the simulation is limited to a Courant number of $C_r = 0.5$, since the results essentially coincide with the two-dimensional advection process. The single sphere is rotated around a diagonally arranged, horizontal axis where a diagonal advection in all three logical element directions is accounted for.

Since the advection process within the MMALE approach is always performed on a distorted mesh, obtained from the Lagrangian step, the Courant number should be restricted to e.g. $C_r = 0.5$, to ensure a coherent material distribution during the advection step. Correspondingly, to account for the required total advection volumes, the number of necessary advection steps has to be increased.

Example 3 Single disk in a vortex flow Note that the preceding advection tests, the diagonal and the circular advection, are performed in an incompressible flow, where – physically – the disc remains circular and the divergence term in Eq. (32) vanishes. This is the common case in a finite element ALE approach, where the mesh nodes are relocated independently of the spatially fixed material distribution. In the following, a more complex test with a compressible velocity field should be applied to verify the reconstruction capabilities

in a compressible flow. This test was applied by different researchers (see e.g. [59] and references therein) to verify different interface tracking methods. In this test, the advective flow is described by a vortex velocity field within the coordinate limits $(x, y) \in [0, \pi]$ in the two dimensional case [cf. Fig. 34 (right)]

$$v_x = \cos(x)\,\sin(y), \quad v_y = -\sin(x)\,\cos(y), \tag{101}$$

where again an eccentric arranged circular disk is considered. The exact solution is a helix-like distribution of the material without separation (see Fig. 39). For the numerical analysis, the Courant number of the flow is chosen to be $C_r = 0.25$ to minimized the effects arising from the overlapping advection volumes. A first advection test is performed with an initial mesh density of 50 elements per spatial direction, where first, the simulation is integrated forward in time for about 2,000 time steps, before the velocity field is reversed and another 2,000 time steps are performed. The exact solution would certainly return to the initial configuration.

Figure 40 shows the material distribution for the prescribed velocity field at the beginning, after 2,000 time steps and after 4,000 time steps, for the homogeneous and the distorted mesh. A conspicuous effect is the separation of the material distribution in both cases. For an accurate determination of the surface normal $\hat{\mathbf{n}}$, using the finite differences stencil, the distribution of the volume fraction is expected to be as smooth as possible and thus a certain amount of elements is required for all spatial directions. If the mesh density is too small, the gradient of the volume fractions can not be computed properly, dispersion effects occur and finally the material separates. This separation also implicates that the initial configuration is not retained exactly after the velocity is reversed. A comparison between the homogeneous and the distorted mesh shows very similar results, since the dispersion effects of the overlapping volumes are minimized, due to the low Courant number. Moreover, the present mesh density is not able to capture the exact material distribution, as mentioned above.

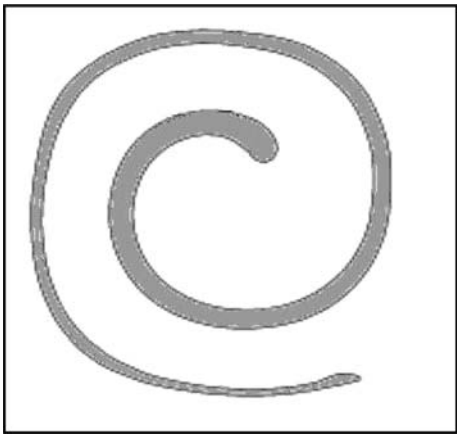

Fig. 39 Sketch of the exact solution of the helix-like vortex flow field after 2½ revolutions (reprinted from [4])

If the mesh density is refined, the material flow is resolved more accurately and less material separation occurs as depicted in Fig. 41. The number of elements per direction is increased to 100, while simultaneously the Courant number is increased to $C_r = 0.5$ to obtain the same deformation velocity. The material after 2,000 time steps is still separated, but the reversed material distribution is reproduced more accurately, compared to the example with the lower mesh density. Transferring these issues to applications in an MMALE finite element context, special care has to be taken into account to ensure that the different materials are always sufficiently resolved by the finite element mesh. Especially, if e.g. highly localized material deformations or crack grows are to be considered, uncertainties due to incorrect material interface reconstructions should be excluded and some kind of error measure has to be included to get an idea of the quality of the material resolution. Indeed, this is not the main objective of this work and is therefore not further considered here.

Considering multiple material properties within one element
A special problem emerges, if more than two material properties occur within one mixed element. This is for instance a standard problem in a micromechanical analysis, where in addition to the matrix material, different inclusion materials may appear. In the advection process, the material interfaces between all material phases have to be reconstructed to account for the correct volume fluxes. Therefore the reconstruction algorithm must first be able to distinguish between different kinds of inclusions and furthermore, all material interfaces have to be reconstructed, based on their respective occurrences. This is realized by storing the volume fractions of all materials that possibly meet within one element or within the first-order adjacent elements, separately as internal element variables. The second point requires a more sophisticated consideration, since special problems can occur concerning the order of the materials and the maintenance of the material coherences. More extensive discussions of this problem are for instance given in [13] or [15].

However, in case of a micromechanical observation, this problem can be circumvented, if the matrix material is treated as a void material that fills the gaps between the inclusions. No explicit volume fraction is associated with the void material and therefore only the volume fractions of the inclusions have to be stored per (mixed-material) element. During the advection step, first the number and type of the materials within each element are determined and subsequently a loop over all element materials is performed, including the corresponding interface reconstructions and the determination of the material-associated advection volumes. Since each material interface is reconstructed independently, the volume fluxes can also be computed independently. Unfortunately, this can lead to problems in the total volume conservation within a mixed element, especially if the inaccuracies mentioned earlier arise. Therefore the corrections, described in Sect. 5.2.3 are necessary to ensure the consistency of the volume fractions [cf. Eq. (77)].

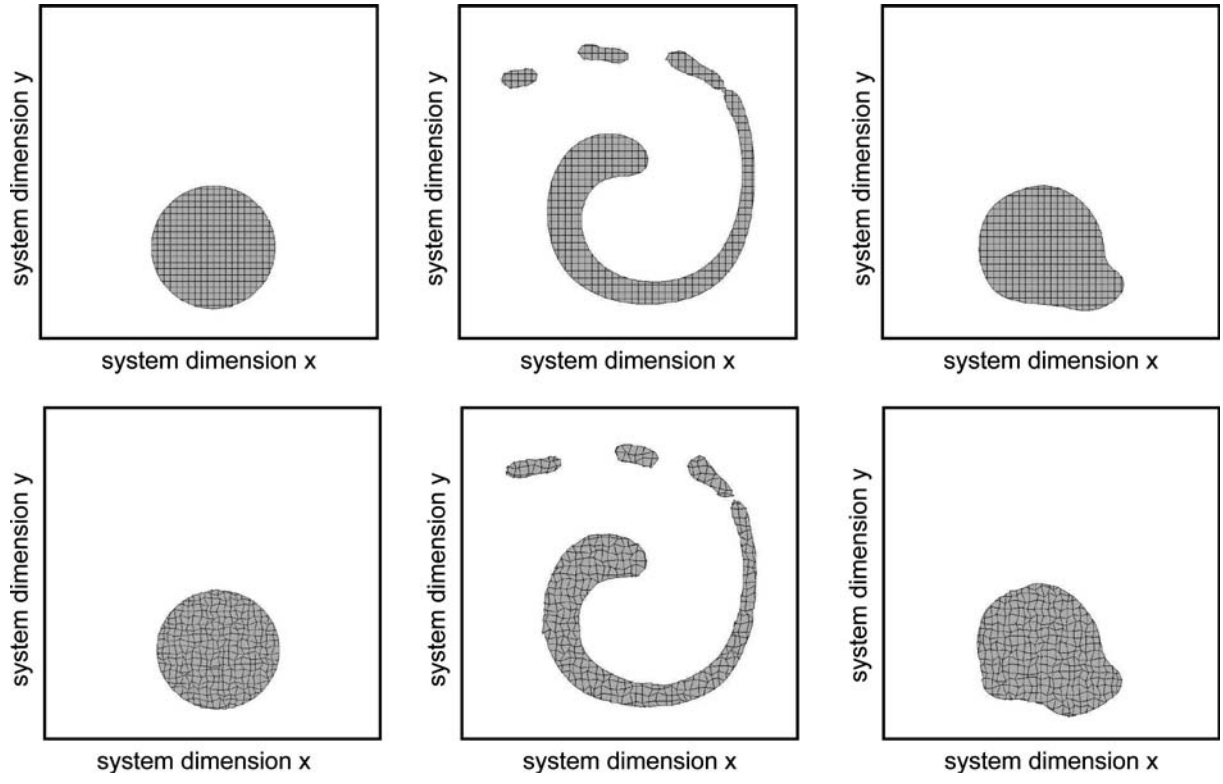

Fig. 40 2D-VOF advection of a single disc in a vortex flow at $C_r = 0.25$; material distribution at the beginning, after 2000 time steps and after reversed advection on a homogeneous (*top*) and distorted (*bottom*) 50×50 element mesh

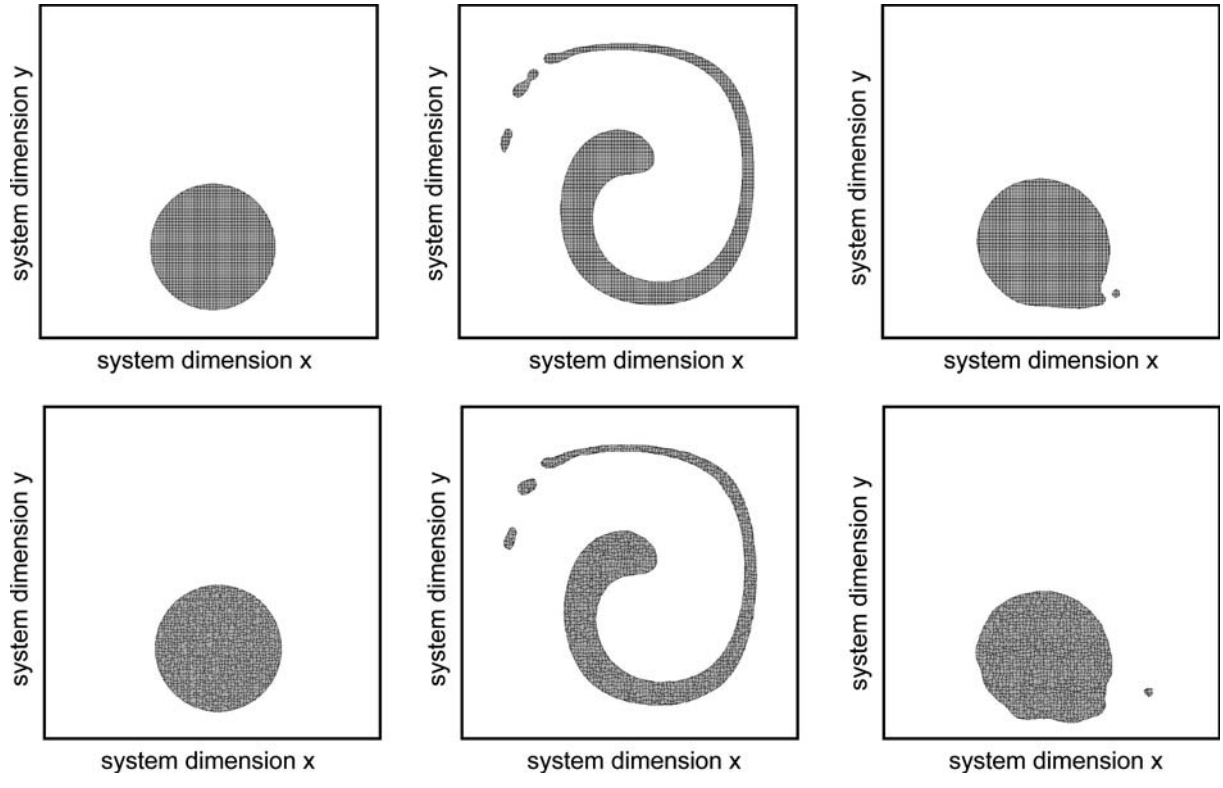

Fig. 41 2D-VOF advection of a single disc in a vortex flow at $C_r = 0.5$; material distribution at the beginning, after 2,000 time steps and after reversed advection on a homogeneous (*top*) and distorted (*bottom*) 100×100 element mesh

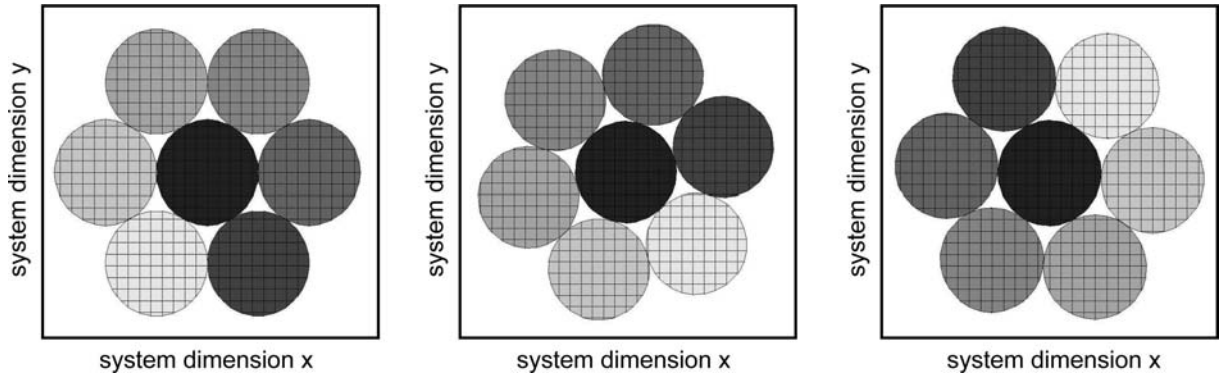

Fig. 42 2D-VOF advection of seven discs in a circular flow; material distribution of the seven discs during the rotation process; homogeneous mesh: 30 elements per spatial direction

Figure 42 shows a simple two-dimensional example, consisting of seven circular discs on a homogeneous mesh. To ensure multiple material properties within the mixed elements, the disks are in initial contact with each other, where, additionally to the matrix material, the elements in the contact zone contain several material phases. The prescribed velocity field corresponds to the incompressible, rotational convective flow from the second example [cf. Fig. 34 (center)]. As can easily be seen, the distinction between the different materials is ensured during the simulation and no mixture of the material phases occurs. Thus the interface tracker is able to distinguish between the different materials, while the boundaries are reconstructed accurately. It should be noted that this algorithm is completely independent of the number of spatial dimensions and therefore also works for the three dimensional case or distorted meshes.

6 Summary and conclusions

In the present paper, different advection approaches for the application in a single- and multi-material ALE finite element framework, based on the fractional step method, have been reviewed and the basic requirements and properties for these methods have been discussed. The arbitrary distribution of the material boundaries in a MMALE approach additionally necessitated a distinction of material- and volume-associated solution variables which led to the implementation of the two different advection approaches. The numerical experiments show that the shape of the variable distribution is reflected accurately and the material distribution remains coherent throughout the advection process while the numerical overhead remains in an acceptable limit.

Indeed, due to the explicit character of the underlying fractional step method, the two computational steps are performed independently of each other. It is well-known that, for instance with regard to the mechanical part of the governing equations, the balance of momentum, i.e. the equilibrium conditions, after the advection step is usually not satisfied. In theory, this might be a problem, especially if extremely large material deformations have to be taken into account. The lack of equilibrium forces the material to deform in the following equilibrium iterations and if the distributions of the solution variables are not properly maintained over the advection process, additional element distortions can occur that may lead to an abortion of the finite element method due to negative Jacobians.

However, the presented advection algorithms are able to reproduce the distribution of the solution variable after the advection step very accurately and the deviation from the solution prior to the advection process is very small and can widely be neglected, especially if the time step size of the Lagrangian step is not chosen to be too large (see [70]).

Acknowledgements This work was financed by the German Research Foundation (DFG) under Grant WR 19/19-1.

References

1. Aboudi J (1991) Mechanics of composite materials – a unified micromechanical approach. Elsevier, Amsterdam
2. Amsden AA, Ruppel HM, Hirt CW (1980) SALE: a simplified ALE computer program for fluid flow at all speeds. Los Alamos National Laboratory, Los Alamos LA-8095
3. Armero F, Love E (2003) An arbitrary Lagrangian-Eulerian finite element method for finite strain plasticity. Int J Numer Meth Eng 57:471–508
4. Aulisa E, Manservisi S, Scardovelli R (2004) A surface marker algorithm coupled to an area-preserving marker distribution method for three-dimensional interface tracking. J Comput Phys 197:555–584
5. Aymone JLF (2004) Mesh motion techniques for the ALE formulation in 3D large deformation problems. Int J Numer Meth Eng 59:1879–1908
6. Bayoumi HN, Gadala MS (2004) A complete finite element treatment for the fully coupled implict ALE formulation. Comput Mech 33:435–452
7. Belytschko T, Ong JS-J, Liu WK, Kennedy JM (1984) Hourglass control in linear and nonlinear problems. Comput Meth Appl Mech Eng 43:251–276
8. Belytschko T, Liu WK, Moran B (2000) Nonlinear finite elements for continua and structures. Wiley, New York
9. Benson DJ (1989) An efficient, accurate, simple ALE method for nonlinear finite element programs. Comput Meth Appl Mech Eng 72:305–350
10. Benson DJ (1992a) Computational methods in Lagrangian and Eulerian hydrocodes. Comput Meth Appl Mech Eng 99:235–394

11. Benson DJ (1992b) Momentum advection on a staggered mesh. J Comput Phys 100:143–162
12. Benson DJ (1997) A mixture theory for contact in multi-material Eulerian formulations. Comput Meth Appl Mech Eng 140:59–86
13. Benson DJ (1998) Eulerian finite element methods for the micromechanics of heterogeneous materials: dynamic prioritization of material interfaces. Comput Meth Appl Mech Eng 151:343–360
14. Benson DJ (2000) An implicit multi-material Eulerian formulation. Int J Numer Meth Eng 48:475–499
15. Benson DJ (2002) Volume of fluid interface reconstruction methods for multi-material problems. Appl Mech Rev 52(2):151–165
16. Boris JP, Book DL (1976) Flux-corrected transport. III - minimal-error FCT algorithms. J Comput Phys 20:397–431
17. Brooks AN, Hughes TJR (1982) Streamline upwind/Petrov-Galerkin Formulations for convection dominated flows with particular emphasis on the incompressible Navier-Stokes equations. Comput Meth Appl Mech Eng 32:199–259
18. Chakravarthy SR, Osher S (1985) A new class of high accuracy TVD schemes for hyperbolic conservation Laws. AIAA 85-0363
19. Chock D (1985) A comparison of numerical methods for solving the advection equation. Atmos Environ 19:571–586
20. Chorin AJ, Hughes TJR, McCracken MF, Marsden JE (1978) Product formulas and numerical algorithms. Commun Pure Appl Math 31:205–256
21. Cockburn B, Shu CW (2001) Runge-Kutta discontinuous Galerkin methods for convection-dominated problems. J Sci Comput 16:173–261
22. Donea J (1983) Arbitrary Lagrangian–Eulerian finite element methods. In: Belytschko T, Hughes TJR (eds) Computational methods for transient analysis, chap. 10. Elsevier, NewYork, USA
23. Donea J, Huerta A (2003) Finite element methods for flow problems. Wiley, New York
24. Dukowicz JK (1988) Efficient volume computation for three-dimensional hexahedral cells. J Comput Phys 74:493–496
25. Gadala MS, Movahhedy MR, Wang J (2002) On the mesh motion for ALE modeling of metal forming processes. Finite Elem in Anal Des 38:435–459
26. Ganzha VG, Vorozhtsov EV (1996) Numerical solutions for partial differential equations. CRC, Boca Raton, New York
27. Ghosh S, Kikuchi N (1991) An arbitrary Lagrangian–Eulerian finite element method for large deformation analysis of elastic-viscoplastic solids. Comput Meth Appl Mech Eng 86:127–188
28. Gross D, Seelig Th. (2001) Bruchmechanik mit einer Einführung in die Mikromechanik. 3. Springer-Verlag, Auflage
29. Gueyffier D, Li J, Nadim A, Scardovelli R, Zaleski S (1999) Volume of fluid interface tracking with smoothed surface stress methods for three-dimensional flows. J Comput Phys 152:423–456
30. Harten A (1983) High resolution schemes for hyperbolic conservation laws. J Comput Phys 49(3):357
31. Hinton E, Campbell JS (1974) Local and global smoothing of discontinuous finite element functions using a least square method. Int J Numer Meth Eng 8:461–480
32. Hirt CW, Nichols BD (1981) Volume of fluid (VOF) method for the dynamics of free boundaries. J Comput Phys 39:201–225
33. Huetink J (1982) Analysis of metal forming processes based on a combined Eulerian–Lagrangian finite element formulation. In: International conference on numerical methods in industrial forming processes, pp 501–509
34. Huetink J, Vreede PT, Van der Lugt J (1990) Progress in mixed Eulerian–Lagrangian finite element simulation of forming processes. Int J Numer Meth Eng 30:1441–1457
35. Hughes TJR (1979) Finite element methods for convection dominated flows. ASME Monograph AMD-34 ASME New York
36. Hughes TJR, Liu WK, Zimmermann TK (1981) Lagrangian–Eulerian finite element formulation for incompressible viscous flows. Comput Meth Appl Mech Eng 29:239–349
37. Hughes TJR, Tezduyar TE (1984) Finite element methods for first-order hyperbolic systems with particular emphasis on the compressible Euler equations. Comput Meth Appl Mech Eng 45:217–284
38. Johnson AA, Tezduyar TE (1999) Advanced mesh generation and update methods for 3D flow simulations. Comput Mech 23:130–143
39. Kothe DB, Williams MW, Lam KL, Korzekwa DR, Tubesing PK, Puckett EG (1999) A second-order accurate, linearity-preserving volume tracking algorithm for free surface flows on 3-D unstructured meshes. In: Proceedings of the 3rd ASME/JSME joint fluids engineering conference, San Francisco, California, USA, fEDSM99-7109
40. Lax P, Wendroff B (1960) System of conservation laws. Commun Pure Appl Math 13:217–237
41. van Leer B (1977) Towards the ultimate conservative difference scheme. IV a new approach to numerical convection. J Comput Phys 23:276–299
42. Liu WK, Belytschko T, Chang H (1986) An arbitrary Lagrangian–Eulerian finite element method for path-dependent materials. Comput Meth Appl Mech Eng 58:227–245
43. Liu WK, Chang H, Chen JS, Belytschko T (1988) Arbitrary Lagrangian–Eulerian Petrov-Galerkin finite elements for nonlinear continua. Comput Meth Appl Mech Eng 68:259–310
44. Löhner R (2001) Applied CFD techniques – an introduction based on finite element methods. Wiley, New York
45. Malvern LE (1969) Introduction to the mechanics of a continuous medium. Prentice Hall, Inc., Englwwood Cliffs
46. Noh WF, Woodward P (1976) SLIC (simple line interface calculation). In: Proceedings of the 5th international conference on numerical methods in fluid dynamics. Twente University, Enschede, June 28 - July 2
47. Ortiz M, Quigley JJ (1991) Adaptive mesh refinement in strain localization problems. Comput Meth Appl Mech Eng 90:781–804
48. Osher S (1985) Convergence of generalized MUSCL schemes. SIAM J Numer Anal 22:947–961
49. Peery JS, Carroll DE (2000) Multi-material ALE methods in unstructured grids. Comput Meth Appl Mech Eng 187:591–619
50. Popinet S, Zaleski S (1999) A front-tracking algorithm for accurate representation of surface tension. Inte J Numer Meth Fluids 30:775
51. Press WH, Teukolsky SA, Vetterling WT, Flannery BP (1992) Numerical recipes in Fortran 77, The Art of Scientific Computing vol 1. Cambridge University Press, London
52. Puckett EG (1991) A numerical study of shock wave refraction at a CO_2/CH_4 Interface. In: Glimm F, Majda A (eds) Multidimensional hyperbolic problems and computations, IMA volumes in mathematics and its applications, vol 29. Springer, Berlin Heidelberg New York pp 261–280
53. Reese S, Wriggers P (2000) A stabilization technique to avoid hourglassing in finite elasticity. Int J Numer Meth Eng 48:79–109
54. Rider WJ, Kothe DB (1998) Reconstructing volume tracking. J Comput Phys 141(2):112–152
55. Roache PJ (1976) Computational fluid dynamics. Hermosa Publishers, Alburquerque, New Mexico
56. Rodriguez-Ferran A, Casadei F, Huerta A (1998) ALE stress update for transient and quasistatic processes. Int J Numer Meth Eng 43:241–262
57. Rodriguez-Ferran A, Perez-Foguet A, Huerta A (2002) Arbitrary Lagrangian–Eulerian (ALE) formulation for hyperelastoplasticity. Int J Numer Meth Eng 53:1831–1851
58. Rood RB (1987) Numerical advection algorithms and their role in atmospheric transport and chemistry models. Rev Geophys 25(1):71–100
59. Rudman M (1997) Volume tracking methods for interfacial flow calculations. Int J Numer Meth Fluids 24:671–691
60. Sweby PK (1984) High resolution schemes using flux limiters for hyperbolic conservation laws. SIAM J Numer Anal 21:995–1011
61. Tezduyar TE, Liou J, Ganjoo DK (1990) Incompressible flow computations based on the vorticity-stream function and velocity-pressure formulation. Comput Struct 35:445–472

62. Tezduyar TE (1992) Stabilized finite element formulations for incompressible flow computations. Adv Appl Mech 28:1–44
63. Tezduyar TE (2001) Finite element methods for flow problems with moving boundaries and interfaces. Arch Comput Meth Eng 8:83–130
64. Tóth G, Odstrěil D (1996) Comparison of some flux corrected transport and total variation diminishing numerical schemes for hydrodynamic and magnetohydrodynamic problems. J Comput Phys 82:82–100
65. Truesdell C, Noll W (1965) The non-linear field theories of mechanics, Handbuch der Physik, chap III/3. Springer, Berlin Heidelberg New York
66. Wang Y, Hutter K (2001) Comparisons of numerical methods with respect to convectively dominated problems. Int J Numer Meth Fluids 37:721–745
67. Youngs DL (1982) Time-dependent multi-material flow with large fluid distortion. In: Morton K, Baines M (eds) Numerical methods for fluid dynamics, Academic, New York, pp 273–285
68. Youngs DL (1987) An interface tracking method for a 3D Eulerian hydrodynamics code. Tech. rep., AWRE Design Math Div, aWRE/44/92/35
69. Zienkiewicz OC, Xi-Kui L, Nakazawa S (1985) Iterative solution of mixed problems and stress recovery procedures. Comput Appl Numer Meth 1:3–9
70. Fressmann D (2005) On single- and multi-material arbitrary Lagrangian–Eulerian approaches with application to micromechanical problems at finite deformations. PhD thesis, Institute of Mechanics and Computational Mechanics, University of Hannover, Germany